PUNCHING BEHAVIOUR OF A HYBRID REINFORCED CONCRETE BRIDGE DECK

by

HANEY JOHN LOUKA

A Thesis
Presented to the Faculty of Graduate Studies
in Partial Fulfilment of the Requirements
for the Degree of

MASTER OF SCIENCE

Department of Civil & Geological Engineering
University of Manitoba
Winnipeg, Manitoba

THE UNIVERSITY OF MANITOBA

FACULTY OF GRADUATE STUDIES

*****

COPYRIGHT PERMISSION PAGE

PUNCHING BEHAVIOUR OF A HYBRID REINFORCED CONCRETE BRIDGE DECK

BY

HANEY JOHN LOUKA

A Thesis/Practicum submitted to the Faculty of Graduate Studies of The University of Manitoba in partial fulfillment of the requirements of the degree of MASTER OF SCIENCE

ABSTRACT

Deterioration of concrete structures subjected to aggressive environmental conditions is attributed to corrosion of the steel reinforcement. Highway bridge deck slabs in particular are exposed to de-icing chemicals that attack the internal reinforcement after the initiation of cracks on the top surface. The use of glass-fibre reinforced polymer (GFRP) bars as top reinforcement in the deck slab greatly increases the resistance of the deck slab to corrosion. Conventional steel bottom reinforcement allows the structural deck system to achieve an overall ductility close to that of a conventional steel-reinforced bridge deck. This hybrid reinforcing system presents a compromise between corrosion-free FRP reinforcement, with low ductility and high cost, and ductile, inexpensive conventional reinforcement, with poor corrosion resistance.

This thesis presents the experimental program of a full-scale hybrid-reinforced bridge deck model. Five static tests were conducted using a simulated design wheel loading to investigate the suitability of a hybrid reinforcing system for highway bridge deck slabs. The behaviour of the experimental model is evaluated and compared with other experimental and analytical models as well as code predictions. Based on this investigation, recommendations are made regarding the applicability of hybrid reinforcement for concrete highway bridge decks.

ACKNOWLEDGEMENTS

I would like to thank Dr. Sami Rizkalla and Dr. Amr Abdelrahman for their guidance, advice, and support throughout the experimental phase and the writing of this thesis.

The staff and students at the McQuade Structural Laboratory, who were always willing to assist in the construction and testing of the experimental model, are also sincerely thanked.

Research funding and financial assistance by the Canadian Network of Centres of Excellence on Intelligent Sensing for Innovative Structures (ISIS Canada) is acknowledged and greatly appreciated.

I would like to express my sincere gratitude to my wife, Kirsten Louka, my parents, Amazis and Sophy Louka, and to the rest of my family for their unending support and encouragement during the undertaking of this thesis.

I dedicate this thesis to my wife, Kirsten.

TABLE OF CONTENTS

LIST OF FIGURES

CHAPTER 1: INTRODUCTION

1.1 GENERAL OVERVIEW

Deterioration of concrete structures subjected to aggressive environmental conditions is normally attributed to corrosion of the steel reinforcement. After the initiation of cracks, de-icing compounds used on roads and bridges can migrate from the top surface of the concrete, through the concrete cover, to the reinforcing bars. Once this occurs, corrosion of the steel begins. Corroded steel has a higher volume than that of its original state, causing expansion of the reinforcement. This expansion induces further cracking and eventually spalling of the concrete cover. Fibre reinforced polymers (FRP) provide a suitable and desirable alternative to conventional steel reinforcement. The main advantages of FRP include corrosion resistance and high tensile strength. A full-scale model of a highway bridge deck slab was constructed and tested at the University of Manitoba to investigate the effect of using a hybrid reinforcing system: glass-fibre reinforced polymer (GFRP) as top reinforcement, and conventional steel as bottom reinforcement. In addition to the favourable properties that are characteristic of FRP, GFRP was selected because it is more economical than other FRP products made from carbon or aramid fibres. In flexural members, GFRP is largely unsuitable because it has a low elastic modulus that results in the formation of very large cracks, leading to high deflections. For bridge deck slabs, however, the development of internal membrane forces, or "arch action," limits the flexural behaviour of the deck slab, resulting in a reduction of

crack width and consequently deflection. Traditional steel reinforcement was selected for the bottom layer of reinforcement since corrosion of the deck slab normally begins with the initiation of cracks and subsequent chloride ingress from the top surface. This phenomenon therefore does not affect the bottom reinforcement to the same extent. Use of traditional steel reinforcement at the bottom layer enhances the overall ductility of the slab. Five tests were conducted on the full-scale bridge deck model, three on the interior spans and two on the cantilevers. Each test was conducted until failure occurred, using repeated loading.

1.2 OBJECTIVES AND SCOPE

The principal objective of the experimental program is to determine the suitability of hybrid reinforcement for highway bridge deck slabs. In particular, the deck slab model was constructed and tested with the following objectives taken into consideration:

- To study the behaviour of the full-scale interior spans and cantilevers under repeated loading, specifically with respect to:
  - Load capacity
  - Crack patterns
  - Failure mode
  - Serviceability
  - Strain distribution
  - Force distribution
  - Girder rotations

- To compare the behaviour of the experimental model with:
  - Cantilevers and interior spans tested by other researchers
  - Analytical model
  - Code predictions
- To determine the overall suitability of hybrid reinforcement for highway bridge deck slabs, by investigating whether the low elastic modulus of GFRP adversely affects the serviceability of the highway bridge deck slab.

Chapter 2 discusses the general behaviour of bridge deck slabs available in the literature. Also discussed in Chapter 2 are predictions of the punching capacity of slabs from design codes used in North America, as well as other models for predicting punching behaviour. Chapter 3 gives a complete description of the experimental program. The results and analysis of the experimental program are presented in Chapter 4, followed by a comparison between the behaviour of this model with that of an analytical model developed by others in Chapter 5. In Chapter 6, the behaviour of the experimental model is compared with that of the CFRP-reinforced model previously tested at the University of Manitoba. Once detailed analyses and comparisons are made for the hybrid-reinforced experimental model, conclusions are drawn and recommendations made on the suitability of hybrid reinforcement for highway bridge deck slabs.

CHAPTER 2: LITERATURE REVIEW

2.1 BEHAVIOUR OF BRIDGE DECK SLABS

2.1.1 General

It has been well documented that two-way concrete slabs with end restraints can achieve punching failure loads far in excess of loads predicted using flexural theory (e.g., Taylor and Hayes, 1965; Hewitt and Batchelor, 1975; Kuang and Morley, 1992; Azad *et al.*, 1994; Mufti *et al.*, 1996; Abdelrahman *et al.*, 1996). According to flexural theory, an applied load on the slab will induce internal compressive forces in the concrete being of magnitude equal to that of the tensile forces in the reinforcement. The tensile forces in the section will necessitate outward displacement of the supporting girders to maintain equilibrium. Under limit states design, the member will fail when either the compression in the concrete or tension in the reinforcement reaches a limiting strain value.

A highway bridge deck slab, however, exhibits more complex behaviour. The main supporting girders are restrained from rotation by cross-diaphragm beams which are structurally integrated with the slab system. The cross-diaphragm beams resist the outward displacement of the main girders by sustaining tensile stresses and, in turn, induce compression on the section. Therefore, instead of satisfying equilibrium at a particular location, the slab is subjected to compression, while the cross-girders

provide the tensile resistance. These in-plane forces induced on the section are known as compressive membrane forces, and the mechanism as a whole is referred to as "arch action." The arch-action mechanism is shown schematically in Figure 2-1. By the development of compressive membrane forces, the section is capable of supporting loads that are far higher than flexural theory predicts. In addition, deflections due to an applied load are lower because of smaller crack widths due to lower induced tensile stresses in the section than those developed in typical flexural members. Kirkpatrick, *et al.* (1986) concluded that the development of compressive membrane action played an important part in the control of cracking, resulting in improved serviceability characteristics.

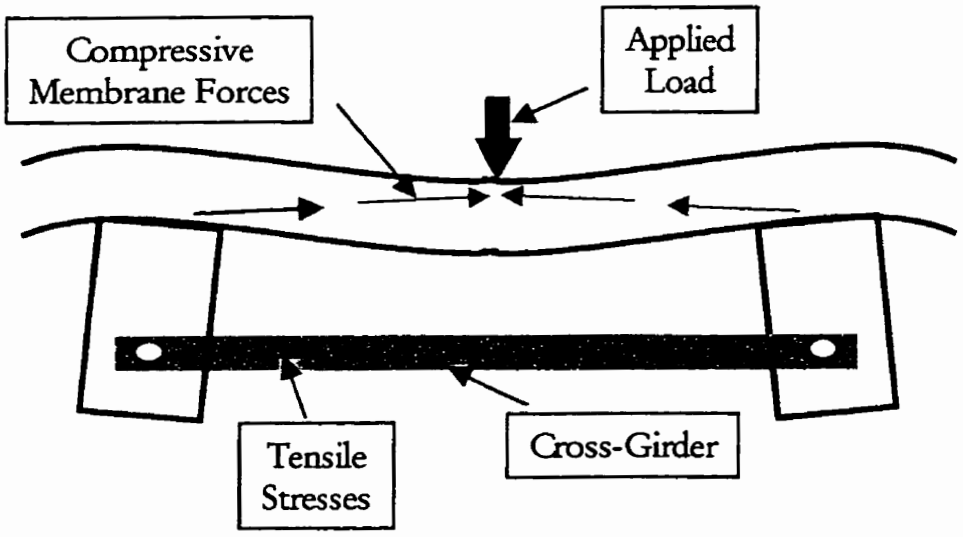

Figure 2-1: Schematic Representation of Arch Action

2.1.2 Cracking Behaviour

As described by Newhook (1997), the typical behaviour of a deck slab begins with the appearance of radial cracks on the bottom surface, usually at relatively low loads. These radial cracks extend from the point of load application to the outer edges of the slab. As the load increases, circumferential cracks are developed on the top surface, with a diameter roughly equal to the spacing of the supporting girders. After the formation of these cracks, the initial radial cracks extend upward to the top surface of the slab, forming full-depth cracks. The final cracking behaviour consists of an inclined shear crack that starts at the bottom surface and extends towards the load to the top surface. This inclined shear crack defines the shear punch cone, which punches out at failure. As Newhook noted, deck slabs with different reinforcing systems all exhibit the same type of punching shear behaviour.

2.1.3 Effect of End Restraints

The presence of end restraints affects the level of membrane forces that are developed in a deck slab, in turn significantly influencing its punching capacity (Taylor and Hayes, 1965; Tadros *et al.*, 1998). Taylor and Hayes concluded that restraint of the edges of the slabs from outward movement increased their punching shear strength. Park (1965) stated that the lateral stiffness and strength of surrounding panels and beams should be examined closely, since membrane action depends on the restriction of very small horizontal translations, and large horizontal

forces are involved. Abdelrahman *et al.* (1998) observed that increasing the stiffness of the end restraints of the supporting beams for a bridge deck reinforced with CFRP increased the ultimate carrying capacity by 20%. When stiffer end restraints were used in conjunction with edge stiffeners to model the continuity of the slab, an additional increase in capacity of 12% was observed. Kuang and Morley (1992) concluded that stiffer lateral restraint resulted in a higher punching shear strength. Newhook (1997) noted that the degree of lateral restraint determines the ultimate punching load at which the deck slab fails. Tadros *et al.* (1998) reported that the top flanges of the supporting girders had to be connected in order to provide sufficient restraint for the deck slab. Connection of these girders resulted in a failure load 2.5 times that of an unrestrained slab.

2.1.4 The Steel-Free Deck Concept

Mufti *et al.* (1993) have been strong advocates of the enhanced capacity of bridge deck slabs due to in-plane restraint. This research group is the pioneer of the steel-free deck slab concept. Mufti *et al.* recognised the enhanced capacity of deck slabs that is possible due to the presence of a system of internal arches that support the applied load. By acknowledging this mechanism, they demonstrated that the removal of all internal steel reinforcement of the deck slab was feasible. This practice virtually eliminates susceptibility of the concrete bridge deck to corrosion.

As shown in Figure 2-2, the concrete deck slab in the steel-free system is supported by steel girders. The shear forces from the applied load are transferred to the girders through shear connecting studs. To provide the restraint necessary for development of arch action, steel straps are welded to the top flanges of the supporting girders. Low-modulus short polypropylene fibres are required within the slab to act as a plastic crack control device and to provide some ductility to the slab. It should be noted that these fibres do not add any structural capacity to the slab system.

Newhook (1997) reported that the durability of the steel-free deck slab is greatly increased due to the absence of steel. He also states that the operation and maintenance costs are substantially reduced, and an increased service life is probable. In addition, with further refinement, the steel-free decks will likely be less expensive than reinforced concrete decks based on capital cost considerations.

This new structural concept has been applied in the design and construction of the Salmon River Bridge near Kemptown, NS, the world's first highway bridge using the steel-free concrete bridge deck technology (Newhook, 1997). It has also been applied in the design and construction of the Crowchild Trail Bridge in Calgary, AB, in 1997. A model of the cantilever of the Crowchild Trail Bridge forms a portion of the experimental program conducted for this thesis.

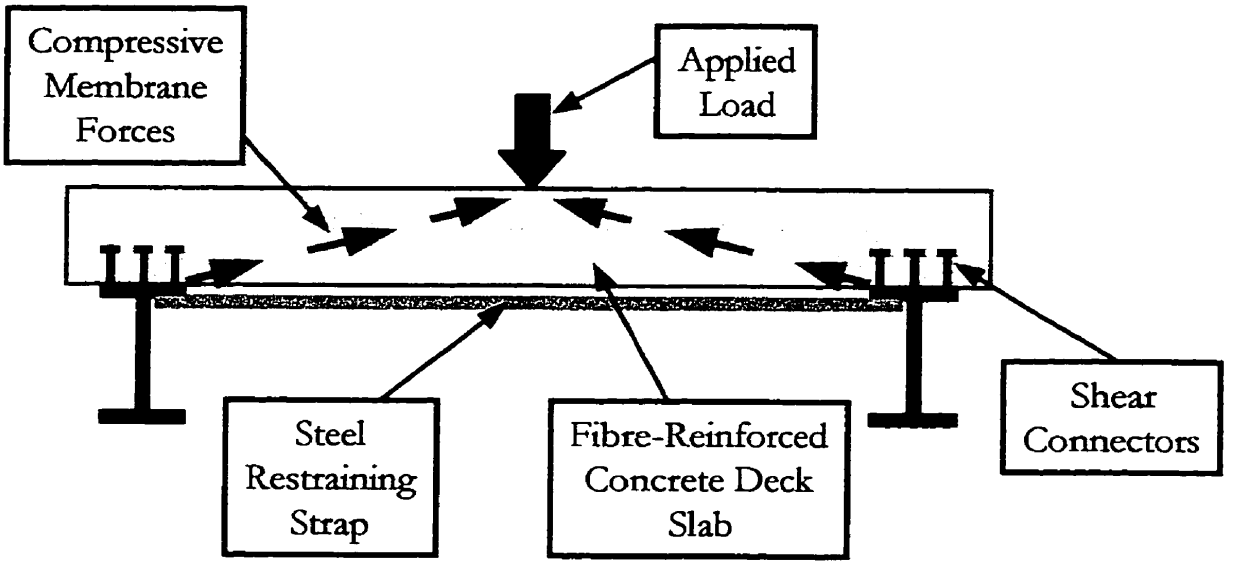

Figure 2-2: The Steel-Free Deck Slab Concept

2.2 EXISTING CODES FOR BRIDGE DECK SLABS

In this section, shear strength predictions from the design codes of different countries are presented.

The following symbols are used in this section:

V_c = punching shear capacity of concrete;
f_r = concrete tensile strength;
f_{pc} = compressive stress in concrete due to prestressing;
b_o = perimeter of critical section at a distance of d/2 from applied load;
d = section depth;
V_p = component of effective prestressing force in direction of applied shear;
β_c = ratio of long side to short side of load plate; and
α_s = constant; function of support conditions.

For the experimental model in this thesis,

f_r = 4 MPa;
f_{pc} = 0;
b_o = 2*(425+775) = 2400 mm;
d = 200 mm;
V_p = 0;
β_c = 575/225 = 2.56; and
α_s = 30 (load < 10d from edge of slab).

2.2.1 Ontario Highway Bridge Design Code (OHBDC) 1991

The OHBDC design equation for the punching shear strength of concrete slabs is given as follows, in units of N and mm:

$$V_c = (0.6f_r + 0.25f_{pc})b_o d + 0.9V_p$$

2.2.2 Canadian Standards Association (CSA CAN–A23.3–94)

The maximum two-way shear resistance of concrete in punching according to CSA is given by the smallest of:

$$V_c = \left(1 + \frac{2}{\beta_c}\right)0.2\sqrt{f_c'}b_o d$$

$$V_c = 0.4\sqrt{f_c'}b_o d$$

$$V_c = \left(\frac{\alpha_s d}{b_o} + 0.2\right)\sqrt{f_c'}b_o d$$

in units of N and mm.

2.2.3 AASHTO LRFD 1998

The American Association of State Highway and Transportation Officials (AASHTO) LRFD Code for the Design of Highway Bridges uses the smallest of the following values for the punching resistance of concrete slabs, in units of N and mm:

$$V_c = \left(0.17 + \frac{0.33}{\beta_c}\right)\sqrt{f_c'}\,b_o d$$

$$V_c = 0.33\sqrt{f_c'}\,b_o d$$

2.2.4 American Concrete Institute (ACI 318M–89)

The ACI 1990 Building Code specifies the minimum of the following values for the punching resistance of concrete slabs, in units of pounds and inches:

$$V_c = \left(2 + \frac{4}{\beta_c}\right)\sqrt{f_c'}\,b_o d$$

$$V_c = 4\sqrt{f_c'}\,b_o d$$

$$V_c = \left(\frac{\alpha_s d}{b_o} + 2\right)\sqrt{f_c'}\,b_o d$$

The predicted values for the punching capacity of the experimental model presented in this thesis according to the methods shown above are given in Figure 2-3.

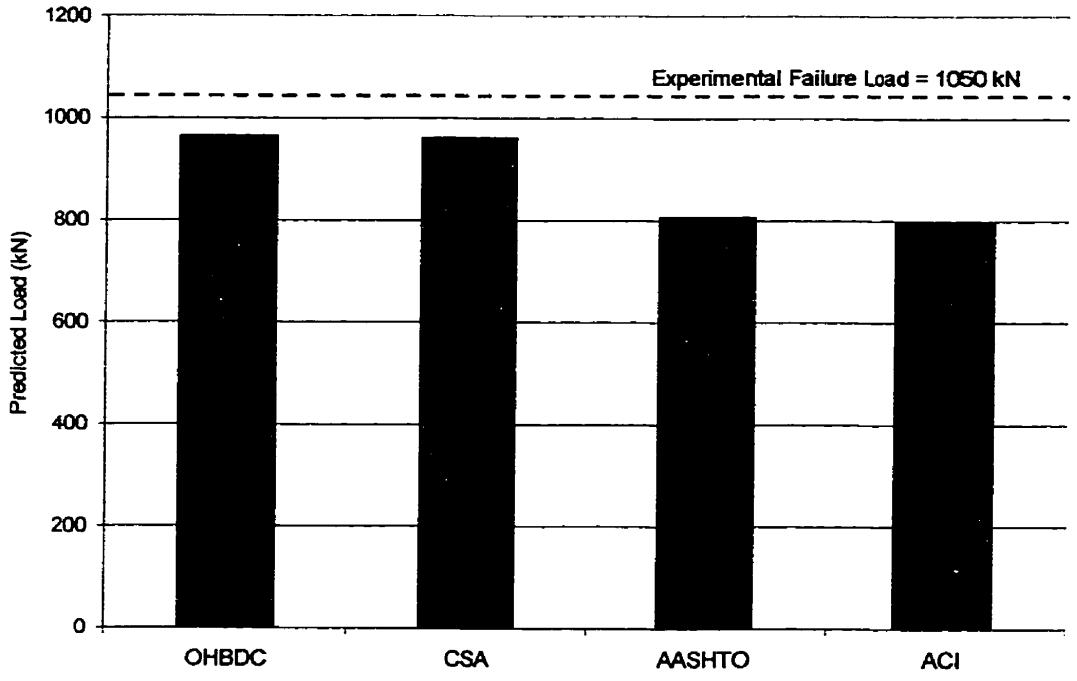

Figure 2-3: Predicted Punching Strength According to Design Codes

2.3 OTHER METHODS OF EVALUATING BRIDGE DECK SLAB BEHAVIOUR

2.3.1 ANATECH Concrete Analysis Program

ANACAP, short for ANATECH Concrete Analysis Program by ANATECH Corporation of San Diego, California, is a non-linear finite element modelling program specifically for modelling of concrete and steel structures. It takes into consideration the highly non-linear response associated with concrete, specifically due to cracking, creep, aging, crushing, reinforcement yielding, and bond failure.

Based on information from the developer, provision is made for the following aspects of concrete behaviour:

- cracking;
- crushing;
- temperature dependence and degradation;
- aging, creep, and shrinkage;
- rebar–concrete interaction; and
- existing cracks and weak zones.

Information from the developer indicates that ANACAP has many capabilities to assist engineers in advanced analysis in various areas of engineering. The discussion here will be limited to material models, element types, and analysis capabilities.

ANACAP can model concrete cracking, including closing and reopening of cracks and aggregate shear interlock. The program includes a compressive plasticity model

for simulation of concrete crushing and spalling and post critical damage modelling. Reinforced or prestressed concrete can be modelled, with explicit reinforcement modelling, including bond slip and anchorage failure capabilities. For dynamic analyses, Raleigh mass and stiffness proportional damping with localised damping in damaged areas are used. For general isotropic materials, elasticity, plasticity, and strain hardening capabilities are included in ANACAP.

ANACAP is capable of modelling of straight or curved beams with rectangular, I or T shaped, box, or tubular cross-sections in two and three dimensions. The two-dimensional models can include plane stress, plane strain, or axisymmetric formulations for four- or eight-node quadrilateral and three- or six-node triangular elements. For three-dimensional models, solid elements with eight- or 20-node hexahedral bricks or 15-node prisms, and plate or shell elements in eight-node quadrilaterals can be used. Reinforcing bars can be incorporated into any of the elements with concrete material.

ANACAP can be used to model two- and three-dimensional structures constructed with plain, reinforced, or prestressed concrete and steel. The response to loading capabilities of the program include static and dynamic structural response, thermal response, coupled thermal and structural response, and seismic or impact analysis. In terms of data output, ANACAP is capable of producing stress-strain distribution predictions, concrete cracking and crushing, rebar demands, structural damage and energy absorption, ultimate capacity, and post-event margin to failure. The program

can also be used to simulate incremental construction, giving predictions of the cracking and residual stresses that occur during the construction phase. Evaluation of structures with existing cracks or construction joints can be performed. Structural phenomena such as local and global buckling, plastic hinges, and collapse of concrete and steel structures with cyclic hysteresis behaviour can be investigated.

The purpose of developing an analytical model using a finite element modelling program such as ANACAP is to facilitate parametric studies. With an analytical model, any characteristic of an existing structure can be varied in order to investigate the resulting effects on behaviour. Conducting such parametric studies through construction and testing of experimental models is extremely expensive and time-consuming.

2.3.2 Rational Model for Steel-Free Concrete Bridge Deck Slabs

Newhook (1997) found that models to predict the punching behaviour of deck slabs that are currently used in codes are not valid for the steel-free deck concept due to one or both of the following reasons:

1. They contain terms that account for the presence of internal reinforcement;
2. They do not account for restraint stiffness.

Newhook therefore considered it necessary to develop a new model that was suitable for the behaviour exhibited by the steel-free deck. The one he developed was based

on an existing model formulated in 1960 by Kinnunen and Nylander. Newhook made many significant contributions to this rational model:

- The concrete surrounding the applied load is in a state of three-dimensional compression, and this is accounted for by the employment of an empirical constant to describe the confinement conditions in a deck slab.
- A method is developed to determine the lateral restraint value to be used in the rational model, one that is able to account for the restraint stiffness provided by both the straps and the girders as well as the variation in restraint stiffness due to the proximity of the individual straps to the applied load.
- A failure criterion associated with the yielding of the steel straps is developed, in addition to the one associated with the attainment of a critical strain value that was previously used.
- While the model was developed initially for steel-free deck slabs, the rational model is applicable to reinforced concrete bridge decks.

The three failure mechanisms recognised in this model include instability, crushing of the concrete, or yielding of the restraint straps. While the first mode is related to "snap-through" failure of the deck, the last two failure mechanisms lead to punching failure.

With this rational model, the punching behaviour of a deck slab can be predicted favourably regardless of the presence of internal reinforcing (Newhook 1997).

CHAPTER 3: EXPERIMENTAL PROGRAM

3.1 GENERAL DESCRIPTION

A full-scale model of a three-metre segment of a highway bridge deck slab was constructed and tested to examine the behaviour of bridge deck reinforced with hybrid GFRP and steel reinforcement. The model is 7.2 metres wide and consists of three continuous spans with two cantilevers, one on each end, as shown in Figure 3-1. The supporting girders are spaced at 1800 mm on centre, and the span of each cantilever is 900 mm to the centreline of the girder. Each of the precast, pretensioned girders has a cross section of 350 x 750 mm and is supported by 750 x 750 x 1000 mm support blocks, anchored to the structural floor. Deformed 15M steel bars are used as bottom reinforcement at a 150-mm spacing, as shown in Figure 3-2, with the exception of the right cantilever, where no bottom reinforcement was used. This was done to simulate the conditions for the Crowchild Trail Bridge in Calgary, built in 1997. Two types of FRP bars are used for top reinforcement in the slab. The right cantilever, the adjacent span, and the middle span are reinforced with double 15 mm C-BAR bars at 250 mm on centre. C-BAR is produced by Marshall Industries in Lima, Ohio, U.S.A. The top reinforcement for the left cantilever and adjacent slab are reinforced by double 15 mm ISOROD bars at 250 mm on centre. ISOROD is produced by Pultrall, Inc. in Quebec, Canada. The overall reinforcement

of the slab before casting is shown in Figure 3-3, and a photograph of the experimental model after testing is shown in Figure 3-4.

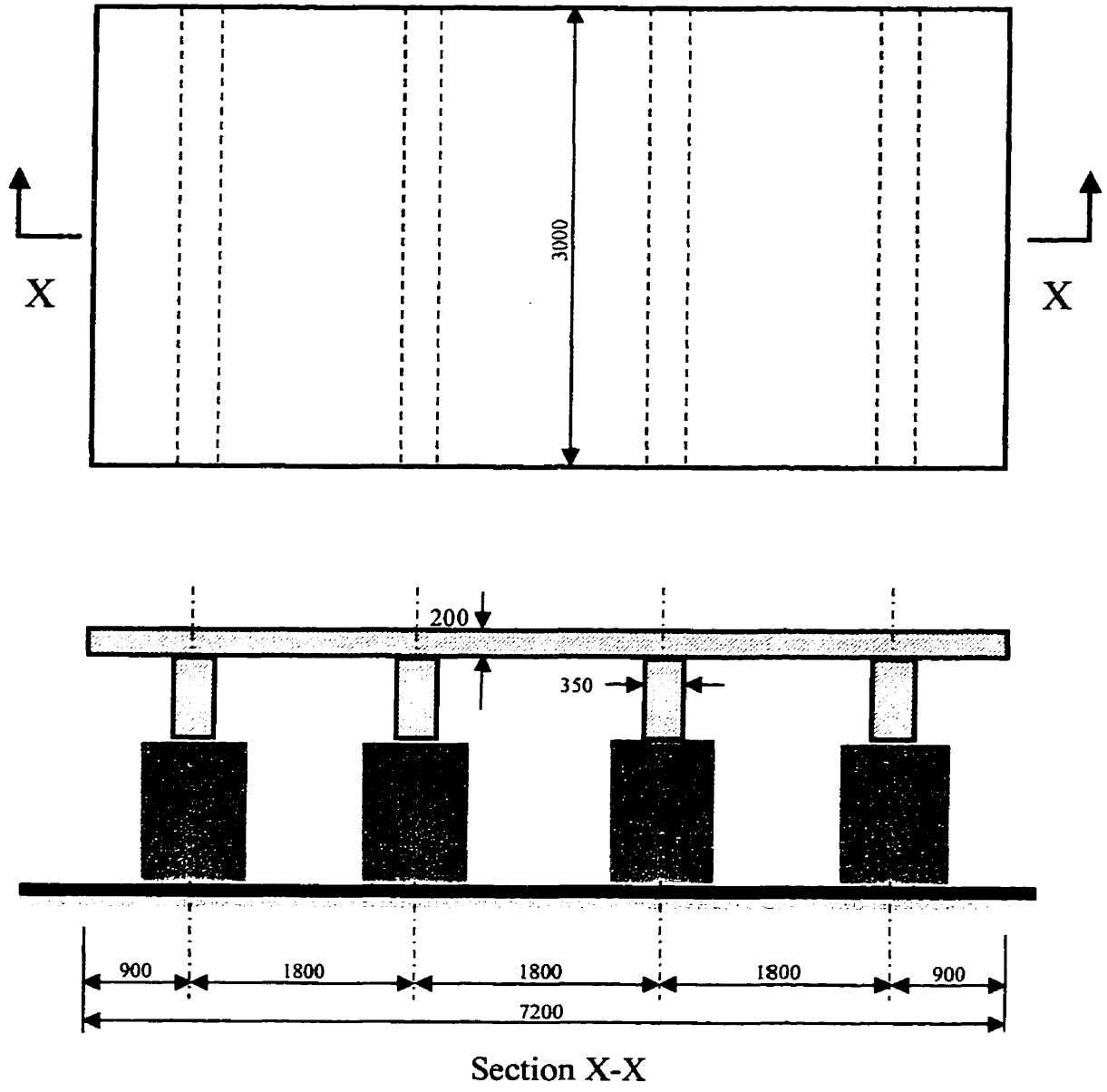

Figure 3-1: Experimental Model Dimensions

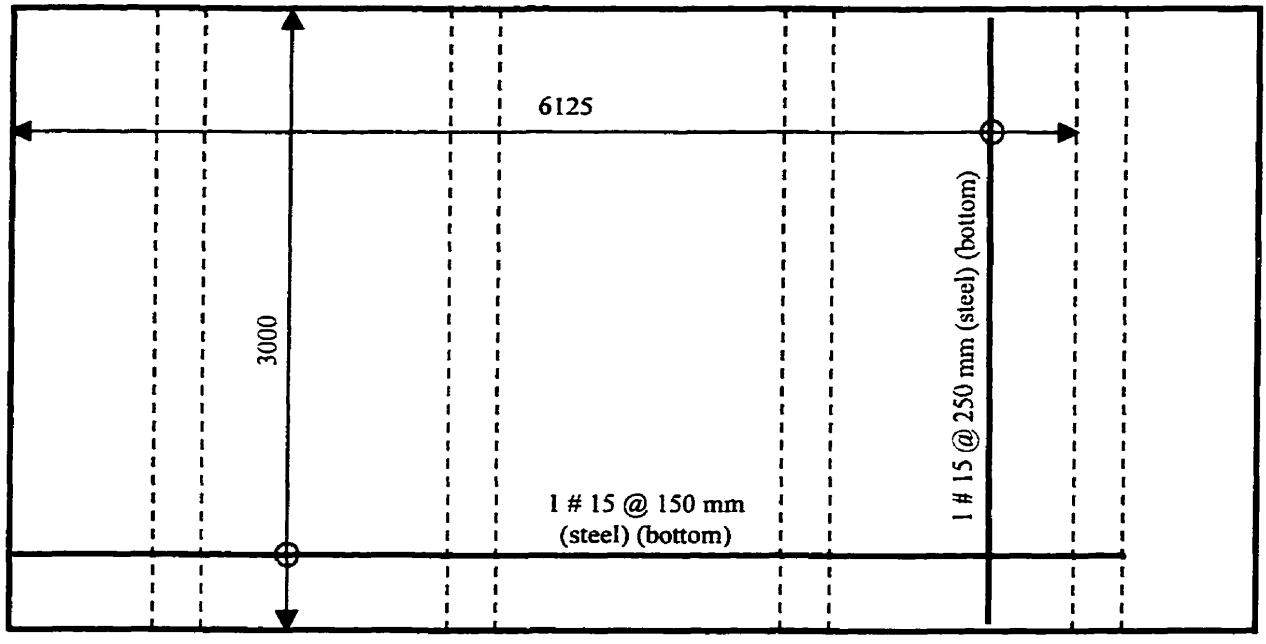

Bottom reinforcement

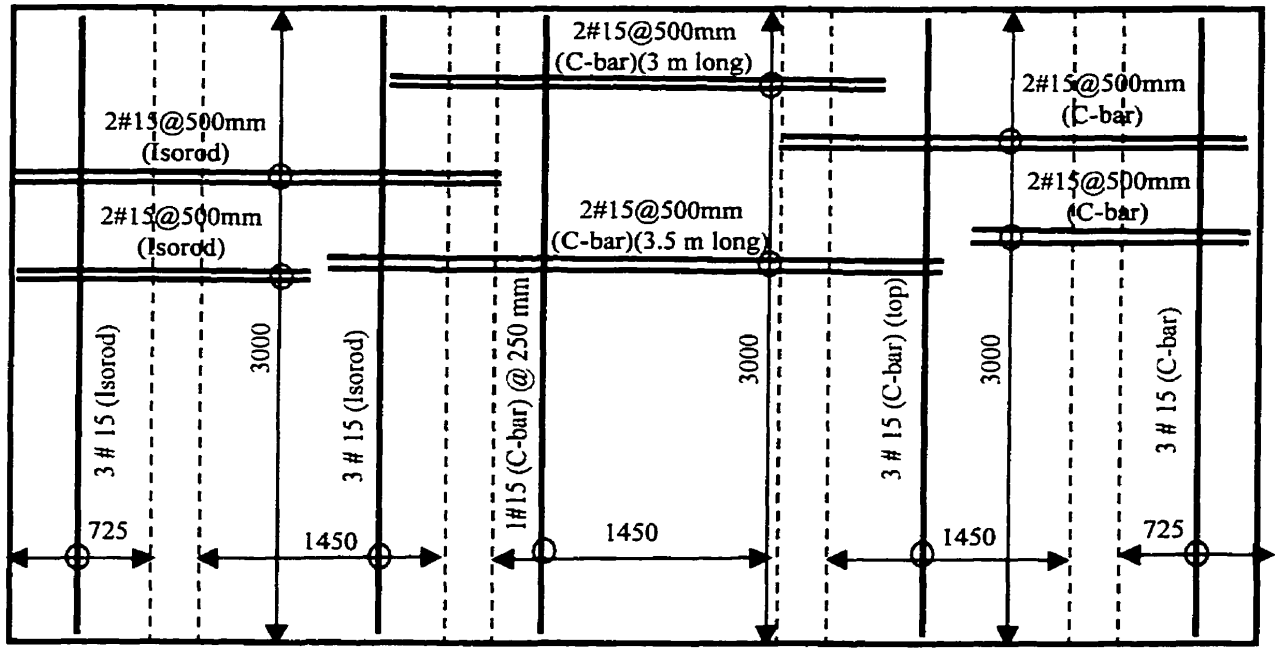

Top reinforcement

Figure 3-2: Slab Reinforcement Details

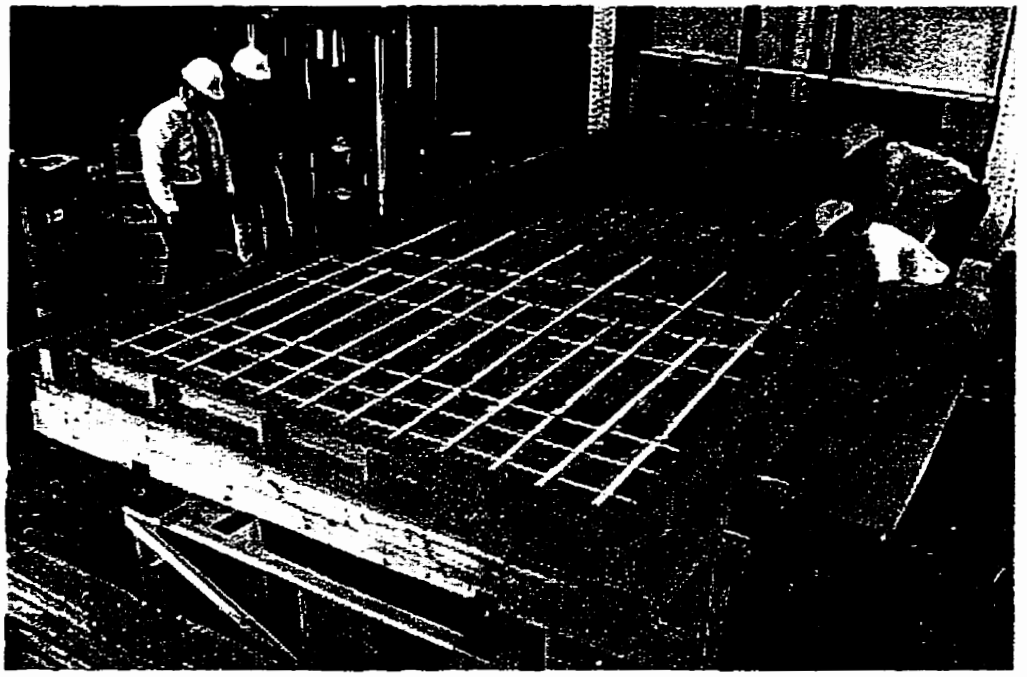

Figure 3-3: Photograph of Slab Reinforcement

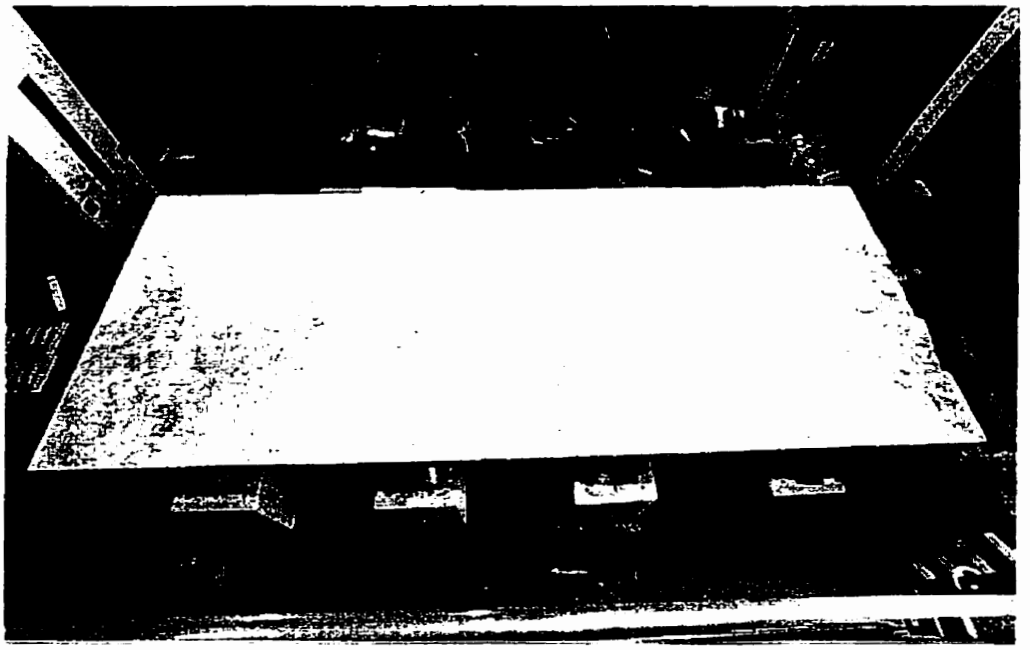

Figure 3-4: Photograph of Experimental Model after Testing

3.2 TESTING PROGRAM

Five tests were conducted on the experimental model, one on each of the three interior spans, and one on each of the two cantilevers. Figure 3-5 shows the location of the applied load for each of the five tests.

For each of the tests, load was applied using an 1800 kN hydraulic jack that was operated by an air-powered pump with manual stroke control. The load was measured using a load cell of 1800 kN capacity. Load was applied in three cycles from zero to specified load levels to allow for stabilisation of cracks. The size of the loading plate was determined according to the AASHTO Bridge Design Code. The AASHTO HS-25 design vehicle has a tire contact patch of 225 x 575 mm. A neoprene pad was placed between the load plate and the slab to simulate the tires of the design vehicle, while at the same time preventing local crushing of the concrete due to stress concentrations. According to the AASHTO–LRFD 1998 Code, the specified load for each contact patch is 72.5 kN. This load is multiplied by a live load factor of 1.5, and an impact allowance of 1.33, for a factored load of 145 kN. The experimental model was cast in May, 1997.

The first test was conducted on the right cantilever of the model, which was designed to model the Crowchild Trail Bridge in Calgary, Alberta. The cantilever is reinforced by C-BAR-GFRP as top reinforcing material, and no bottom reinforcement is used. The experimental model was cast in May, 1997. Construction of the Crowchild

Bridge was scheduled to begin in the summer of 1997; therefore the right cantilever was selected to be tested first. during testing of the right cantilever, cracks formed on the top surface of the adjacent right span due to the induced negative bending moment in this region. Following testing of the right cantilever, the middle span was tested. This was done so that there would be no effect from other tests on the adjacent spans. Following test 2 on the middle span, test 3 was conducted on the left cantilever. This was done to expose the left and right interior spans to the same cracking conditions due to the induced negative bending moment from the adjacent cantilever tests. However, it should be mentioned that the failure load of the left cantilever was 875 kN, in comparison to an ultimate load of 500 kN for the right cantilever. Consequently, there was more cracking at the top surface of the left cantilever and its behaviour was affected to a greater extent than that of the right interior span. The left and right interior spans were tested last, both having incurred cracks from the adjacent cantilevers. The applied load in tests 4 and 5 was offset by 400 mm from the girder midspan, as shown in Figure 3-5. This was done to minimise the effect of the circumferential cracks that formed during test 2 on the middle span.

The test set-up for each span, including the instrumentation and load sequence, are discussed in the following sections.

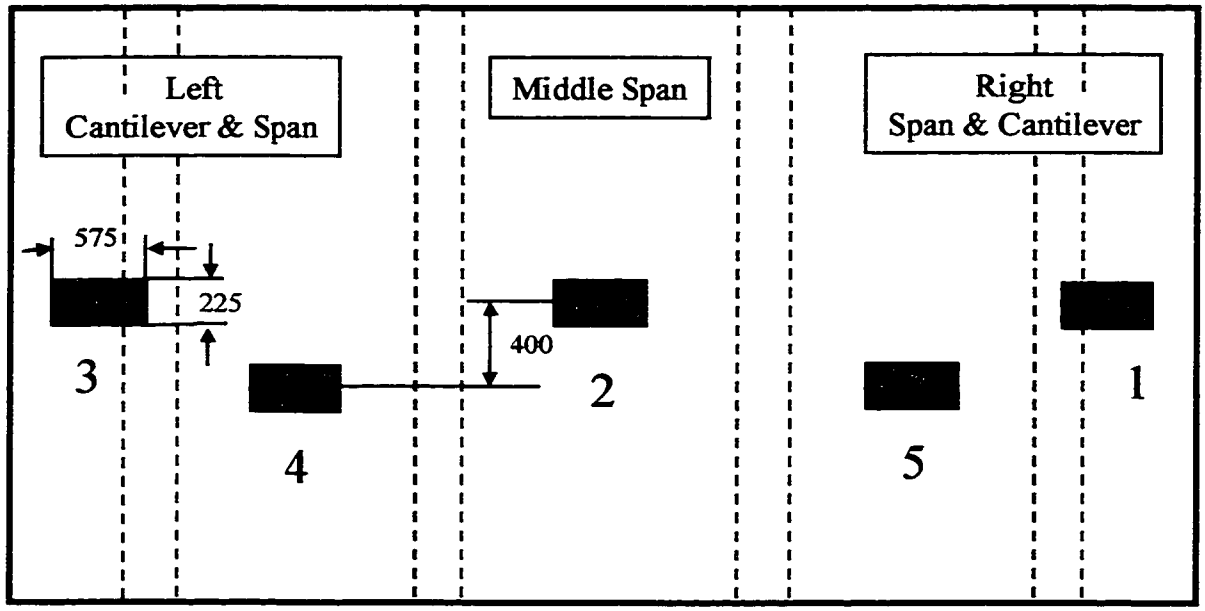

Figure 3-5: Applied Load Locations for Tests

3.2.1 Test 1 (Right Cantilever)

The right cantilever of the model was used to model the cantilever of the Crowchild Trail Bridge in Calgary, AB. The interior deck slabs of the Crowchild Trail Bridge were designed and constructed using the steel-free deck concept explained in Chapter 2 (Tadros *et al.*, 1998); therefore no internal steel reinforcement is used. Instead of flexural reinforcement, external steel straps are welded between supporting steel girders under interior spans to establish the arch action mechanism. The negative moment in the cantilevers was resisted by C-BAR-GFRP as top reinforcement, without bottom reinforcement. The purpose of test 1 was to verify the suitability of GFRP for this application in terms of structural capacity and serviceability requirements.

The right cantilever was loaded using three cycles up to two specified load levels. The first three cycles were from zero to 200 kN, which is in excess of twice the service load, followed by three cycles from zero to 400 kN. The cantilever was then loaded to failure, which occurred at a load of 500 kN, as shown in Figure 3-6.

The instrumentation used to monitor the behaviour of the right cantilever during the test consisted of a combination of electrical strain gauges, PI gauges, LVDTs, dial gauges, and demec points. As shown in Figure 3-7, the strain gauges were located above the face of the supporting girder. This location was chosen in order to capture the maximum values of tensile strain in the top reinforcement. The external instrumentation is shown in Figure 3-8. On the top surface of the slab, PI gauges were mounted above the girder face to measure crack width. LVDTs and dial gauges measured the total deflections of the slab and its supporting girder. Demec points and a mechanical gauge were used to measure the concrete tensile strains. An LVDT fixed to the end of the slab was used to measure the slip at the end of an exposed GFRP bar located directly below the load. On the bottom surface of the slab, PI gauges were used to measure the compressive strains at the girder face. Four PI gauges were mounted to the slab only, while four others were fixed to the face of the girder. These two configurations are shown in Figure 3-9, and are used to measure the strain at the critical section of the slab. Demec points were used to measure the strains at the extreme compression fibre to the end of the cantilever. The rotations

of the supporting girder and the deflections of the slab relative to the girder were measured using LVDTs, as shown in Figure 3-8.

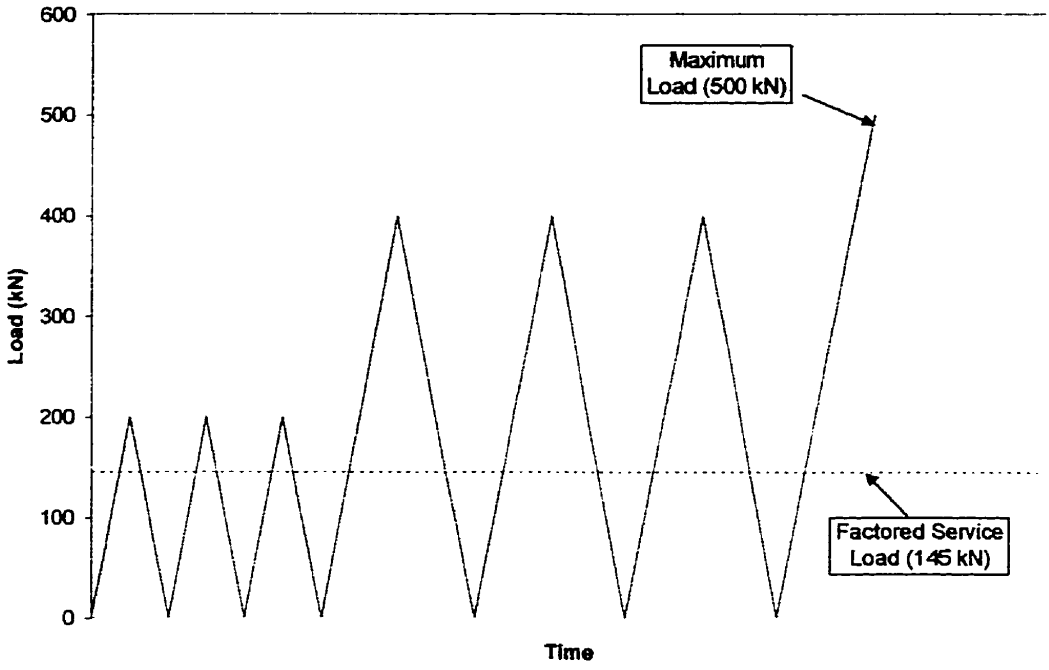

Figure 3-6: Load History for Right Cantilever

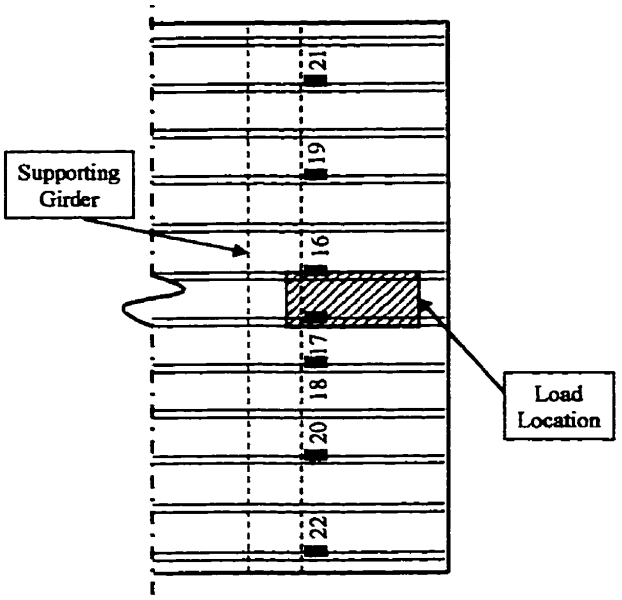

Figure 3-7: Strain Gauge Locations for Right Cantilever

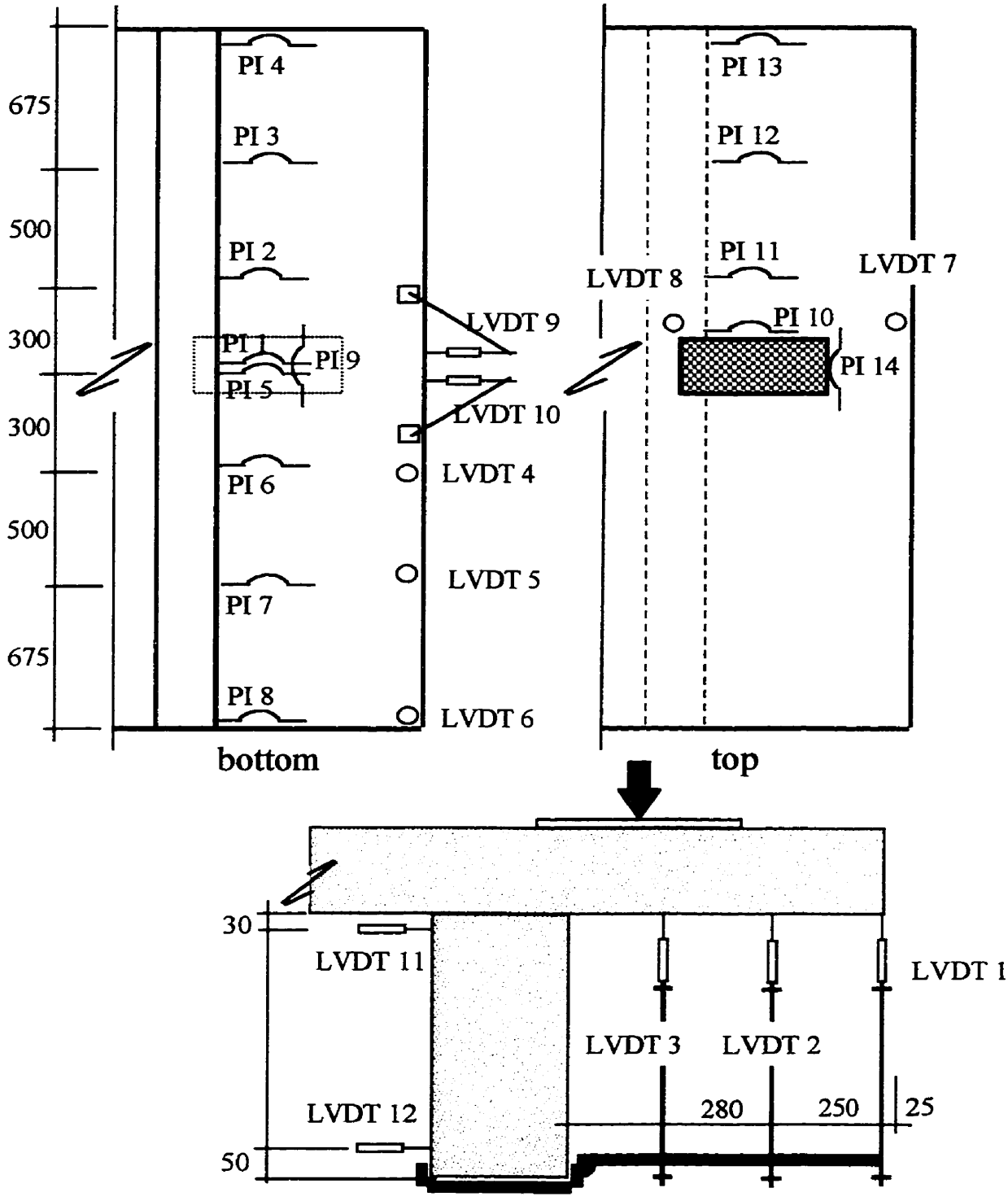

Figure 3-8: Instrumentation for Test 1

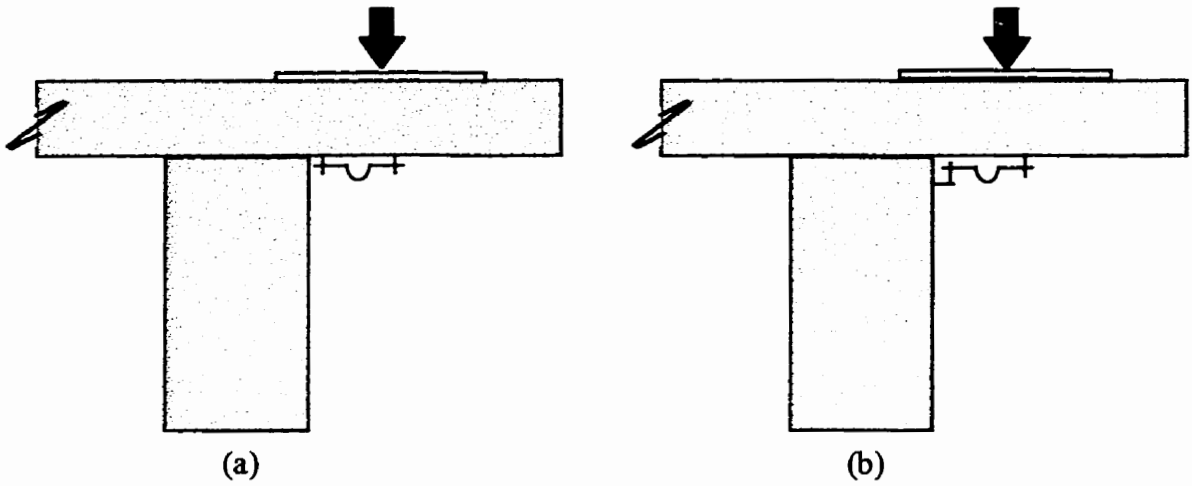

Figure 3-9: PI Gauge Configurations: (a) Slab Only; (b) Including Girder Face

3.2.2 Test 2 (Middle Span)

The middle span was loaded using three cycles up to each of five selected load levels, with each cycle starting at zero. The five load levels chosen for this test were 200 kN (more than twice the service load), 400 kN, 600 kN, 800 kN, and 1000 kN. After completion of the repeated load cycles, the slab was loaded to failure, as shown in Figure 3-10.

The instrumentation used to monitor the behaviour of the middle span during the test consisted of a combination of electrical strain gauges, PI gauges, LVDTs, and dial gauges. The electrical strain gauges, as shown in Figure 3-11 and Figure 3-12, were installed on the surface of the of the GFRP (top) and steel (bottom) reinforcing bars. They were positioned such that the maximum tensile and compressive strains in the reinforcement would be measured. External instrumentation, shown in Figure 3-13,

was used to measure behaviour at the surface of the concrete. On the top surface, PI gauges were used to measure the concrete compressive strains at the slab midspan. LVDTs were used to measure vertical deflections of the slab relative to the supporting girders. On the bottom surface of the slab, PI gauges were used to measure the concrete compressive strains and crack widths. LVDTs measured absolute vertical deflections of the slab and its supporting girders. Dial gauges and LVDTs were used to monitor the rotations of the supporting girders during the test.

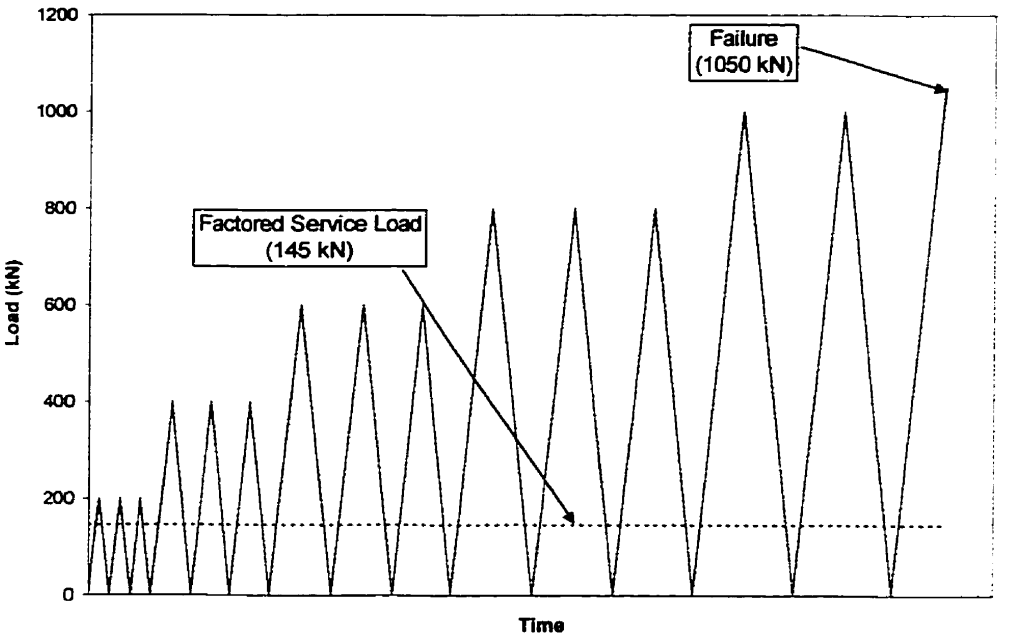

Figure 3-10: Load History For Middle Span

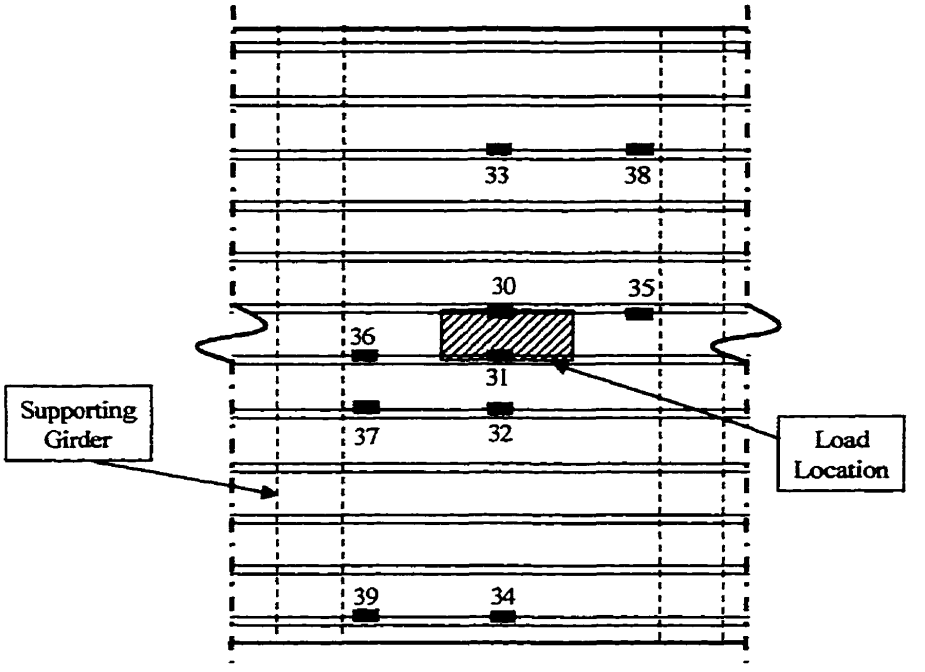

Figure 3-11: Strain Gauge Locations for Middle Span (Top Reinforcement)

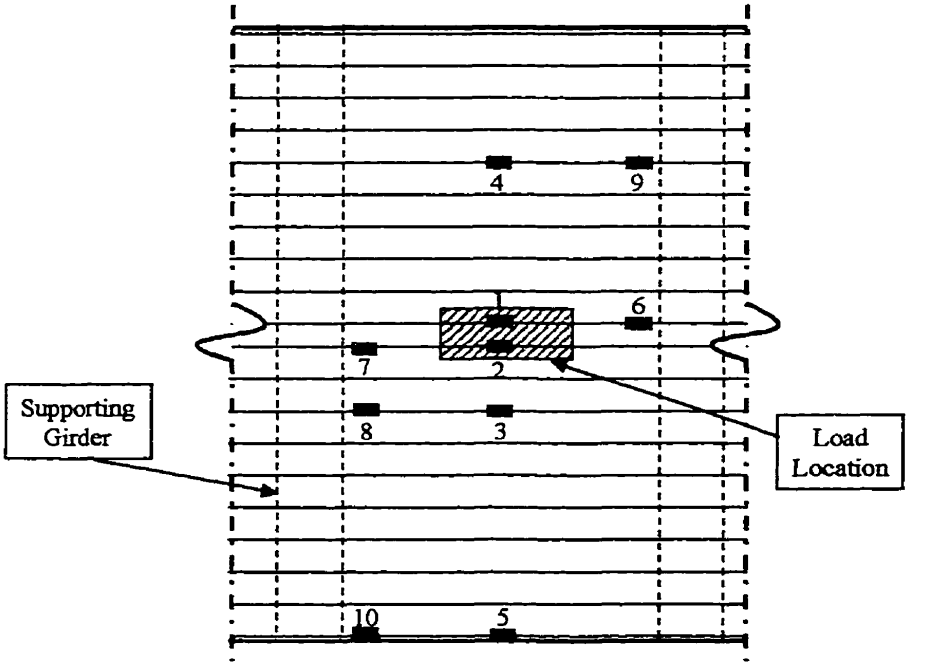

Figure 3-12: Strain Gauge Locations for Middle Span (Bottom Reinforcement)

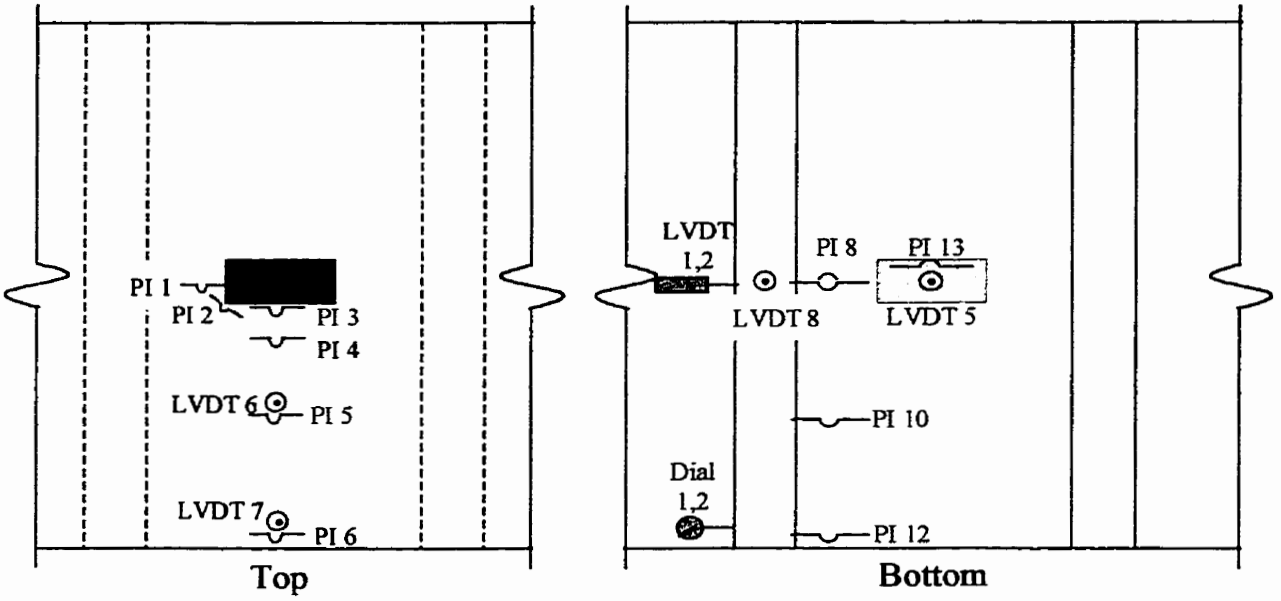

Figure 3-13: External Instrumentation Locations for Middle Span

3.2.3 Test 3 (Left Cantilever)

The loading history for the left cantilever was similar to that of the right cantilever. The cantilever was loaded using three cycles at each of two load levels. The first three cycles were from zero to 250 kN, followed by three cycles from zero to 400 kN. The slab reached a maximum load of 875 kN before failure. This loading history is shown in Figure 3-14.

The instrumentation for test 3 was very similar to that for test 1. The major difference was with respect to the internal electrical strain gauges. The right cantilever contained only top reinforcement, while the left cantilever had top and bottom reinforcement. As a result, the left cantilever utilised twice as many strain gauges, monitoring the strains in both the top and bottom reinforcement.

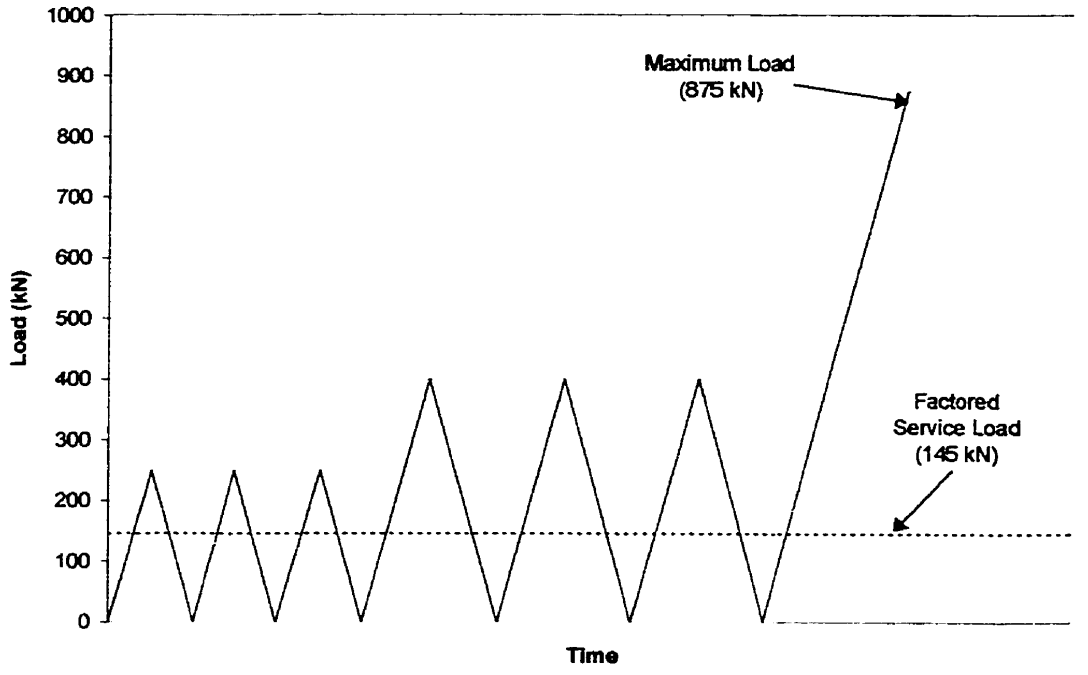

Figure 3-14: Loading History for Left Cantilever

3.2.4 Tests 4 and 5 (Left and Right Interior Spans)

The loading history for tests 4 and 5 was similar to that for test 2 (middle span). Load levels of 200, 400, 600, 800, and 1000 kN were used, followed by loading to failure. This loading history is shown in Figure 3-15.

The instrumentation for the left and right spans of the bridge deck slab model is shown in Figure 3-16. On the top surface of the slab, PI gauges were used to measure the compressive strains at the slab midspan. LVDTs were used to measure the vertical deflections of the slab relative to its supporting girders. On the bottom surface, PI gauges were used to measure the concrete compressive strains and crack

widths. LVDTs measured absolute vertical deflections of the slab and its supporting girders.

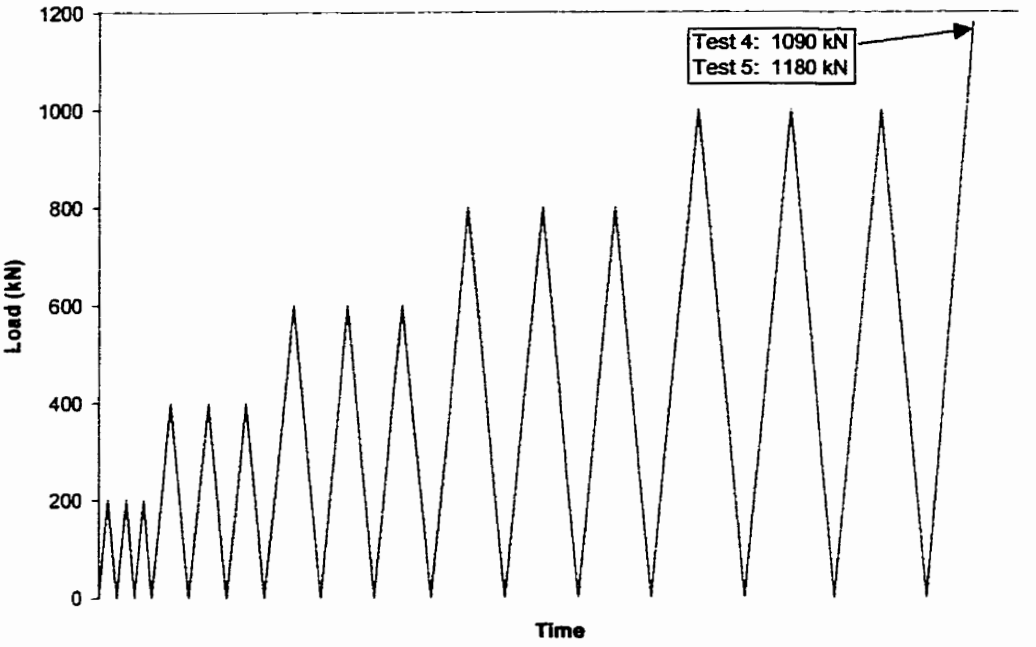

Figure 3-15: Load History for Left and Right Interior Spans

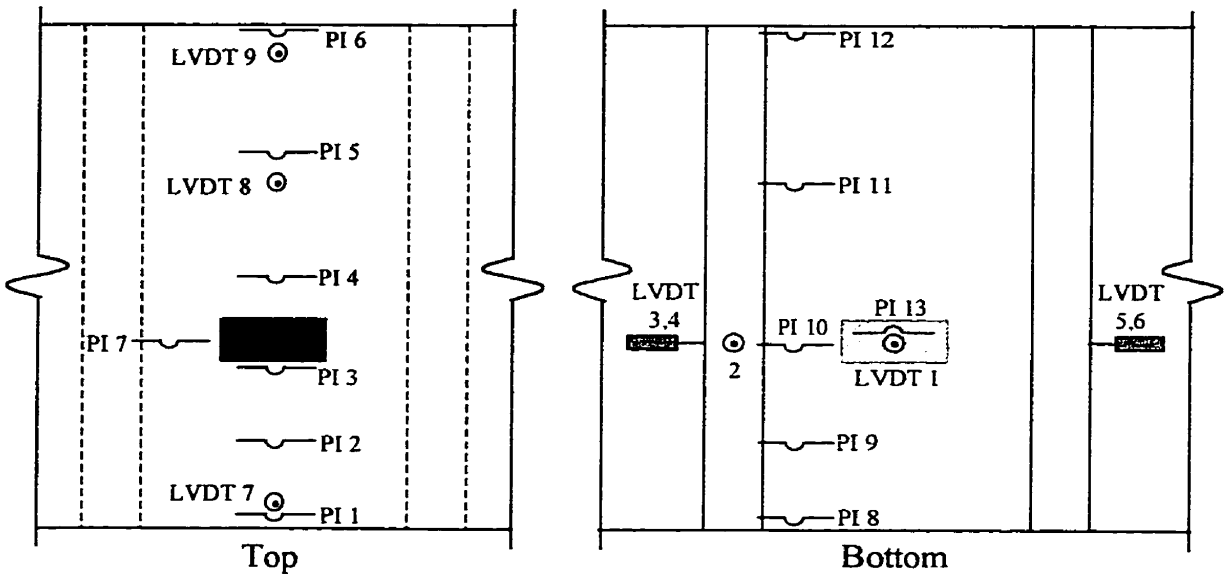

Figure 3-16: Instrumentation for Left and Right Spans

CHAPTER 4: TEST RESULTS AND DISCUSSION

4.1 INTRODUCTION

This chapter discusses in detail the five tests conducted on the hybrid-reinforced experimental model. The results for each test are presented and discussed in the order that the tests were conducted, with respect to the following aspects of behaviour:

- **Load Capacity and Mode of Failure**— For each test, the ultimate load capacity and mode of failure are presented and compared.
- **Load-Deflection Behaviour**— The relationship between applied load and slab (interior span or cantilever) deflection is discussed.
- **Crack Patterns**— The cracking load and its effect on the behaviour of the slab are presented. The spacing and direction of the cracks formed due to applied load are considered and compared for each test.
- **Strain Distribution**— The distribution of strain in the slab is an important aspect of its behaviour. Discussion of the strain distribution assists in determining the structural mechanisms acting in the slab.
- **Reinforcement Stresses**— Evaluation of the stresses in the reinforcement at service load is necessary due to the fact that glass fibres are attacked by the alkalinity present in normal concrete. It is important to determine whether or not the matrix that protects the fibres from this alkalinity cracks under service load.
- **Membrane Forces**— The internal normal forces that are developed in the interior spans are due to restraint of the supporting beams. These restraints are used to simulate the diaphragms that are used in actual bridges. These forces are calculated and their effect on behaviour is discussed.
- **Neutral Axis Depth and Internal Moment**— For further understanding of the behaviour of the slab, the variation of neutral axis depth and internal moment with applied load are evaluated and discussed.

- **Girder Rotations**—For the interior spans, the rotations of the girders are monitored to assist in determining the full effect of the end restraints used in the tests. For the cantilevers, girder rotations are used to isolate the various components of deflection.

4.2 MECHANICAL PROPERTIES OF FRP MATERIALS

Before the test results are presented, it is important to discuss the properties of the FRP materials that were used as reinforcement for this experimental model. A total of six GFRP specimens were tested, each with a length of 1000 mm. Because of the weakness of the FRP in compression perpendicular to the fibre orientation, the use of traditional grips in direct contact with the FRP was not possible. To solve this problem, the specimens were encased in 25 mm-diameter steel tubes, 300 mm on each end, using a high-strength epoxy. The forces from the grips of the testing machine were then transferred through the epoxy to the specimens without crushing the FRP.

The specimens were tested in a 30-kip-capacity testing machine equipped with an internal load cell. The strains on the FRP bars were measured using electrical strain gauges similar to those used on the experimental model.

Three ISOROD specimens were tested. All three specimens failed in tension, with an average strength of 655 MPa and an average elastic modulus of 39.3 GPa, as shown in Figure 4-1. The technical data provided by the manufacturer of ISOROD indicates an ultimate tensile strength of 674 MPa. Note that this is not a guaranteed

strength, but an average experimental value. The average elastic modulus of the ISOROD is 41 GPa according to the manufacturer.

Three C-BAR tension specimens were prepared and tested by A. Abdelrahman. Due to flaws in the pultrusion manufacturing process of the C-BAR, "joints" were formed in the bars at 200-mm intervals. These joints resulted in a visible offset in the centreline of the bars and initiated a premature failure. The average tensile strength that was measured was 473 MPa, with an average elastic modulus of 41.3 GPa, as shown in Figure 4-1. Bars without such visible flaws were tested at the University of Manitoba by ISIS Canada (1997) and achieved a minimum tensile strength of 640 MPa and a mean elastic modulus of 41 GPa. Information from the manufacturer gives a nominal ultimate tensile strength of 680 MPa with an elastic modulus of 42 GPa.

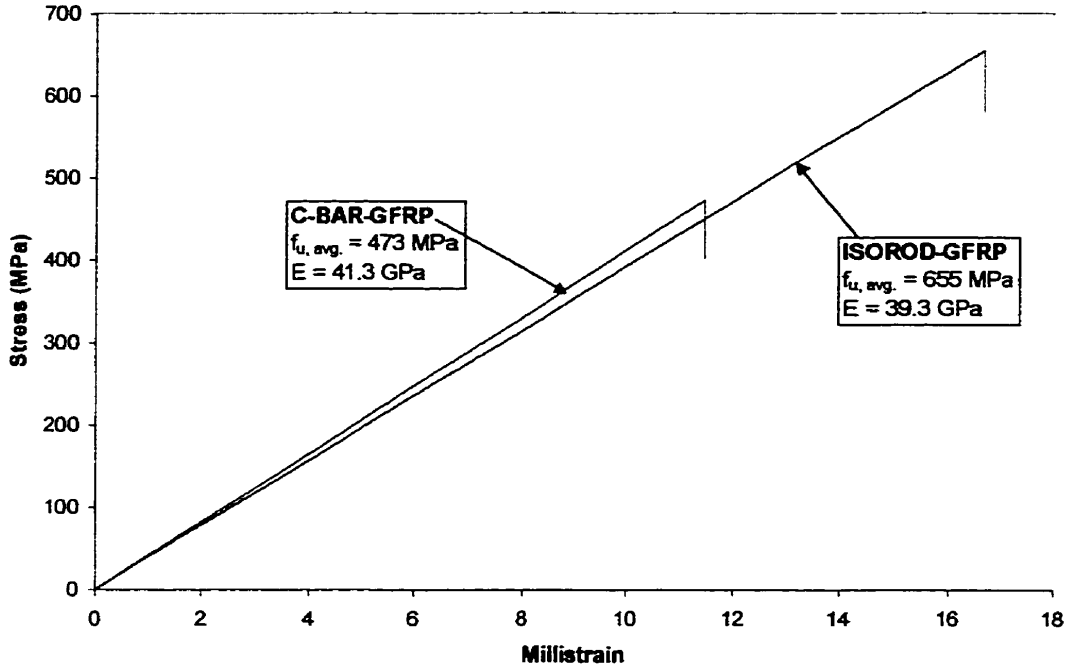

Figure 4-1: Typical Stress–Strain Curves for C-BAR and ISOROD GFRP Specimens

4.3 TEST 1 (RIGHT CANTILEVER)

The measured load–deflection relationship for the right cantilever is shown in Figure 4-2. Results indicate that the deflection of the cantilever is in the range of 1 mm at the service load of 72.5 kN. The current CSA Code limits the maximum deflection of a bridge cantilever to $l/180$, where l is the clear projection of the cantilever. In this model, l is 725 mm; therefore the maximum allowable deflection is 4.0 mm. Hence, the serviceability of the cantilever is satisfactory for short-term deflection.

As shown in Figure 4-2, the slope of the load–deflection curve for the second and third load cycles up to a load level of 200 kN is the same as that during the initial loading cycle. It was observed that the deflection increased suddenly at 275 kN. This increase coincides with the obvious measured slippage of the reinforcement, as shown in Figure 4-3 at the same load level. After 275 kN, the slope of the load–deflection curve decreased, reflecting a noticeable loss in stiffness, a result of continuous slipping of the reinforcement and cracking of the top surface of the slab. The slab failed at a maximum load of 500 kN due to slip of the reinforcement.

The crack pattern at failure is shown in Figure 4-4. The first crack occurred at 200 kN due to the negative bending moment in the adjacent span. It was expected that the first crack would appear on the adjacent span, as shown in Figure 4-5. The moment gradient between the point of load application and the peak moment is very high. In the adjacent span, however, the moment decreases at a slow rate from the peak. Therefore, at the face of the girder, the negative bending moment is higher in the adjacent span than in the cantilever. Circumferential cracks around the applied load began to develop at a load of 300 kN. At the maximum load of 500 kN, the slip increased from 0.45 to 0.8 mm. Based on a limiting value of 0.064 for the slip at the free end recommended by Ehsani *et al.*, the corresponding load is 270 kN for this cantilever as shown in Figure 4-3. It should be noted that the slip at service load was approximately 0.003 mm, which is 5% of the limiting value.

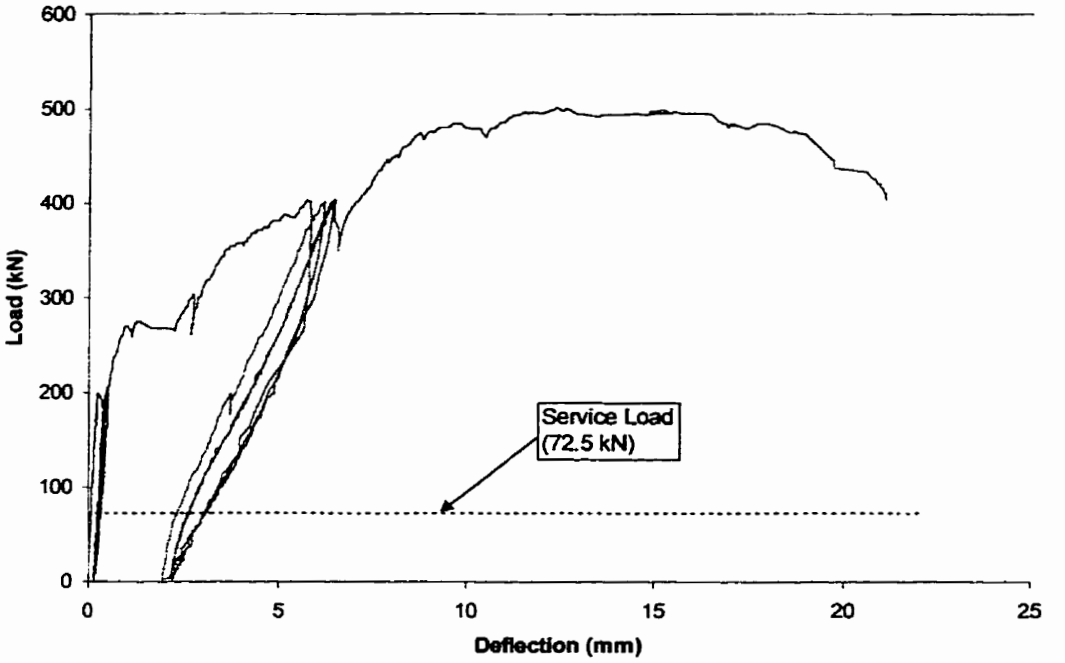

Figure 4-2: Measured Load–Deflection for Right Cantilever

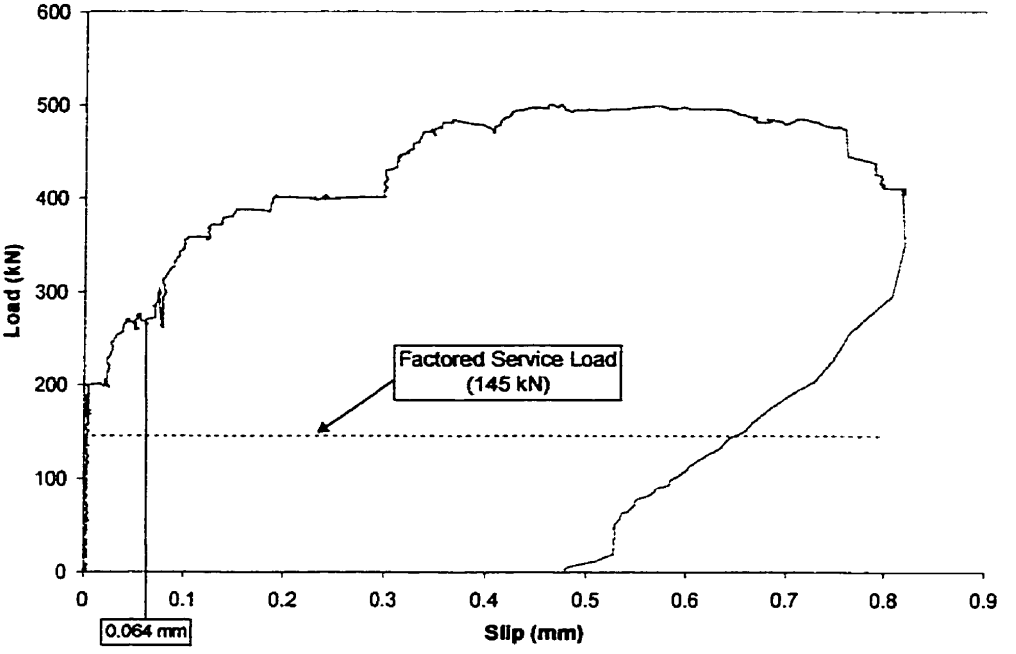

Figure 4-3: Load–Slip Relationship for Right Cantilever

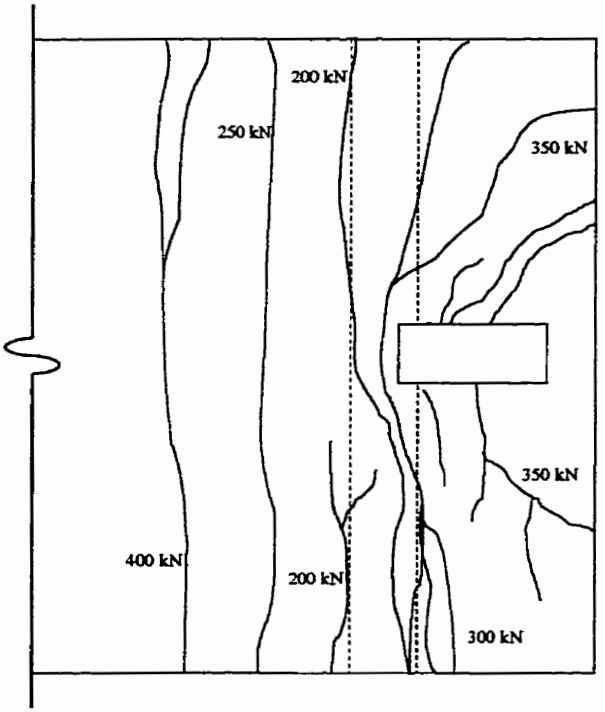

Figure 4-4: Crack Pattern for Right Cantilever, Top of Slab

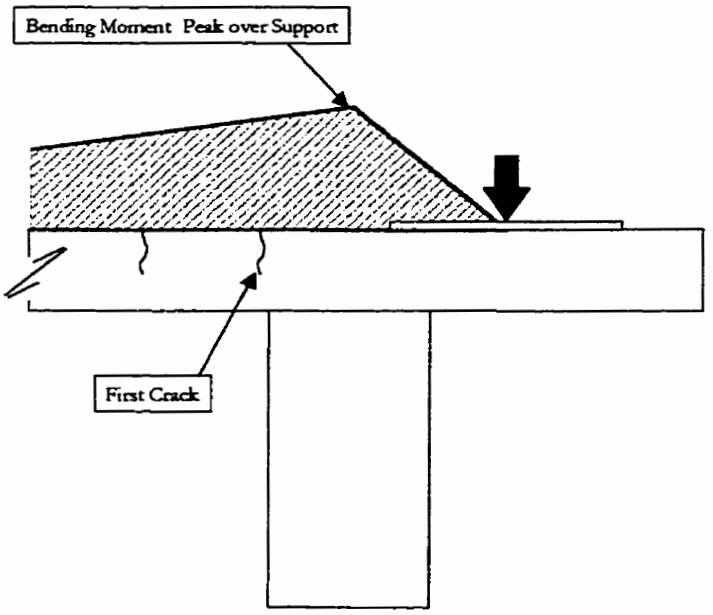

Figure 4-5: Location of First Crack in Adjacent Span

The maximum concrete compressive strain was measured at the bottom concrete surface at the location of the applied load. PI gauges mounted to the girder face at this location measured a value of 0.0038, as shown in Figure 4-6. The PI gauges mounted only to the surface of the slab did not capture the maximum strain and reached a peak value of 0.001, shown in Figure 4-7.

The maximum tensile strain of the C-BAR at the location of the applied load is shown in Figure 4-8. The tensile strain measured at failure was 0.0065, compared to a limiting value of 0.016 provided by the manufacturer. Therefore the ultimate strain in the C-BAR was not reached due to slip of the reinforcement which caused premature failure.

The strains at the top surface of the concrete were also measured using demec points and a mechanical gauge. The measured strains were very high near the girder face and decreased rapidly toward the edge of the cantilever, as shown in Figure 4-9. The maximum measured strain at 400 kN was 0.01 compared to a value of 0.004 measured by the strain gauge. This is indicative of debonding of the reinforcement near the location of the crack and the fact that the strains measured by the demec gauge include the crack widths. Figure 4-9 also shows the strain measurements at the bottom of the slab using a combination of demec and PI instrumentation. The maximum compressive strain in the concrete at 400 kN was 0.004 at the face of the girder, directly below the load. Again, the strains decrease rapidly with increasing distance from the girder.

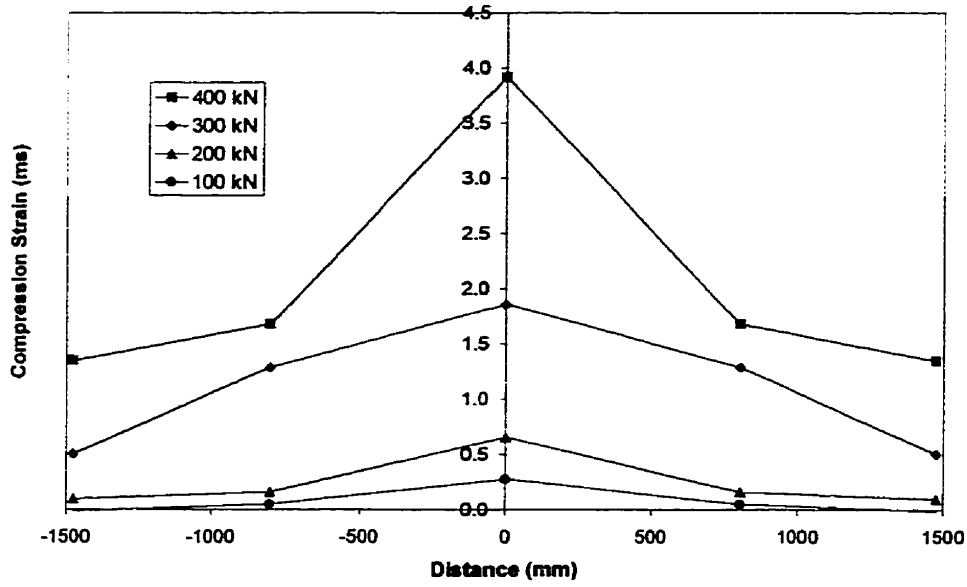

Figure 4-6: Compressive Strain in Concrete (including girder face)

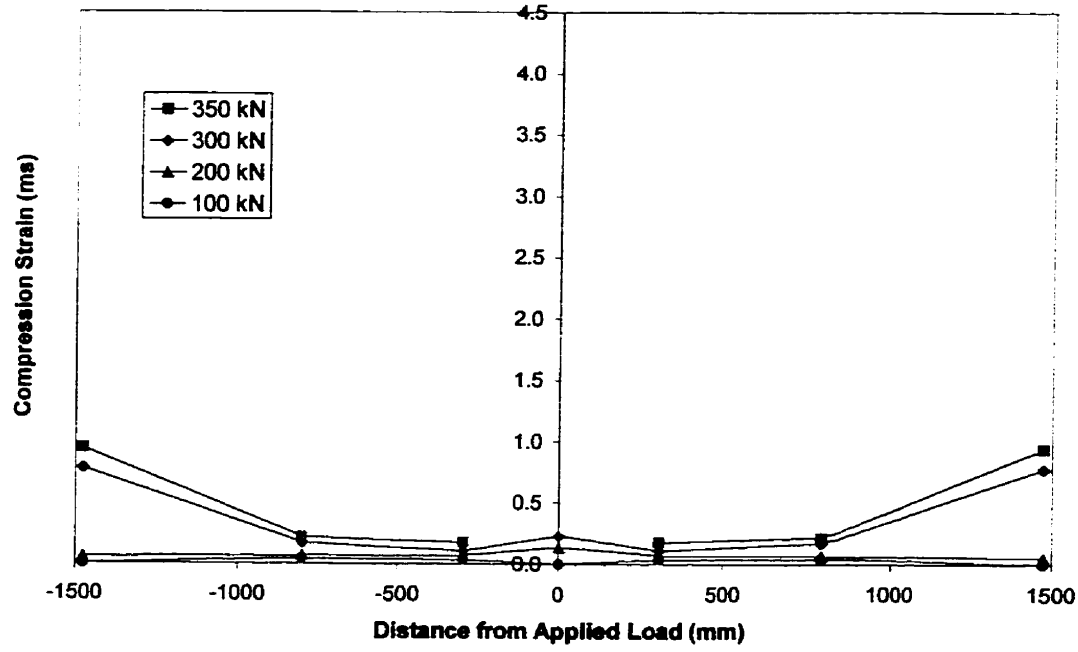

Figure 4-7: Compression Strain in Concrete (slab only)

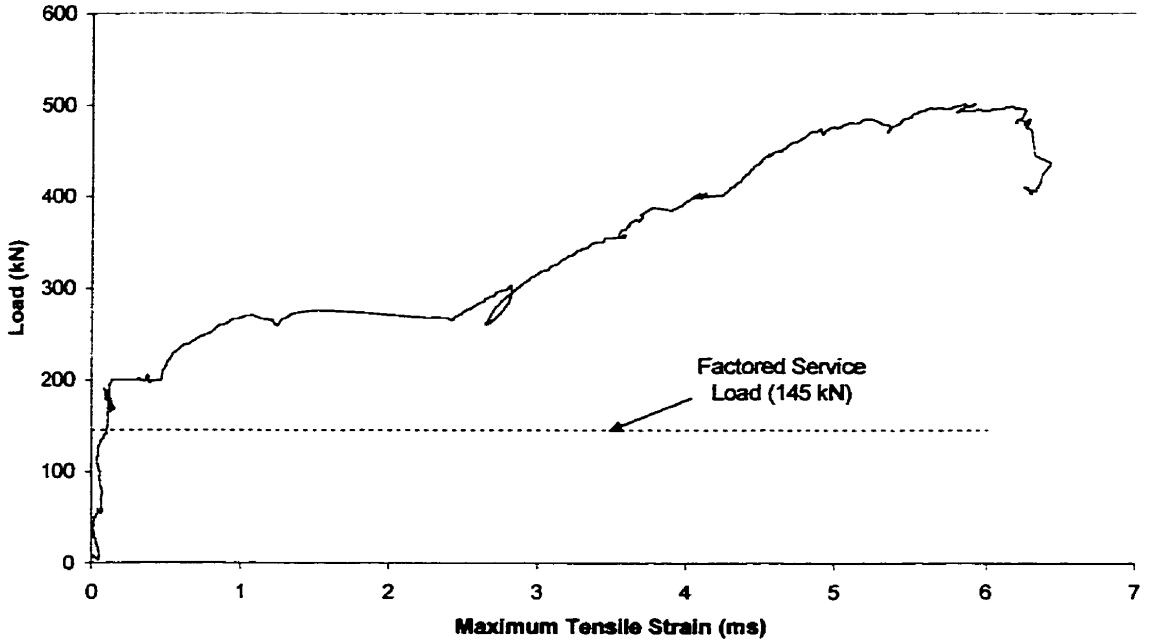

Figure 4-8: Load–Maximum Tensile Strain Relationship

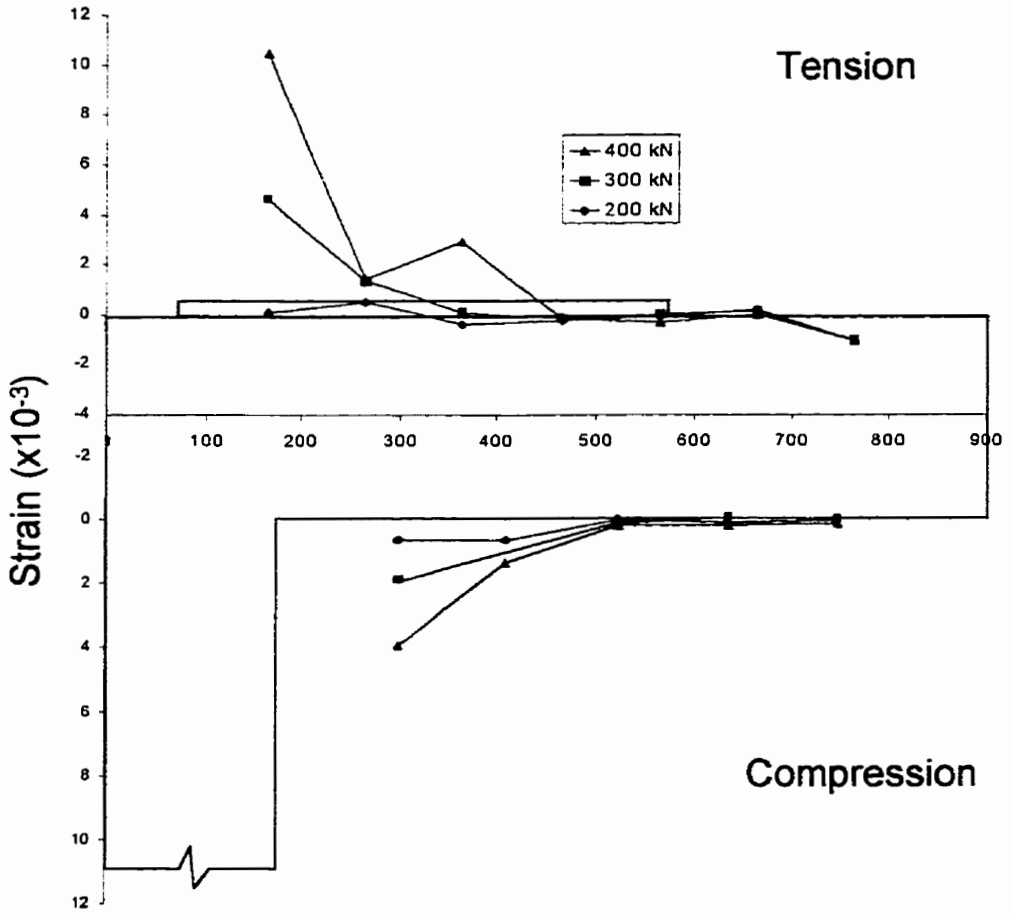

Figure 4-9: Strain Readings along Cantilever: Top and Bottom

The stresses in the reinforcement at service loads are an important concern when designing with GFRP reinforcement. The alkalinity present in normal concrete can attack the glass fibres over time, causing degradation of the reinforcement. This phenomenon will not occur if the matrix surrounding the glass fibres does not crack. GangaRao *et al.* assert that the polymer matrix in the FRP will not crack if the stress

in the reinforcement does not exceed 20% of ultimate. The design ultimate strength, as given by the manufacturer of C-BAR, is 680 MPa. The maximum measured strain in the reinforcement at service load was under 0.0002. Given an average elastic modulus of 42 GPa, the stresses in the reinforcement at service load were under 85 MPa, which corresponds to 12% of ultimate. This is indicative of satisfactory performance in terms of GFRP stresses under service load.

4.4 TEST 2 (MIDDLE SPAN)

The load–deflection relationship of the slab at the location of the applied load is shown in Figure 4-10. The deflection was measured at the bottom of the slab, directly below the load location. At the service load, the deflection of the slab was approximately 0.15 mm. Note that the shape of the load–deflection curve indicates that the stiffness of the slab did not decrease significantly before failure. The slab failed in punching shear at a load of 1050 kN. The distribution of deflection along the midspan of the slab relative to the girders is shown in Figure 4-11.

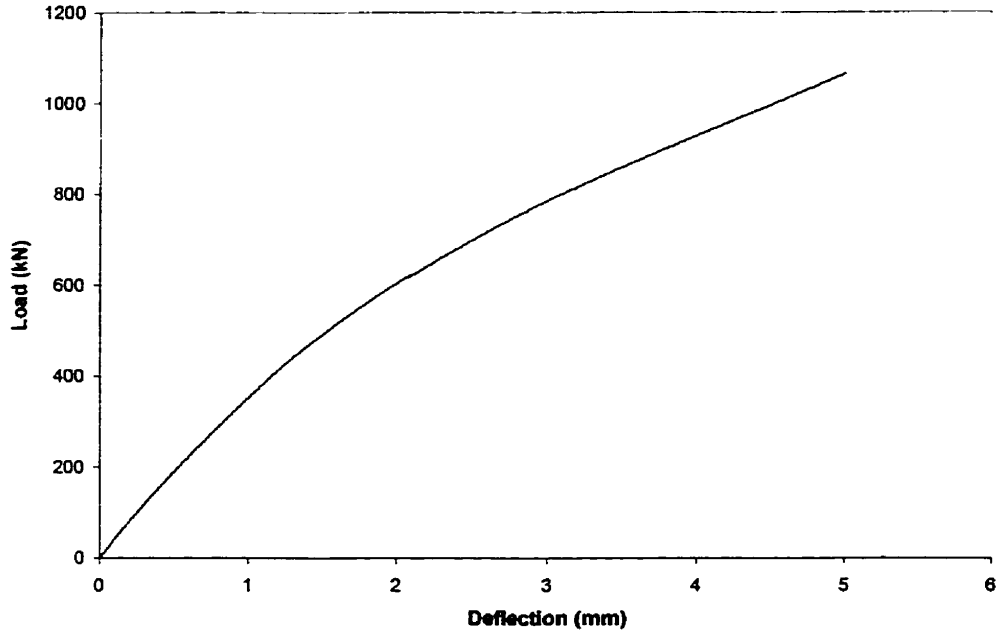

Figure 4-10: Load–Deflection Relationship for Middle Span

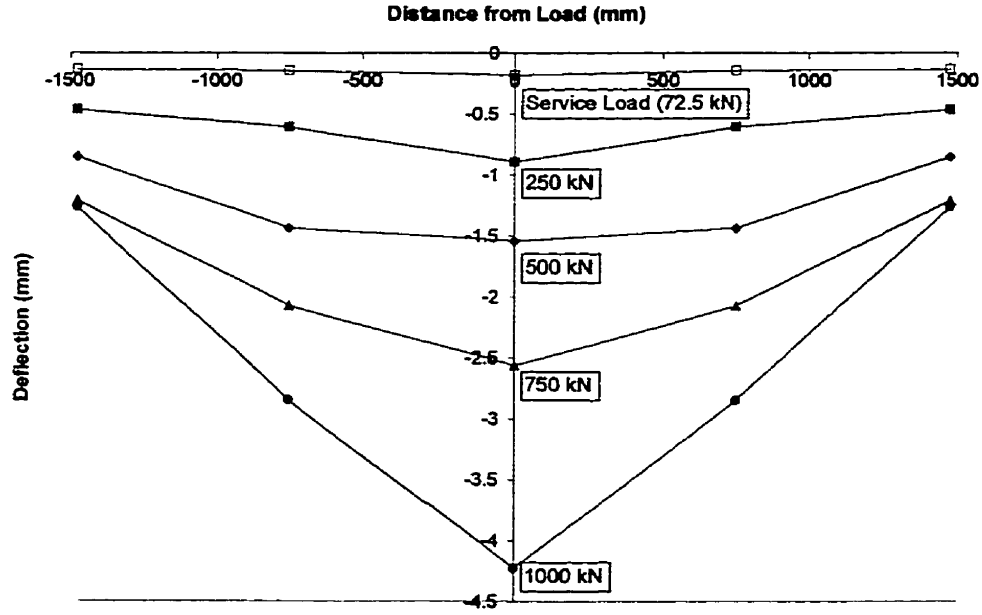

Figure 4-11: Deflection Distribution for Middle Span (Slab Midspan)

The crack pattern at failure for the top and bottom surfaces of the slab is shown in Figure 4-12 (a) and (b), respectively. The first crack was observed at a load level of 200 kN, at which point radial cracks on the bottom began propagating from the point of load application towards the edges of the slab. The cracks on the bottom surface of the slab are typical for punching shear failure, with circumferential cracks close to the load location and radial cracks forming between the load location and all edges of the slab. The major crack on the left side of the bottom view represents the location where the punching occurred. This crack did not form until failure.

Significant cracking did not occur on the top surface of the slab until a load of 400 kN was reached. At 600 kN, flexural cracks over the supporting girders formed, followed by further circumferential cracking at 800 kN. A photograph of the bottom surface crack pattern at failure is given in Figure 4-13.

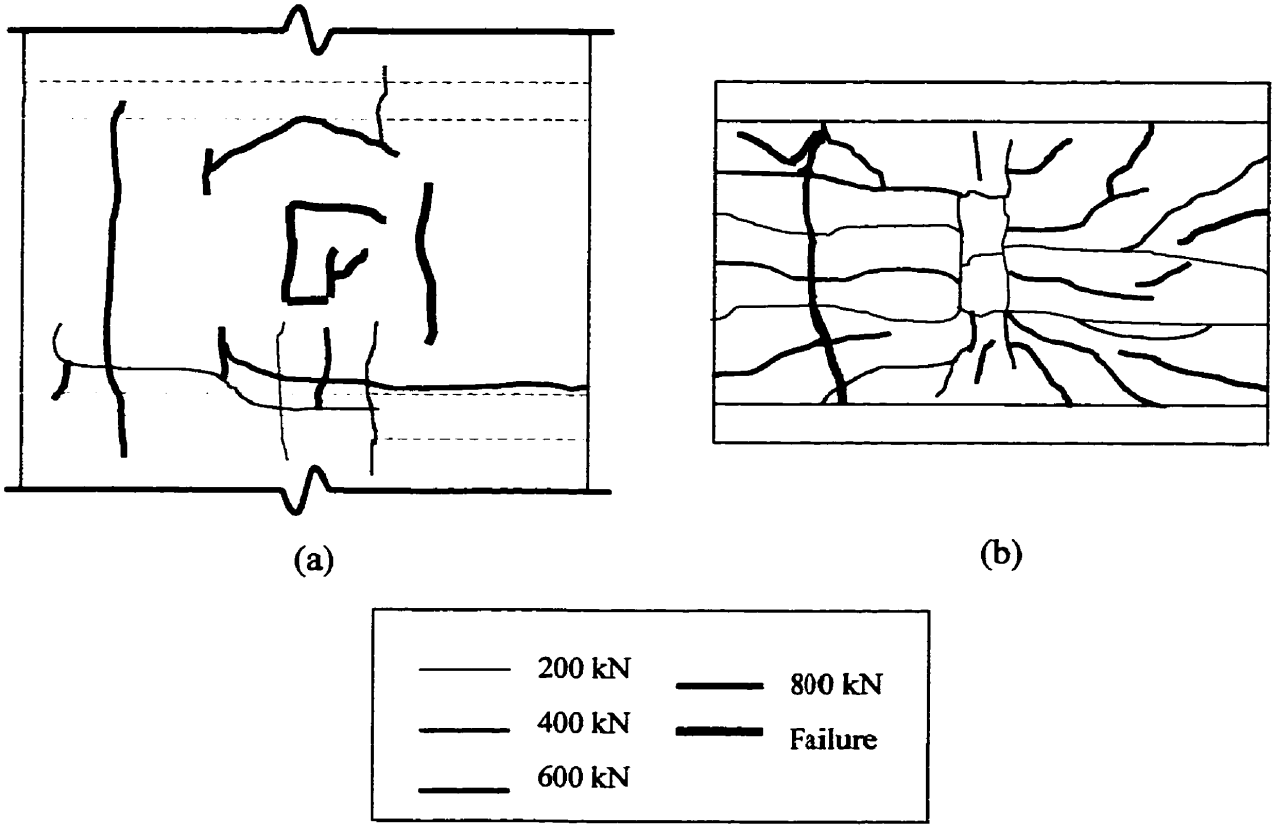

Figure 4-12: Middle Span Crack Pattern at Failure: (a) Top; (b) Bottom

Figure 4-13: Photograph of Middle Span Crack Pattern

The rotations of the slab's supporting girders were monitored to observe the behaviour of the girders and the effect of the restraining straps on the general behaviour of the girders and slab. The rotation of the girder midspan is shown in Figure 4-14, beginning with the 0-400 kN cycles until failure. Initial cycles are omitted because of instrumentation problems that occurred early in the test. The rotation of the girder at the support is shown in Figure 4-15, as measured by dial gauge readings at various load levels throughout the test. The increase in rotational stiffness of the girder after a load level of 500 kN may be attributed to increased bearing on the pins that support the steel straps. Once these pins experience bearing, the steel straps add to the resistance against support rotations.

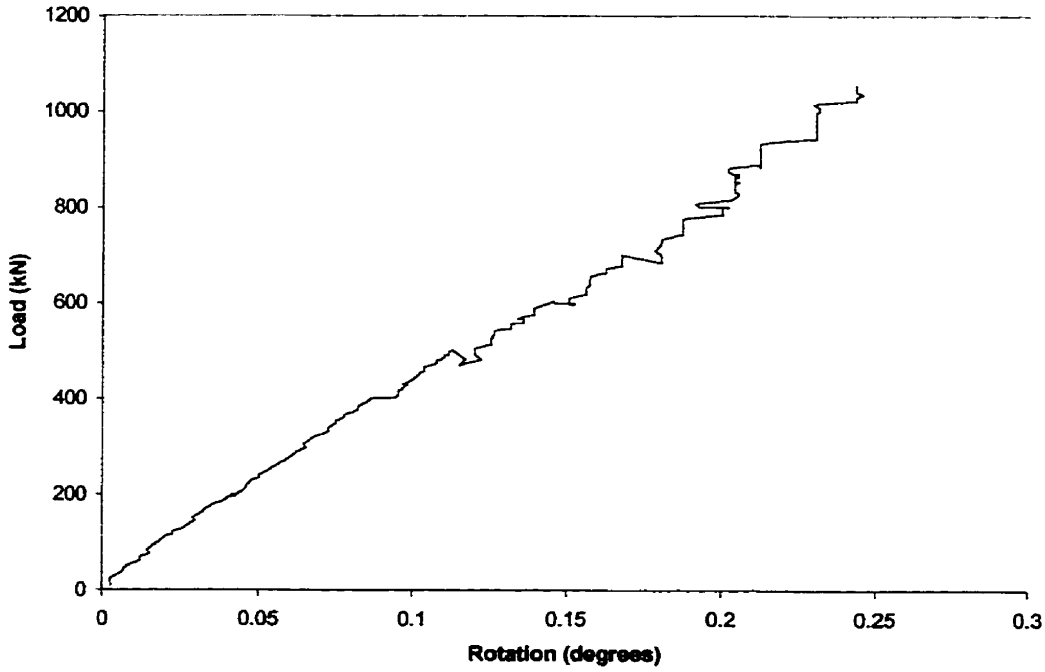

Figure 4-14: Girder Midspan Rotation

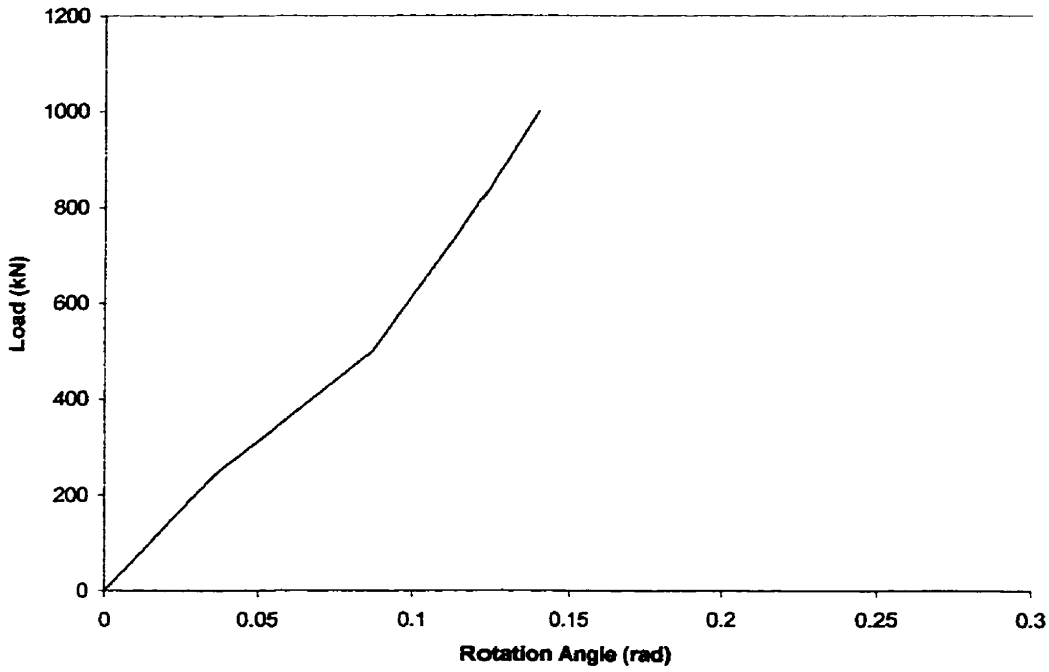

Figure 4-15: Girder Support Rotation (Measured by Dial Gauge)

The reinforcement strain distribution at the midspan of the slab is shown in Figure 4-16. In the top reinforcement, compressive strains at the load location increased as the load increased. Away from the location of the load, compressive strains became smaller with increasing load, eventually developing into tensile strains. In the bottom reinforcement, tensile strains at the load location increased as the load increased. Likewise, tensile strains away from the location of the load increased with increasing load. The maximum tensile strain in the bottom reinforcement before failure was 0.002, approaching, but not achieving, yield of the steel reinforcement.

The strains in the reinforcement along the girder face are shown in Figure 4-17. Throughout the test, the bottom reinforcement strains remained almost constant,

with relatively small compressive strains at the load location and small tensile strains away from the loaded area. The top reinforcement at the load location experienced significant tensile strains as the load increased, whereas locations greater than 750 mm from the load experienced low tensile strains. The top gauge readings at a location 375 mm from the load showed higher values than those at the load location. This behaviour may be due to the proximity of the gauge to a crack at the top surface of the slab. This led to local debonding of the reinforcement and consequently a higher strain reading. It is important to note that the entire section is in tension at loads in excess of 500 kN. This is true for both midspan and girder face locations.

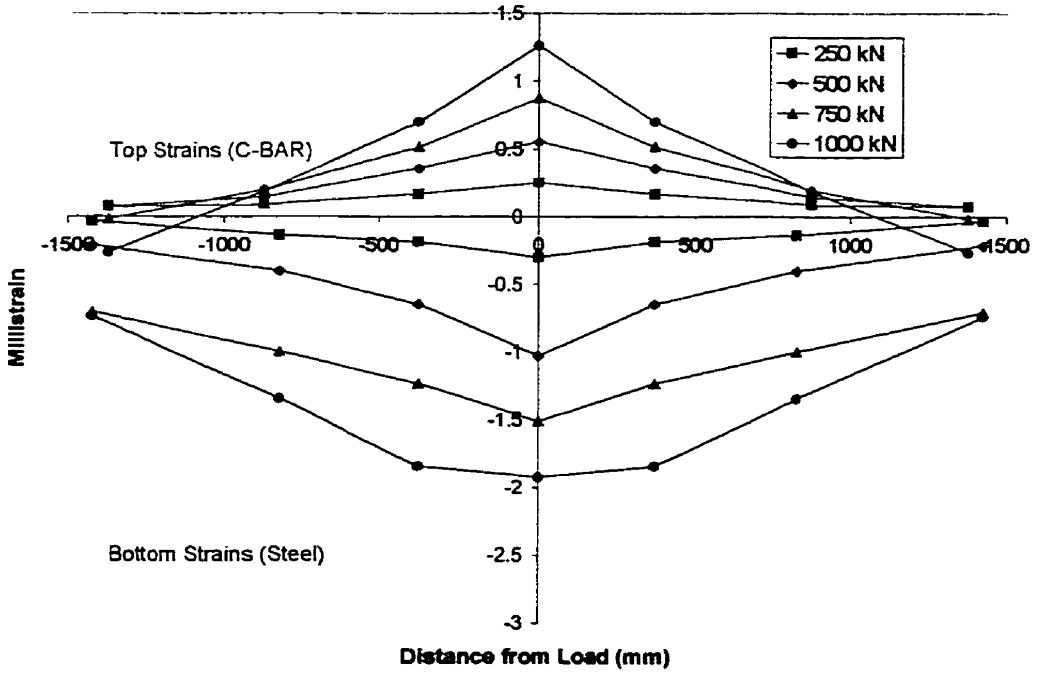

Figure 4-16: Reinforcement Strain Distribution, Slab Midspan

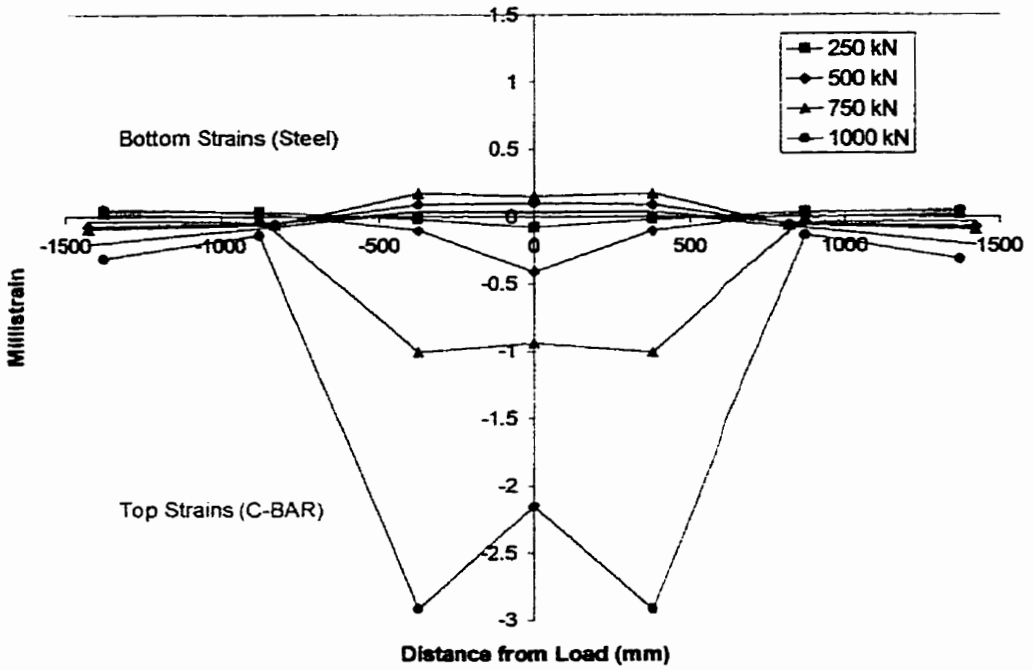

Figure 4-17: Reinforcement Strain Distribution, Girder Face

The interior spans of this model utilised end restraints to simulate the response of the cross-girder diaphragm of an actual highway bridge. These secondary girders act as stiffeners and prevent the main girders from rotating due to flexural action under applied loads. Without these restraints, the girders would move outward under the tension induced at the bottom fibre of the slab. When this movement is prevented, compressive normal forces, known as membrane forces, are induced on the section. The magnitude of the compressive membrane force is equal to the sum of compression in the concrete and tension in the reinforcement.

Figure 4-18 shows the calculation of stresses in a concrete section according to Collins and Mitchell (1997). Values for the strains in the top FRP and bottom steel

reinforcing bars were measured using electrical strain gauges. Using a linearly elastic relationship for the FRP and equivalent stress block factors α_1 and β_1 for the concrete in compression (an assumed parabolic stress–strain relationship), the compressive and tensile forces were calculated. Parameters α_1 and β_1 are calculated such that the magnitude and location of the resultant force are the same in the equivalent stress distribution as in the actual distribution. The resultant magnitude requirement is given by Equation 4–1, as follows:

$$\int_0^c f_c b dy = \alpha_1 f'_c \beta_1 c b \qquad \textbf{(4–1)}$$

Assuming a parabolic stress–strain relationship for concrete in compression, (4–1) reduces to

$$\alpha_1 \beta_1 = \left(\frac{\varepsilon_c}{\varepsilon_c'}\right) - \frac{1}{3}\left(\frac{\varepsilon_c}{\varepsilon_c'}\right)^2 \qquad \textbf{(4–2)}$$

The requirement that the location of the resultants be the same is given by

$$\bar{y} = \frac{\int_0^c f_c b y dy}{\int_0^c f_c b dy} = c - 0.5\beta_1 c \qquad (4\text{–}3)$$

Again, assuming a parabolic stress–strain curve, as well as a constant width, b, (4–3) reduces to

$$\beta_1 = \frac{4 - \left(\frac{\varepsilon_c}{\varepsilon_c'}\right)}{6 - 2\left(\frac{\varepsilon_c}{\varepsilon_c'}\right)} \qquad (4\text{–}4)$$

where ε_c' = concrete strain at $f_c = f_c'$
ε_c = extreme compressive fibre strain

The tensile and compressive forces are summed (based on a 1-metre width of slab), and the resultant normal force is the membrane force intensity per unit width. If the resultant is zero, then the membrane forces are also zero and consequently the concrete section is in equilibrium.

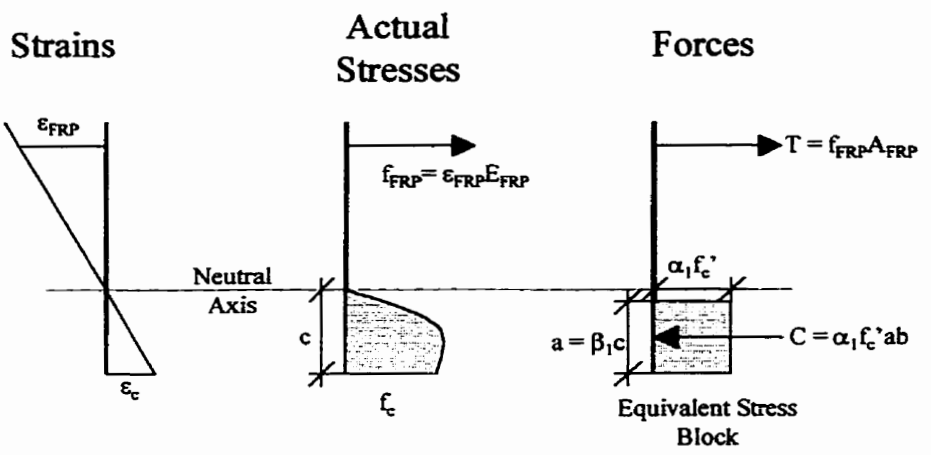

Figure 4-18: Calculation of Forces in Concrete Section

Figure 4-19 shows the distribution of the membrane forces along the midspan of the slab. Analysis shows that at an early stage in the test, the entire midspan of the slab experiences net compressive membrane forces, with a sharp peak at the location of the applied load . As the load exceeds 750 kN, however, sections at a distance greater than 1000 mm from the load location are subject to axial tension. This behaviour might be attributed to the horizontal reaction in the supporting girders. While the girders are pushed outward at their midspan due to the applied load, they are held in place at their ends by the slab, which is subjected to axial tension. This phenomenon is shown schematically in Figure 4-20.

Figure 4-21 shows the distribution of membrane forces along the girder face. The forces developed along this line were very small relative to those developed along the midspan of the slab. The behaviour, however, is similar to that at the midspan, with

net compressive forces at lower loads, and tensile forces far away from the load at loads above 750 kN.

The relationship between membrane force per unit width and applied load at the location of the load is shown in Figure 4-22. The compressive membrane force increases with increasing load through the entire loading range up to failure. Figure 4-23 shows how the membrane forces vary with applied load at the girder face. At this location, the membrane force is compressive and increases up to an applied load of 785 kN, then decreases. At a load level of 800 kN, the membrane force decreases suddenly. This horizontal portion of the membrane force curve represents crack stabilisation during the 800-kN cycles.

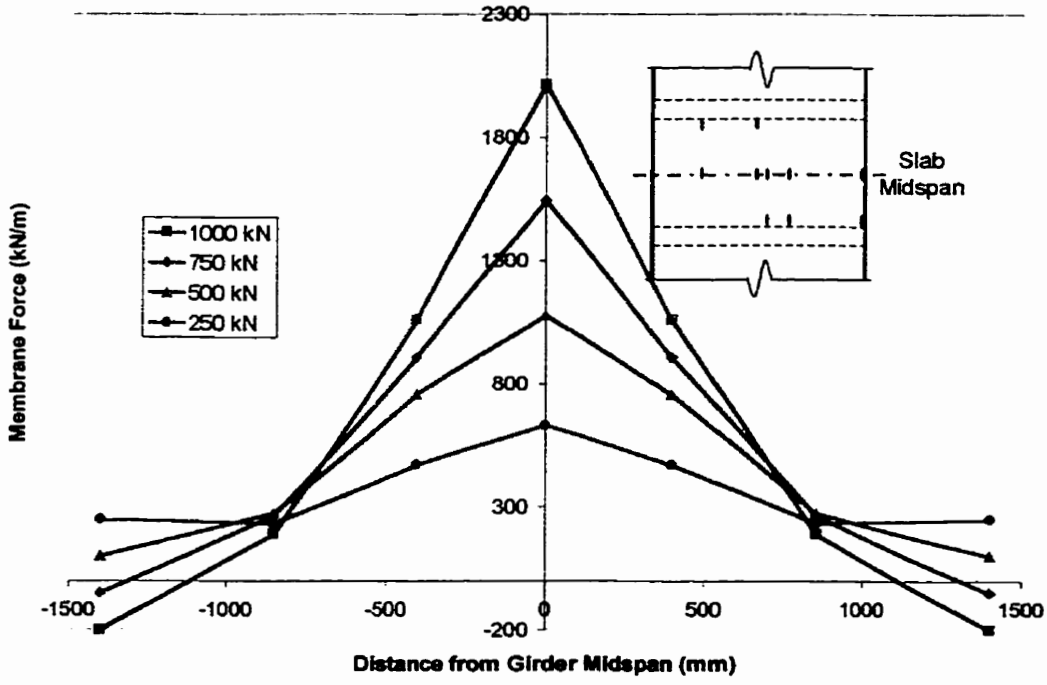

Figure 4-19: Membrane Force Distribution at Slab Midspan

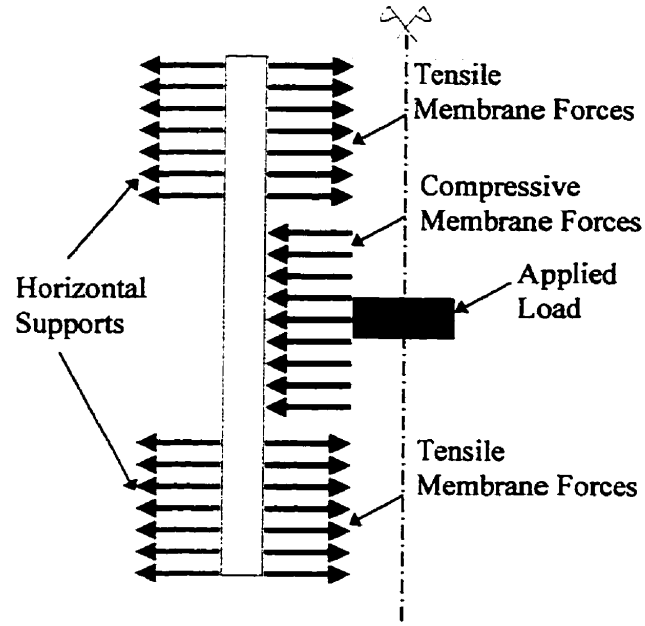

Figure 4-20: Schematic Representation of Membrane Force Distribution

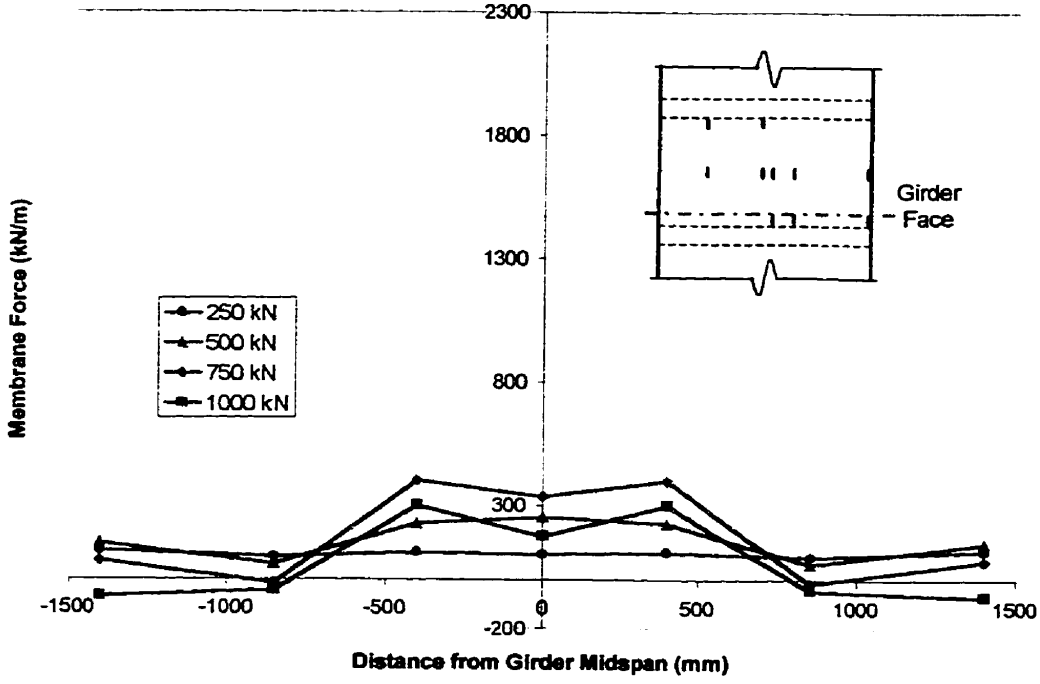

Figure 4-21: Membrane Force Distribution at Girder Face

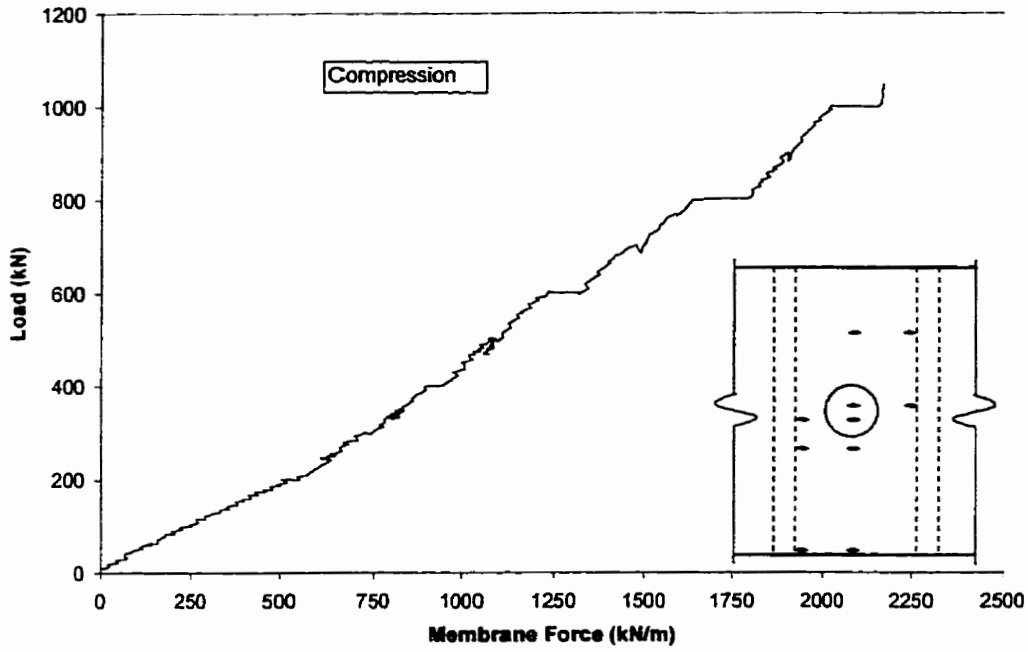

Figure 4-22: Applied Load versus Membrane Force per Unit Width (Slab Midspan)

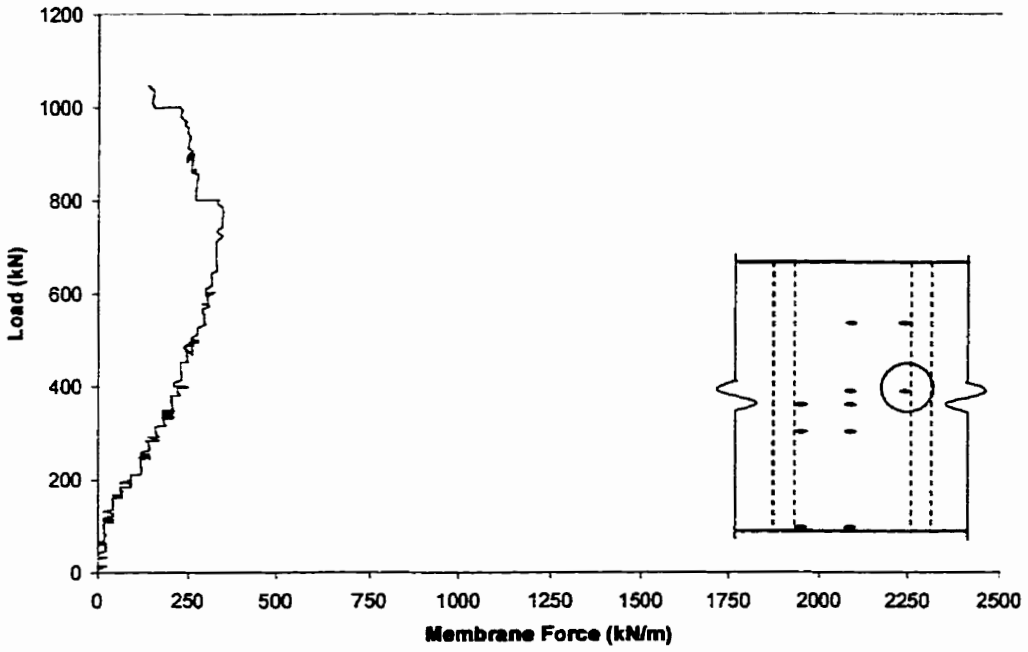

Figure 4-23: Applied Load versus Membrane Force per Unit Width (Girder Face)

Figure 4-24 shows the variation of neutral axis depth as related to the applied load at the midspan of the slab. Before cracking, the neutral axis is close to the centroid of the gross section, approximately 100 mm from the top of the slab. After cracking, the area of concrete in compression decreases, causing the depth of the neutral axis to decrease to approximately 80 mm from the top as the reinforcement resists the tension released by the concrete. Further loading causes the neutral axis depth to increase slightly, corresponding to an increase in compressive stresses in the concrete.

Figure 4-25 shows the neutral axis variation with applied load at the face of the supporting girder. At loads below 400 kN, the neutral axis is located approximately at the centroid of the section. There is a sharp increase in neutral axis depth at a load level of 400 kN, which corresponds with the cracking at the top surface of the slab at the girder face. As the applied load is increased, the depth of the neutral axis increases steadily. At 800 kN, the neutral axis is at the location of the bottom steel reinforcement, and remains at this level until failure, as evidenced by the tensile strains measured in the bottom reinforcement at these loads. It should be noted that at loads below 160 kN, the measured values from the strain gauges at this location were too low to give meaningful data.

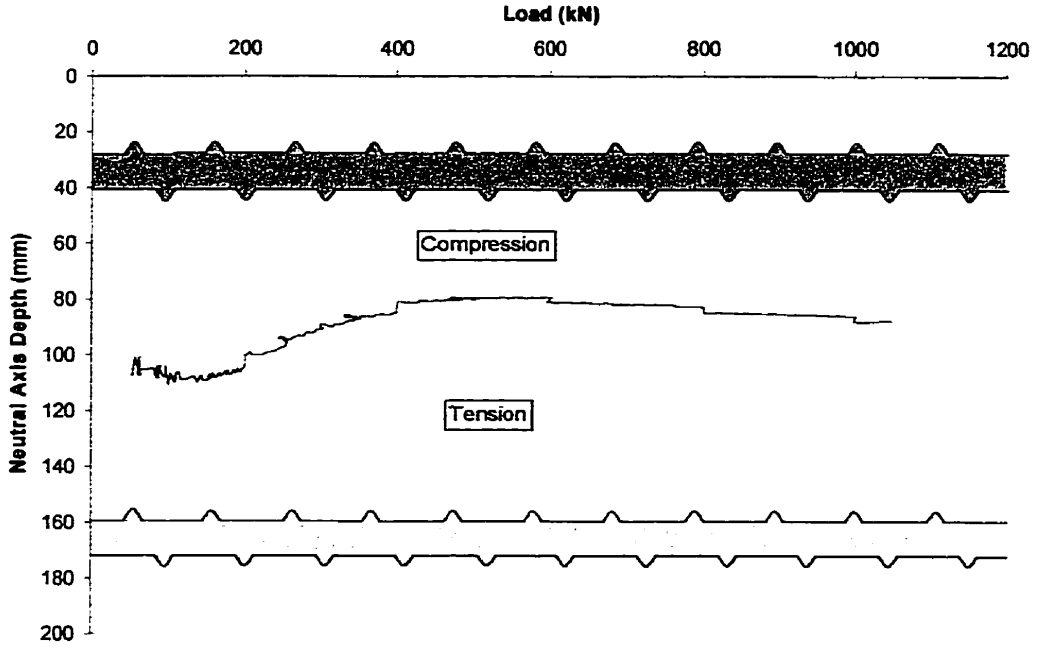

Figure 4-24: Variation of Neutral Axis Depth with Applied Load (Slab Midspan)

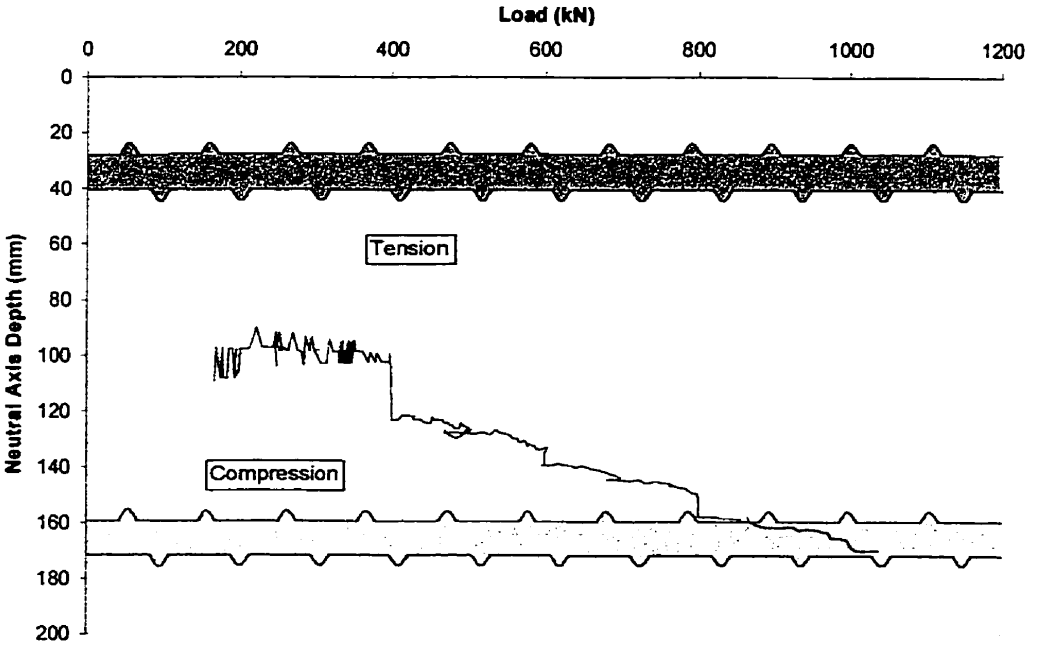

Figure 4-25: Variation of Neutral Axis Depth with Applied Load (Girder Face)

The membrane forces are applied through the plastic centroid. The plastic centroid is defined as "the centroid of resistance of the section if all the concrete is compressed to the maximum stress and all the steel is compressed to the yield stress, with uniform strain over the section. In other words, [it] is the point of application of the external load P_0 that produces an axially loaded condition at failure" (Park and Paulay, 127). The plastic centroid is calculated by taking the failure load of each component of the cross-section, multiplying it by the distance to the centroid of each component, and dividing their sum by the total failure load in the cross-section, as shown in Table 4–1.

Table 4–1: Calculation of Plastic Centroid

Component	Area (mm^2)	Strength (MPa)	Failure Load (F, kN)	Centroid (y_{bar}, mm)	$F*y_{bar}$
Concrete	200000	43	8600	100	860000
GFRP	1413.7	500	706.86	32.5	22972.95
Steel	1178.1	400	471.24	167.5	78932.7
Σ			9778.1		961905.65
Plastic Centroid = $\Sigma F*y_{bar}/\Sigma F$ = 961905.7/9778.1= 98.373 mm					

Once the location of the plastic centroid is determined, the internal moment can be calculated by summing the products of the forces in the section and their respective moment arms. The internal moment was calculated at the midspan of the slab and at the face of the supporting girder. Once the membrane forces in the section are calculated as discussed on page 4-24, the induced moment in the section is calculated as follows:

First, the moment is calculated about the tensile reinforcement (refer to Figure 4-26):

$$M_t = C\left(d - \frac{\beta_1 c}{2}\right) \qquad (4\text{–}5)$$

The eccentricity of the induced membrane force, e_t', is then calculated based on the locations of the forces in the section, as shown in Figure 4-26, and given in Equations 4–6 to 4–8:

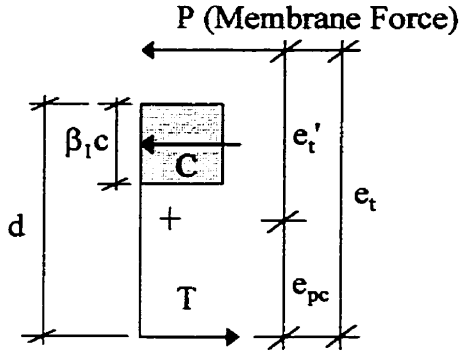

Figure 4-26: Calculation of Eccentricities in Concrete Section

$$e_t = \frac{M_t}{P} \qquad (4\text{–}6)$$

$$e_{pc} = d - y_{pc} \qquad (4\text{–}7)$$

$$e_t' = e_t - e_{pc} \qquad (4\text{–}8)$$

Once the eccentricity of the force P is calculated relative to the location of the plastic centroid in the section, the induced moment on the section can be calculated, as shown in Equation 4–9:

$$M = P \times e_t' \qquad (4\text{–}9)$$

Figure 4-27 shows the applied load versus induced moment relationship for the slab midspan. It is an approximately linear relationship throughout the loading range. This is expected since the neutral axis at this location did not vary significantly with load. As a result, an increase in applied load results in a proportional increase in tensile and compressive forces. In Figure 4-28, it can be seen that the induced moment at the girder face increases with applied load up to approximately 800 kN, then remains almost constant until failure. This behaviour is due to the fact that the neutral axis dropped because of crack development in the concrete. When the neutral axis drops, the area of concrete in compression decreases, eventually to the point that both top and bottom reinforcement are subject to tension. Since a majority of the section experienced tension at high loads, the resulting internal moment did not increase.

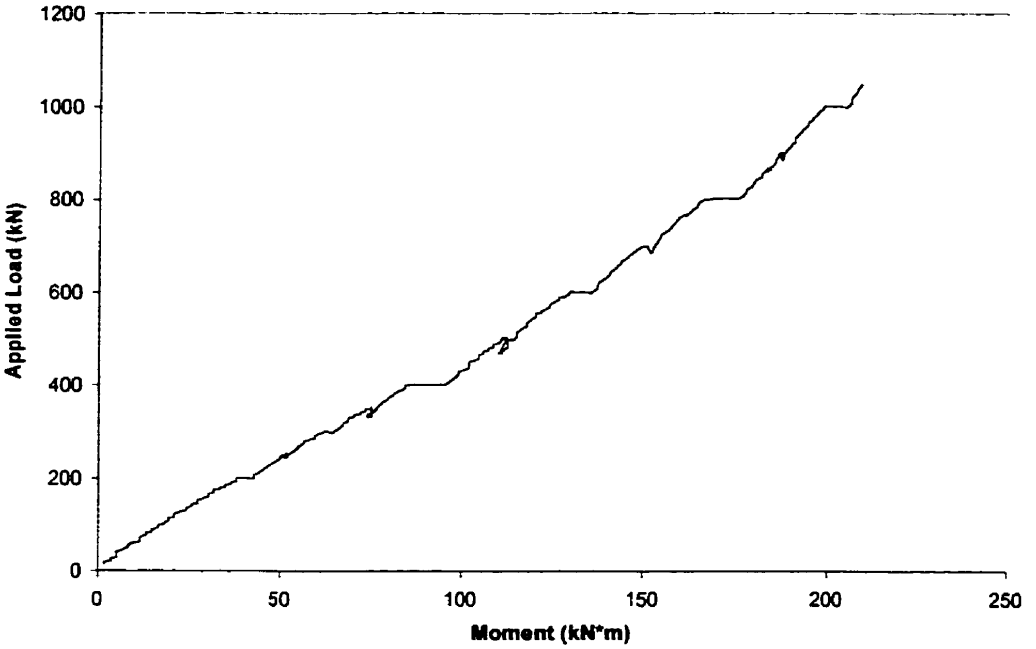

Figure 4-27: Variation of Internal Moment with Applied Load (Slab Midspan)

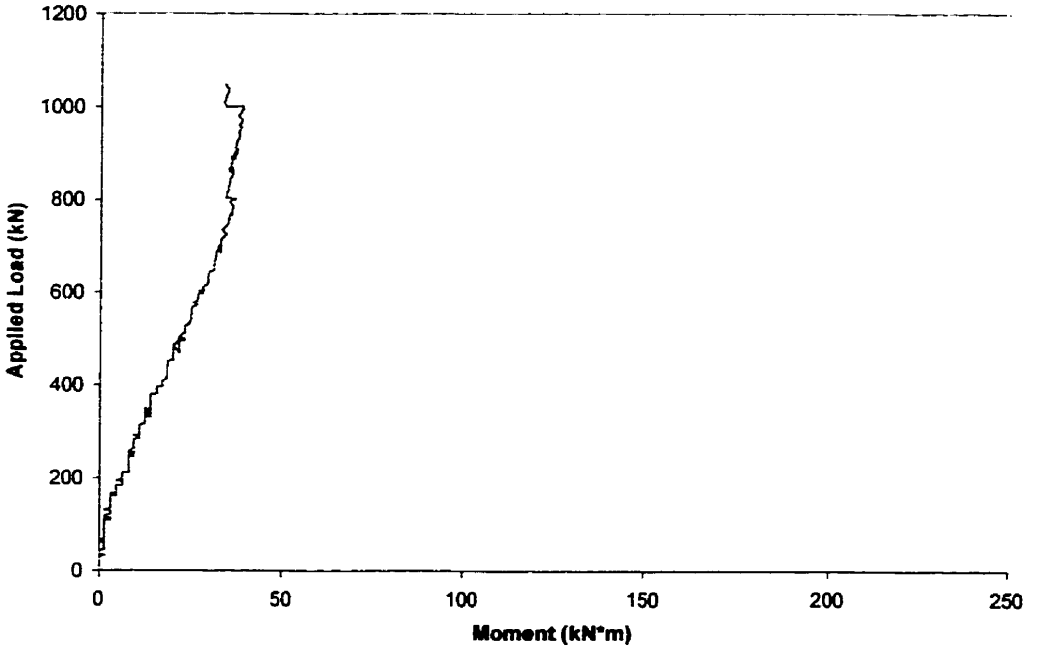

Figure 4-28: Variation of Internal Moment with Applied Load (Girder Face)

4.5 TEST 3 (LEFT CANTILEVER)

Figure 4-29 shows a section of the cantilever taken at the midspan of the girder. This section shows schematically that the total deflection of the cantilever consists of three components: girder deflection, deflection due to girder rotation, and cantilever deflection. Experimental results show that girder rotation contributes significantly to the total deflection. This can be seen in the load–deflection curve shown in Figure 4-30. Note that Test 1 is not referred to in this discussion because deflection due to slip played a key role in the behaviour of the right cantilever; therefore the right cantilever did not exhibit the expected behaviour that is discussed here. Since the behaviour of the cantilever is the focus of this study, only cantilever deflections will be discussed in relation to the serviceability requirements. The load–deflection relationship for the cantilever is shown in Figure 4-31. The deflection at service load (72.5 kN) was very small; therefore it was not recorded by the instrumentation. The CSA Code specifies a maximum deflection for a cantilever of *l*/180 under service loading conditions, which translates to 4.4 mm for the given length of cantilever. The serviceability of the cantilever is therefore satisfactory in terms of short-term deflection under service load.

The first crack was observed at a load of 230 kN during the first cycle. This flexural crack formed in the adjacent span due to the negative bending moment at the top fibres of the slab. The stiffness of the cantilever did not noticeably decrease until a level of 330 kN, when circumferential cracks were first observed. After completion

of the cyclic loading, the cantilever was loaded to a level of 875 kN. As further stroke was applied, the load decreased to approximately 650 kN due to softening of the concrete. At this point, the slab was unloaded to 100 kN in order to remove instrumentation that was at risk of being damaged. Upon being reloaded, the cantilever failed at 635 kN due to punching shear.

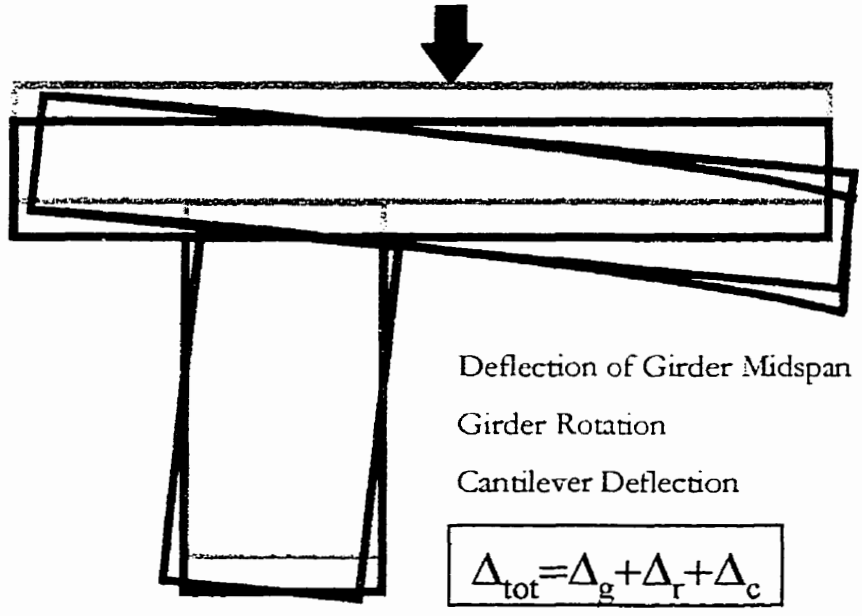

Figure 4-29: Components of Cantilever Deflection

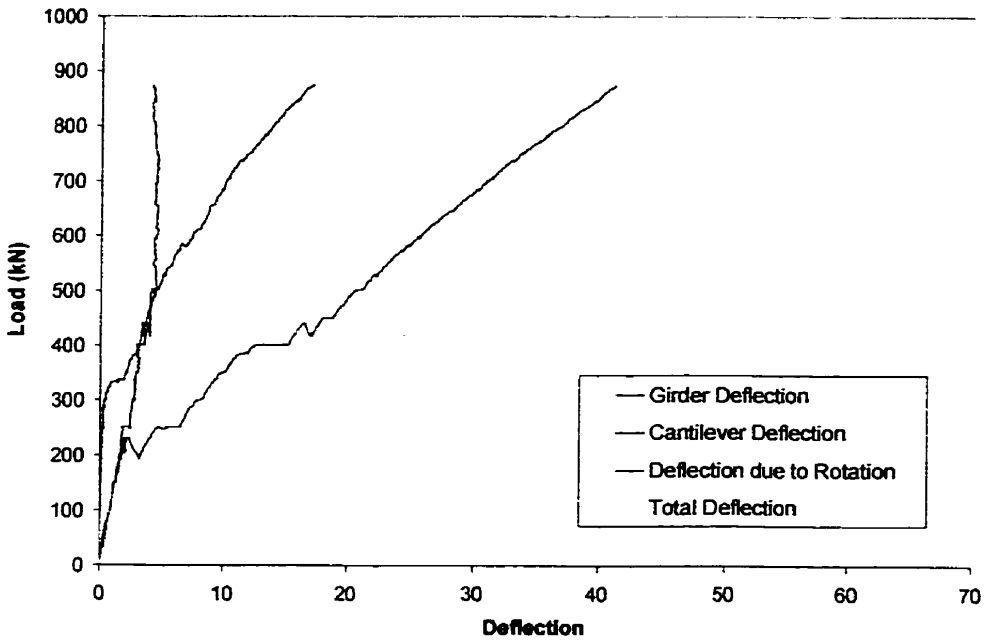

Figure 4-30: Contribution of Each Component to Total Deflection

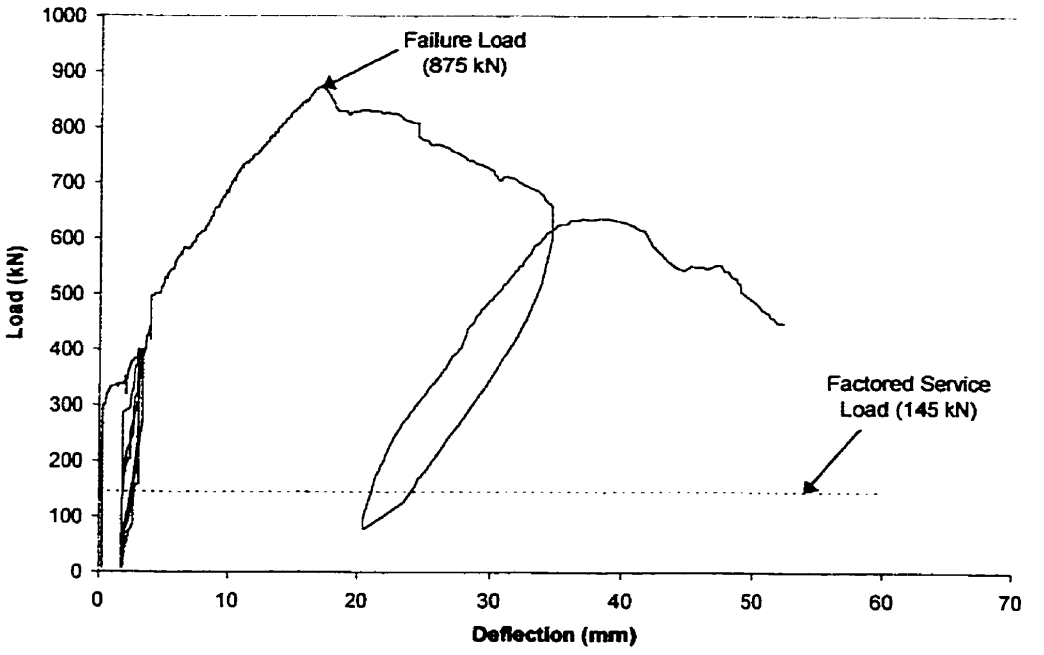

Figure 4-31: Load–Deflection Curve for Cantilever

The crack pattern at failure is shown in Figure 4-32. The first crack was observed at 230 kN due to the negative bending moment in the adjacent span. Circumferential cracks around the applied load started to develop at a load of 330 kN. The cantilever failed in shear, producing cracks on the vertical face at angles of 40° and 60° from the horizontal, as shown in Figure 4-33.

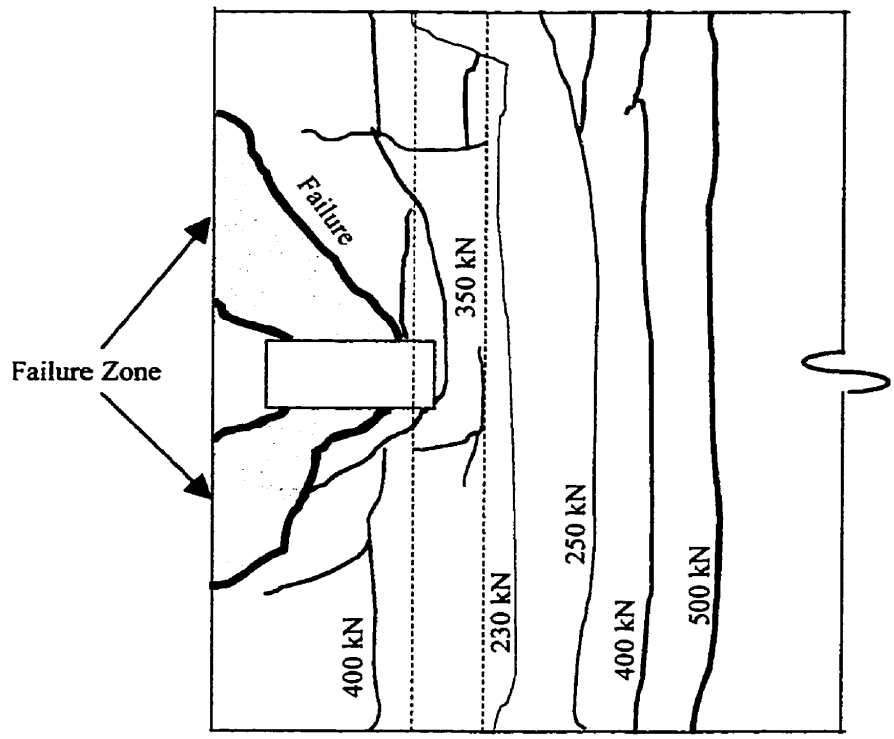

Figure 4-32: Left Cantilever Crack Pattern at Failure

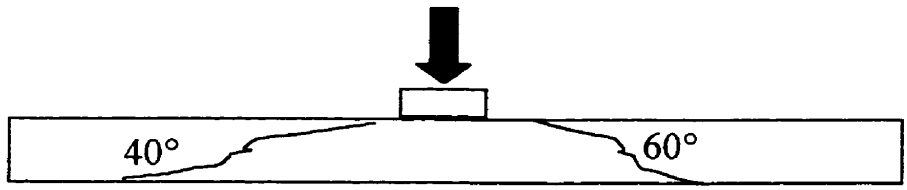

Figure 4-33: Shear Cracks on Vertical Face of Cantilever

The rotation of the girder midspan as a function of applied load is shown in Figure 4-34. The first crack occurred at the top fibres of the beam in the adjacent span due to the negative bending moment. As a result, a significant increase in girder rotation was observed, rather than deflection of the cantilever relative to the girder. It is for this reason that the load–deflection curve does not show the initiation of the first crack. Increases in rotation were observed at 250 and 400 kN, due to an increase in flexural crack width during the cycles of the applied load.

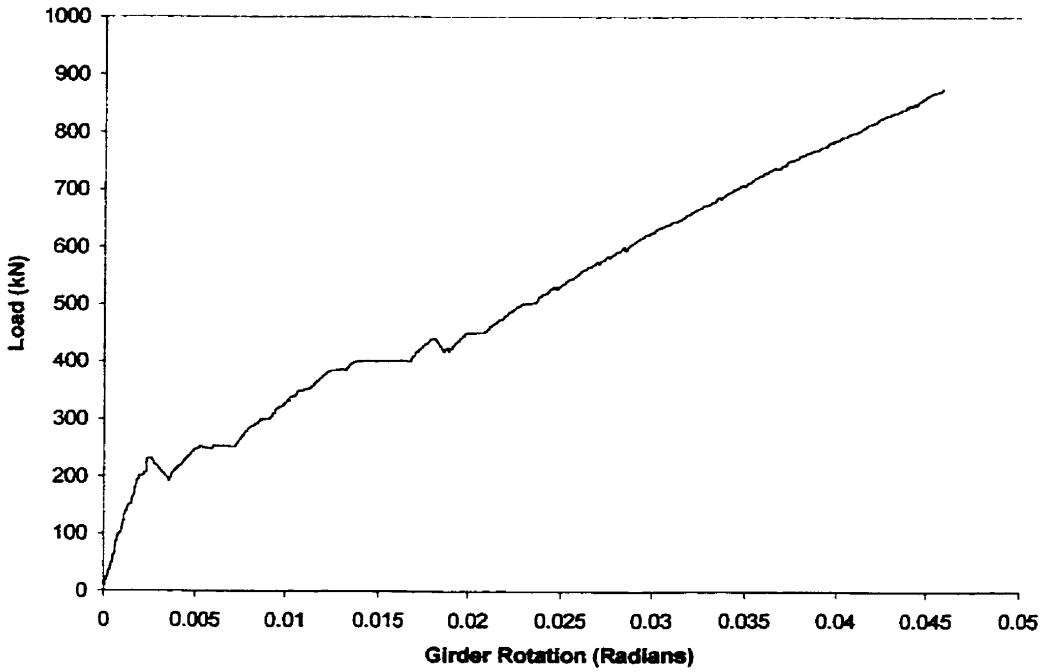

Figure 4-34: Rotation of the Girder at Midspan

Using electrical strain gauges, the measured tensile strain in the ISOROD bars reached a value of 0.012 at the maximum load of 875 kN. As load decreased due to concrete softening, the tensile strain increased to 0.016 before failure. The load–

maximum strain relationship is shown in Figure 4-35. Experimental results give a limiting tensile strain value for ISOROD of 0.017, indicating that the top reinforcement in the cantilever might have been close to rupture when the cantilever failed in shear.

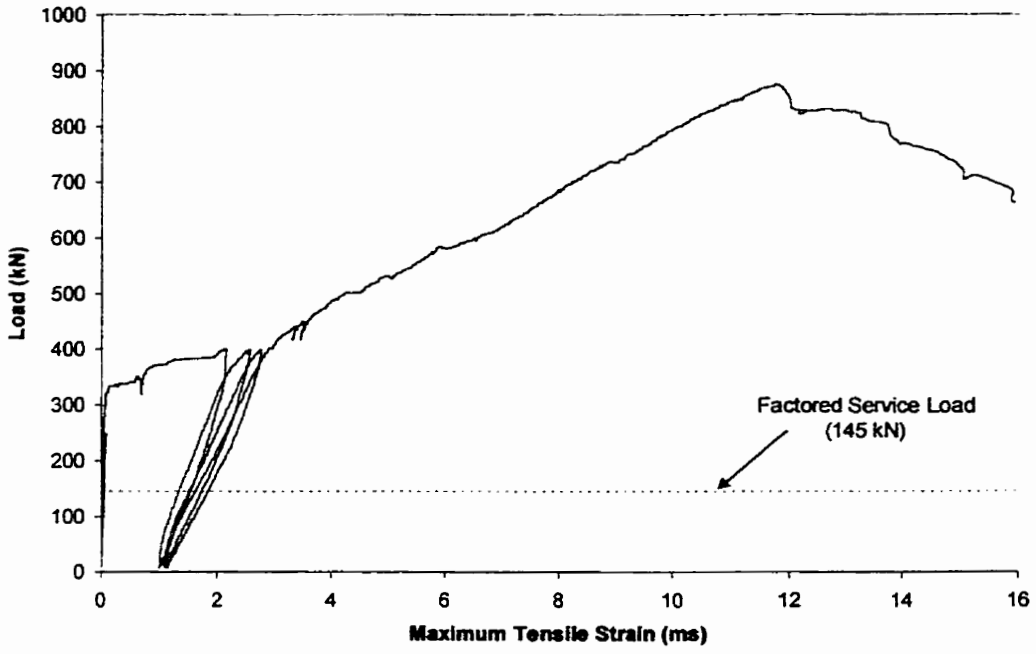

Figure 4-35: Load–Strain Relationship for GFRP at the Load Location

The strains in the top and bottom reinforcement at the midspan are shown in Figure 4-36. The top reinforcement experienced tension throughout the loading range. The bottom reinforcement experienced compression until the section cracked at 330 kN. It is important to note here that while the cracking load was 230 kN, the section where the strain gauges were located did not crack until 330 kN. Based on the

measured values in the top and bottom reinforcement, the neutral axis depth was calculated. Due to the low elastic modulus of the FRP, the neutral axis fell below the bottom reinforcement (Figure 4-37), which, as a result, became subject to tensile strains. This continued until softening of the concrete began at the maximum load. At this point, the strain in the concrete increased rapidly, causing movement of the neutral axis to a level above the reinforcement at failure. The concrete strains at the extreme compression fibre were calculated based on the strain gauge measurements in the reinforcement. As shown in Figure 4-38, these measurements indicate that the concrete began to soften at a strain of 0.002. The PI gauges that were mounted to the bottom of the cantilever and attached to the face of the supporting beam could not be used to measure the compressive strain in the concrete at the face of the beam. This is because the PI gauges measured a combination of concrete compressive strain and rotation of the cantilever with respect to the beam. This occurred after local crushing of the concrete took place. For this reason, measurements from the PI gauges were far in excess of the actual strains present in the concrete. Figure 4-39 shows a schematic of the phenomenon described here.

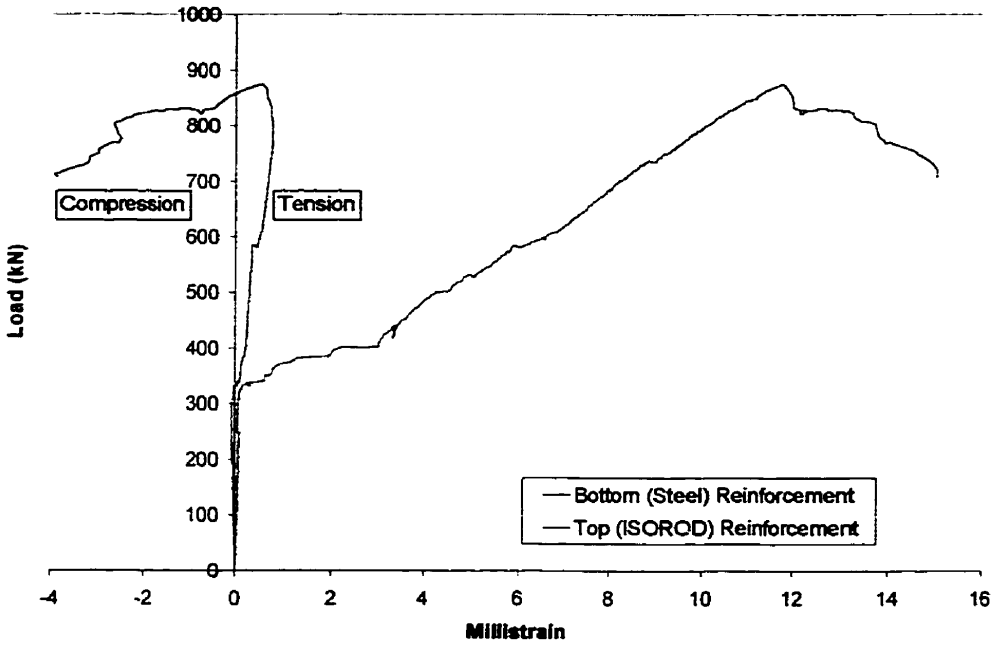

Figure 4-36: Strains in Top and Bottom Reinforcement at the Load Location

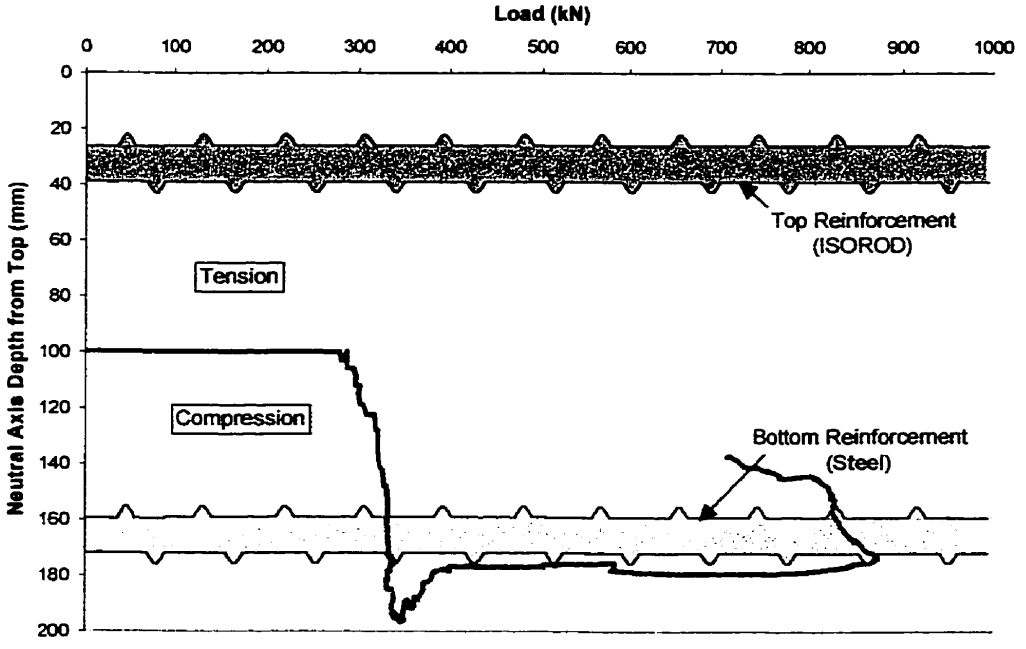

Figure 4-37: Load vs. Neutral Axis Depth

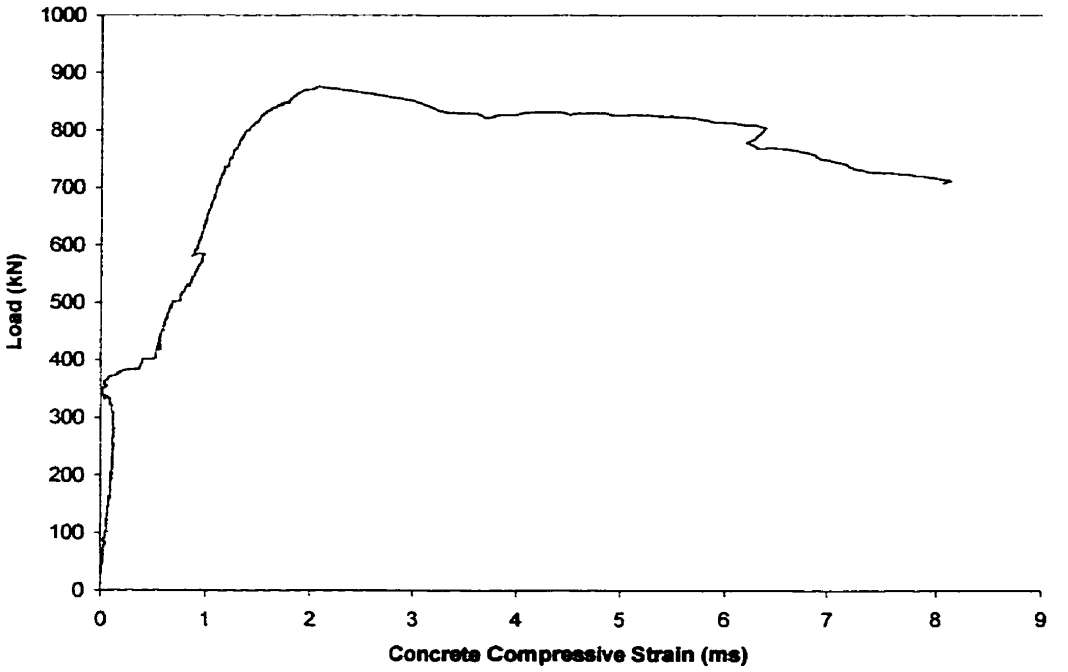

Figure 4-38: Strain in Concrete at the Load Location

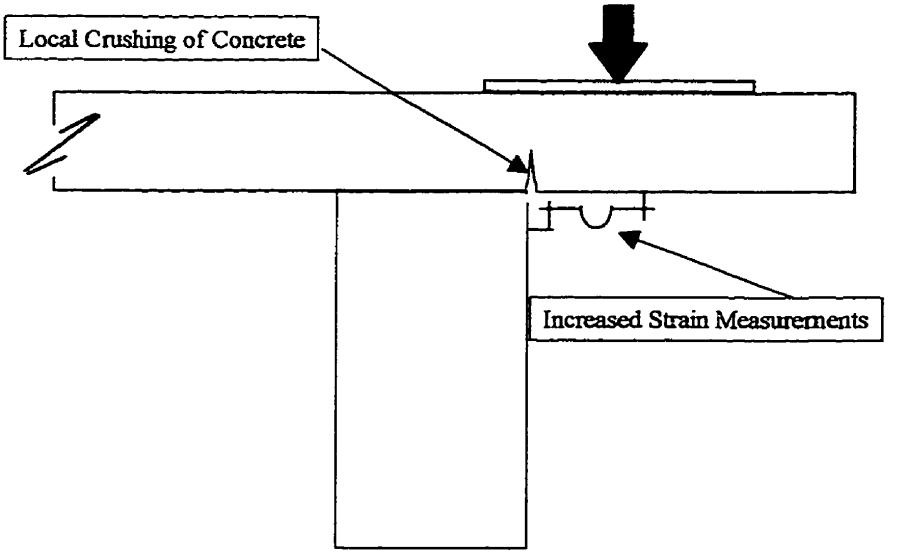

Figure 4-39: Local Crushing of Concrete causing Increased Measurements

The distribution of strain in the top reinforcement is shown in Figure 4-40. The strains were very low until the section cracked at 330 kN. A plateau in the distribution formed and became more apparent as the load increased. The width of the plateau was approximately 1200 mm.

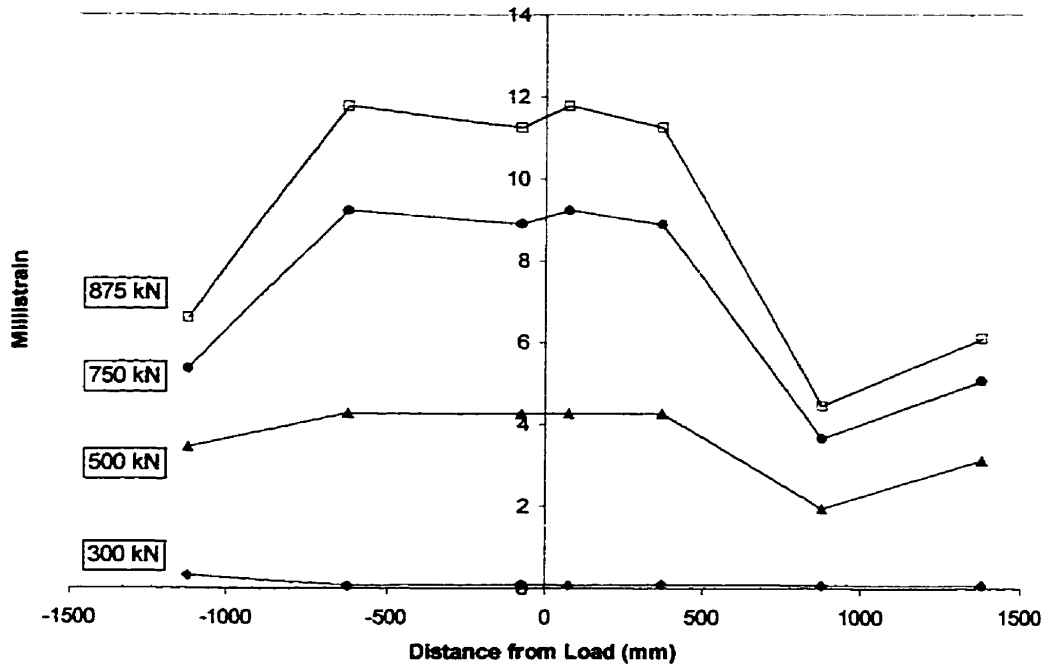

Figure 4-40: FRP Strain Distribution

Using conventional reinforcement, the steel in typical cantilever members yields, causing redistribution of the load away from the point of application. For FRP reinforcement, due to its brittle failure characteristics, the strain would increase without redistribution up to rupture of the reinforcement, causing failure. The strain

plateau may be explained by showing the distribution of forces within the cantilever. Figure 4-41 shows that the forces are distributed through an angle θ to the face of the girder.

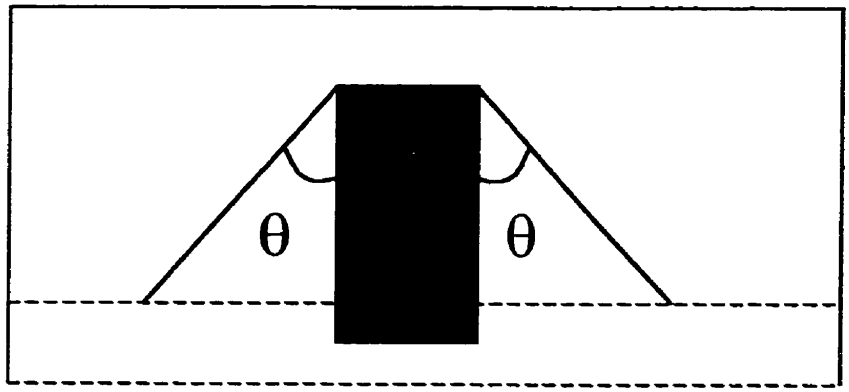

Figure 4-41: Distribution of Load in Cantilever

Using assumed load distribution angles of 45°, 55°, and 60°, and a fixed value for ε_c' of 0.00215, the strains and stresses in the section were calculated according to the method described in Section 4.4. Values for the concrete strain (ε_c) were chosen initially. Once the parameters α_1 and β_1 were found, the depth of the compression zone, c, was assumed. The compressive and tensile forces were then summed, and the value for c was adjusted until equilibrium was achieved. Using the equilibrium value for C and T, the moment in the section and the corresponding strain in the FRP were calculated. This process was repeated for various values of ε_c, from

cracking moment to failure of the section due to the limiting concrete strain value of 0.0035.

When plotted as a function of the applied moment, the predicted values for strain in the FRP can be compared to the measured values for tests 1 and 3, as shown in Figure 4-42. The measured test data compare fairly well with the load distribution angle of 45°. The matching slope values result in a prediction that gives accurate stiffness predictions and conservative strain estimates for both tests.

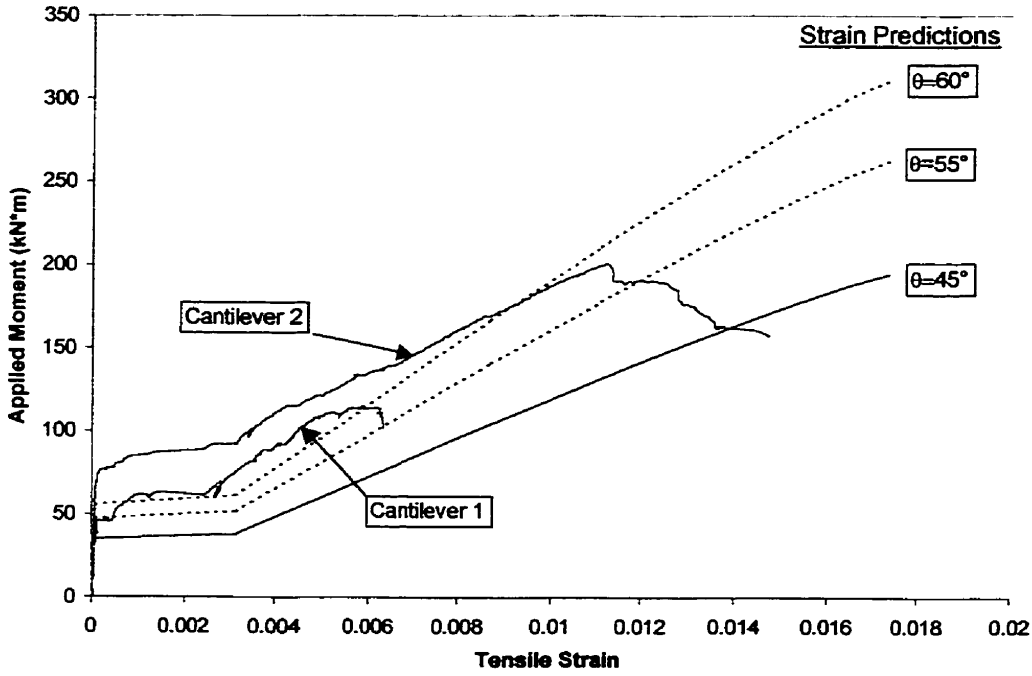

Figure 4-42: Predicted versus Actual Behaviour

4.6 TESTS 4 AND 5 (LEFT AND RIGHT SPANS)

The load–deflection relationships for tests 2, 4 and 5 are shown in Figure 4-43. Note that test 2 results are included in this section for the purpose of comparison. The total deflection was measured at the bottom of the slab under the location of the applied load. The deflection of the girder in the line of the applied load was also measured, in order that the deflection of the slab relative to the girder could be determined. The deflections at service load were 0.15, 0.7, and 0.3 mm for tests 2, 4 and 5 respectively. The higher deflections for tests 4 and 5 are a result of the pre-existing cracking at the top surface of the slabs following complete testing of the cantilevers. The presence of these cracks decreased the stiffness of the slabs, resulting in higher deflections and rotations of the girders. The measured failure loads in punching shear were 1050 kN, 1090 kN, and 1180 kN for tests 2, 4, and 5 respectively.

The deflection profiles along the midspan of the slab parallel to the supporting beams for tests 4 and 5 are shown in Figure 4-44 and Figure 4-45 respectively. The small deflections measured at the ends of the slab show that the load was distributed in two directions. The ends of the slab perpendicular to the girders acted as supports for the distribution of load in the transverse direction. The deflections in test 4 are considerably higher than those in test 5. This was expected, since the left span was

more severely damaged by the left cantilever test than was the right span by the right cantilever test.

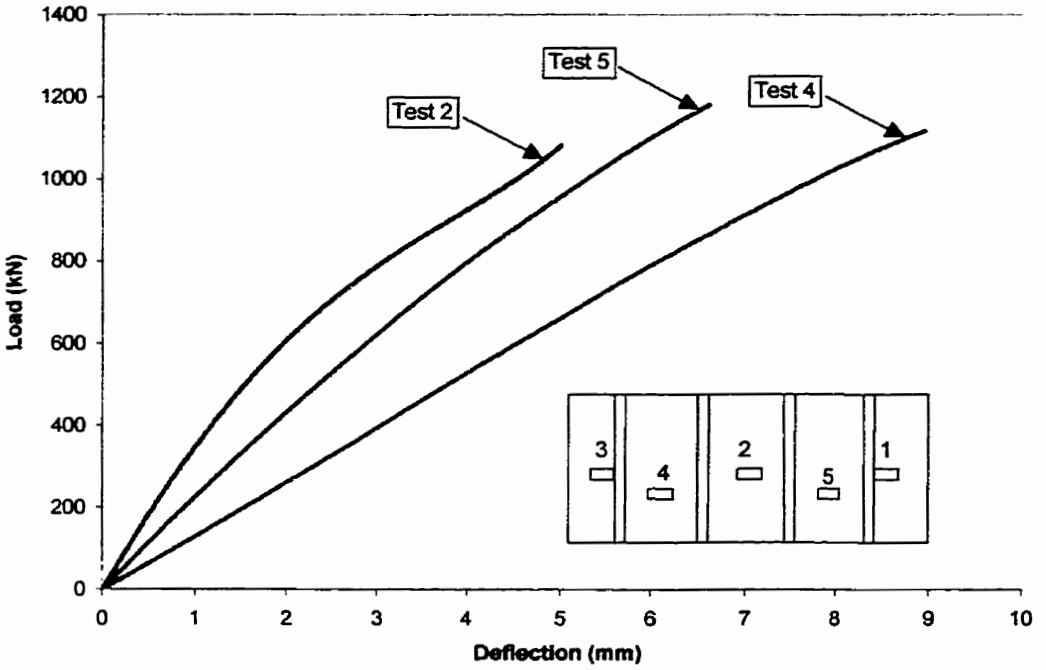

Figure 4-43: Load–Deflection Relationships for the Three Interior Spans

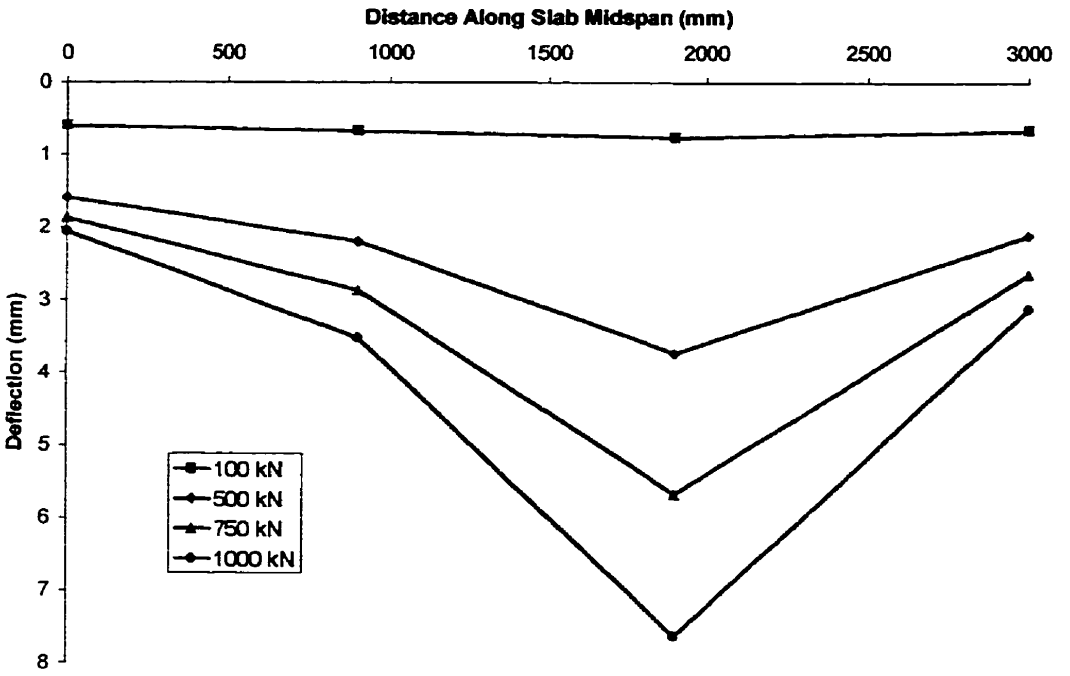

Figure 4-44: Midspan Deflection Profile for Test 4

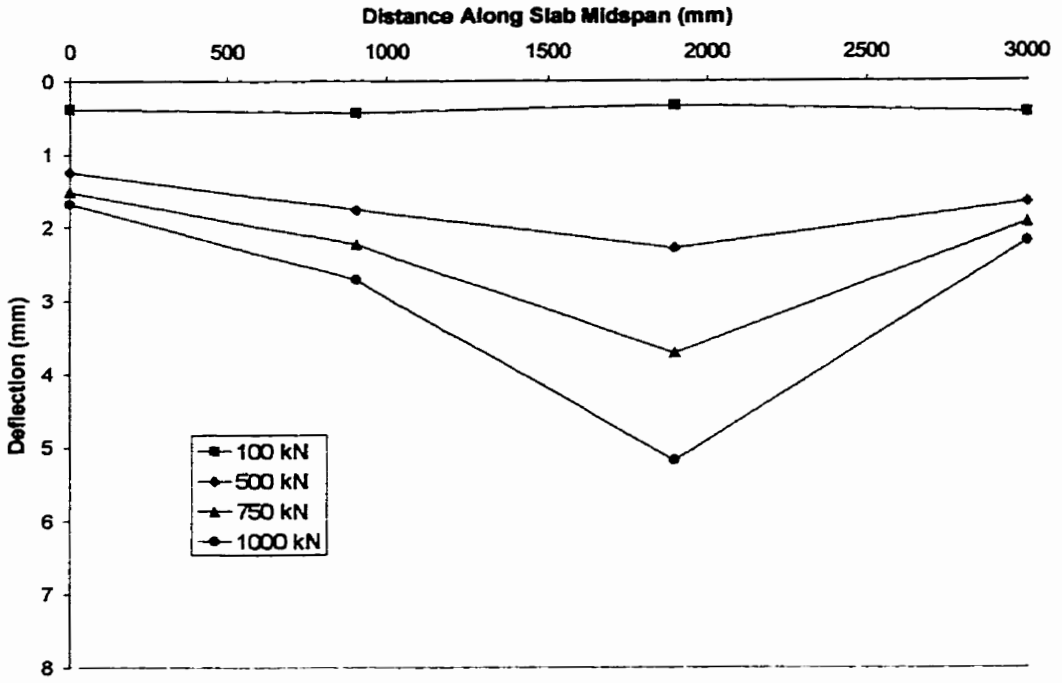

Figure 4-45: Midspan Deflection Profile for Test 5

The crack pattern of the bottom surface of left span (Test 4) at failure is shown in Figure 4-46. The cracking load was 80 kN, with a flexural crack forming at midspan, parallel to the supporting beams. At a load level of 300 kN, radial cracks extended from the load location to the outer edges of the slab. A major crack was formed at failure (1090 kN) by punching shear to the right of the load location as shown in Figure 4-46.

The crack pattern at failure for the right span (Test 5) is shown in Figure 4-47. Similarly to the left span, the first crack occurred at 80 kN, with a flexural crack forming along the slab midspan parallel to the supporting beams, followed by the formation of the radial cracks at a load level of 300 kN. The major crack to the right

of the load location occurred at the punching shear failure load of 1180 kN, as shown in Figure 4-47.

Figure 4-46: Test 4 Crack Pattern at Failure (Bottom Surface)

Figure 4-47: Test 5 Crack Pattern at Failure (Bottom Surface)

The rotations of the supporting beams in tests 2, 4, and 5 are shown in Figure 4-48. For tests 4 and 5, the rotation of the left and right beam are shown. The beam supporting the cantilever was expected to rotate more than the beam supporting the continuous slab in each test. This type of behaviour is expected because the projected end of the cantilever is not restrained vertically, whereas the adjacent interior span is restrained. The expected behaviour did take place, as can be seen in Figure 4-48. Figure 4-49 shows average rotations of the two beams for each test. Behaviour of the beams for test 2 showed an approximately linear load–rotation relationship until failure. The supporting girders in tests 4 and 5 show a high rate of

rotation at lower loads, with a decreasing rate as the load increased. This behaviour was likely related to the holes in the steel strap that were used to restrain the girder rotation, as shown in Figure 4-50. As a result, the girders rotated initially before closing the gap between the pin and the holes, as evidenced by the measured strain of the strap, as shown in Figure 4-51. In this figure, the straps were not stressed until a load level of approximately 150 kN in test 5, and 400 kN in test 2. Since the test 2 data show initial straining followed by a vertical portion, it is likely that the strap in test 2 was initially in compression. Rate reduction of the rotation could also be attributed to the fact that testing of the two cantilevers cracked the top surface of the adjacent spans, as shown in Figure 4-52. While conducting tests 4 and 5, it was found that closing of the cracks from the previous tests was necessary before the slab was to achieve its full stiffness. Figure 4-53 shows that at a load level between 200 and 300 kN, the cracks close and the stiffness of the slab increases. This corresponds to Figure 4-48, showing that above 200 kN the rate of increase of girder rotation is reduced. It was found that both curves approximate a bilinear relationship between the measured strain and the applied load. The first line in each curve represents the closing of the cracks at the top surface due to the compressive strain induced at the top fibre of the slab. If the beginning of the second line is taken as the point of zero strain at the top surface of the concrete, it can be seen that the concrete in both tests achieved a strain of slightly over 0.003, which is the average value of the ultimate strain for concrete in compression.

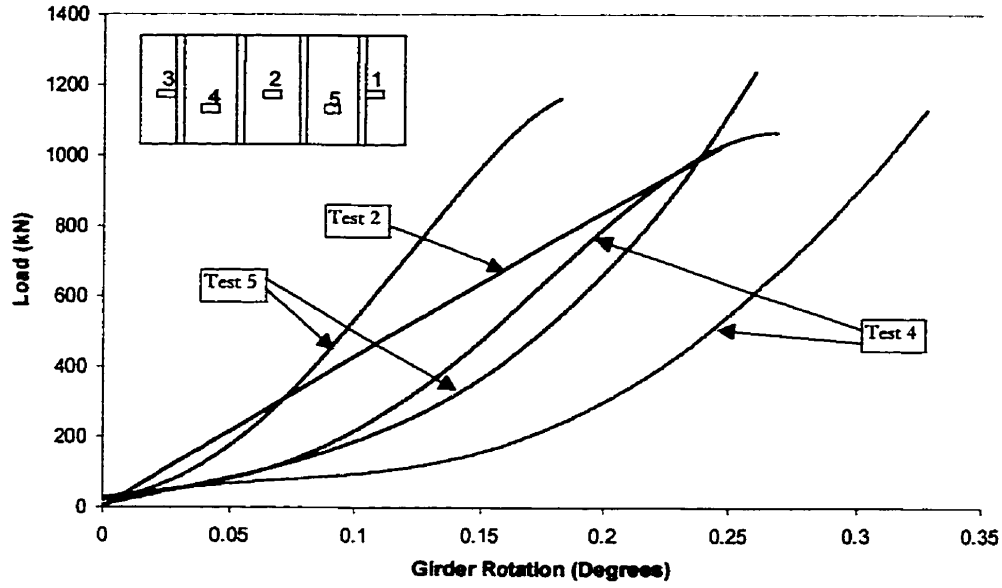

Figure 4-48: Rotation of All Supporting Girders for Tests 2, 4, and 5

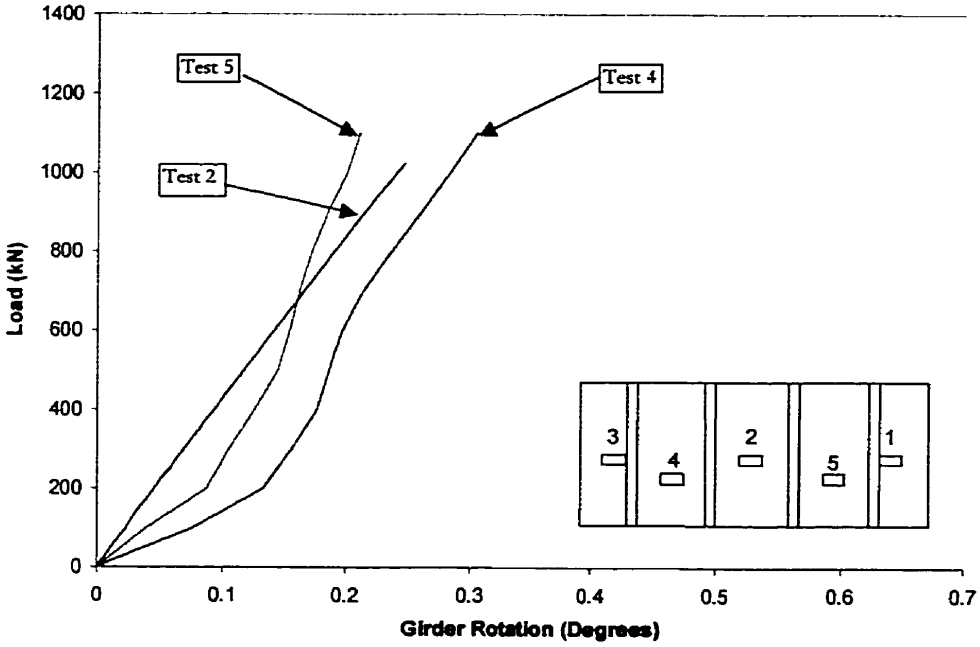

Figure 4-49: Girder Rotations with Average Values for Tests 4 and 5

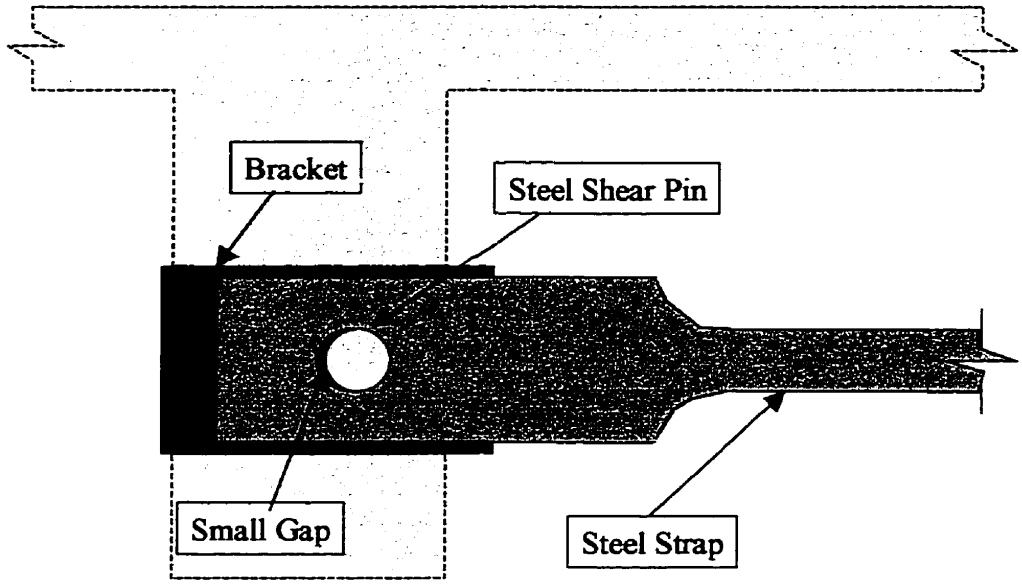

Figure 4-50: Schematic of Steel Restraining Strap

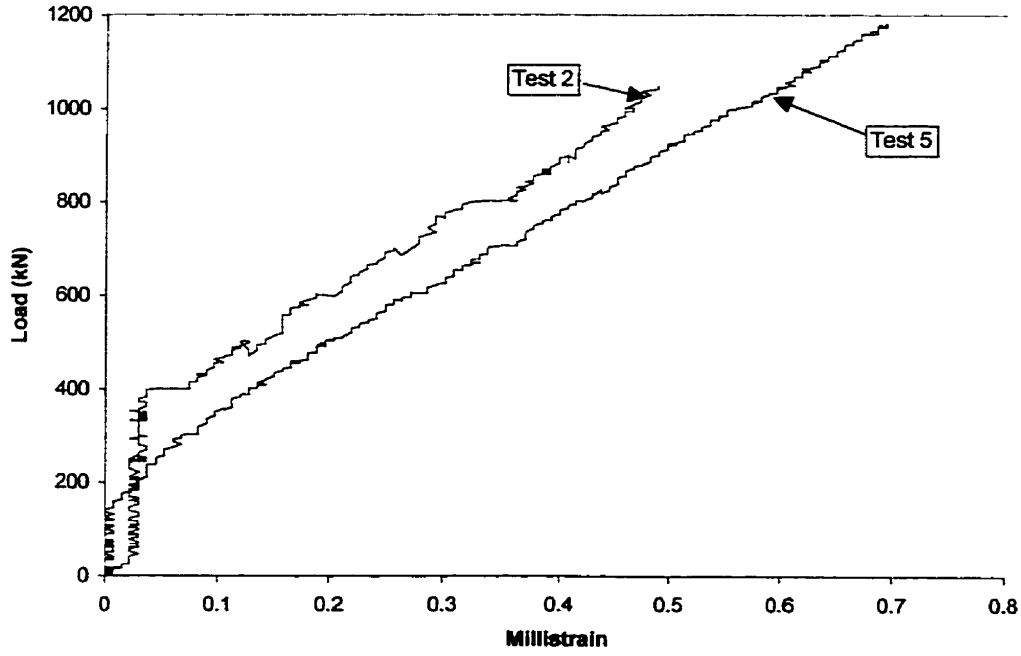

Figure 4-51: Measured Strain in Steel Restraining Straps, Tests 2 and 5

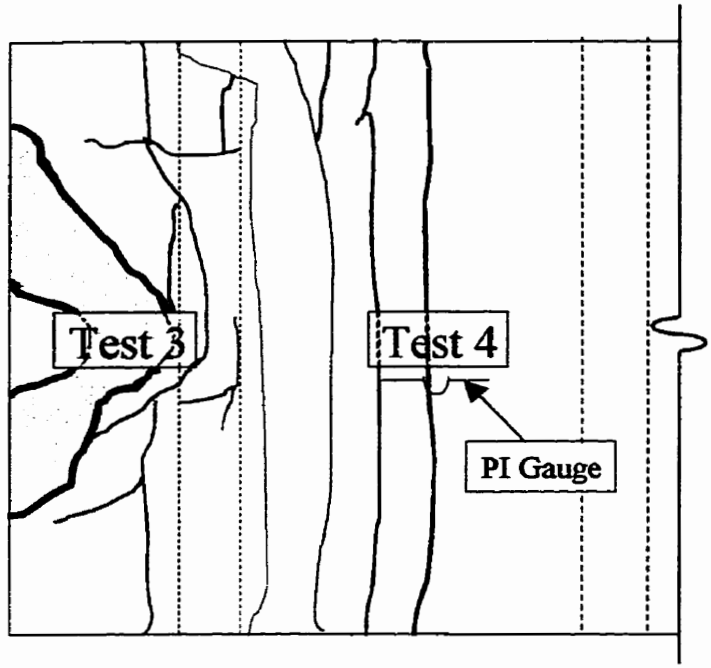

Figure 4-52: Cracks Formed during Test 3

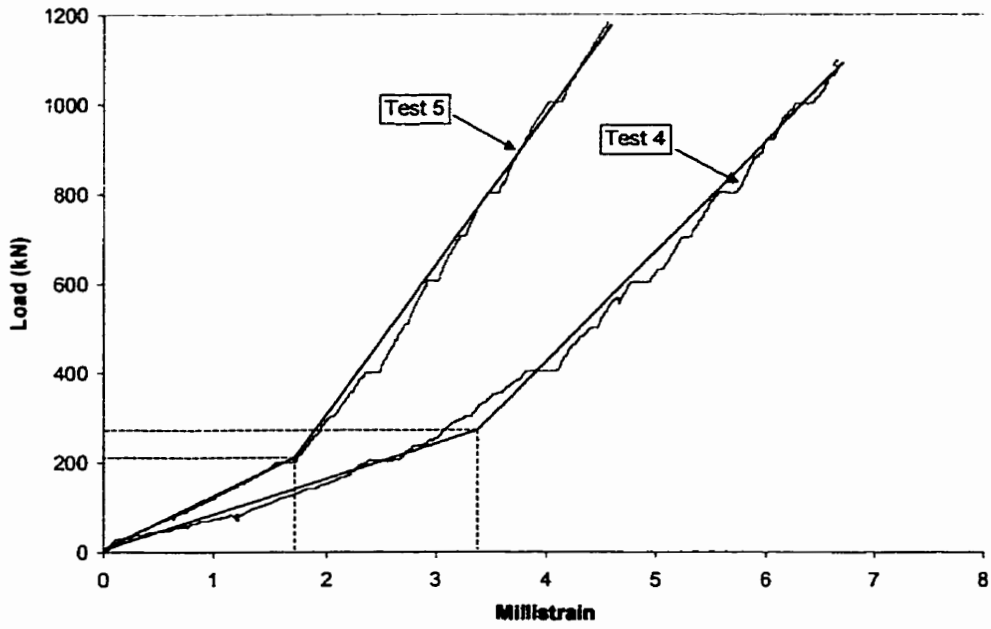

Figure 4-53: Measured Strains at Top Surface of Slab at the Load Location

CHAPTER 5: COMPARISON WITH ANALYTICAL MODEL

5.1 INTRODUCTION

As discussed in Chapter 2, ANACAP is a non-linear finite element program designed specifically for modelling of concrete and steel structures. An analytical model was developed using ANACAP by T. Hassan in parallel with the construction and testing of the experimental model. The purpose of the analytical model is to facilitate parametric studies. With this model, any characteristic of the deck slab can be varied in order to investigate the resulting effects on behaviour. Conducting such parametric studies through construction and testing of experimental models is expensive and time-consuming. This chapter presents a description of the analytical model that was developed, and the analytical results are presented and compared with the experimental results.

5.2 THE ANALYTICAL MODEL

Two analytical models were developed to represent the experimental model. One model was designed to simulate the response of the cantilevers of the experimental model, while another was developed to represent the interior middle span. The elements that made up the two models were 20-node hexahedral elements, as shown in Figure 5-1.

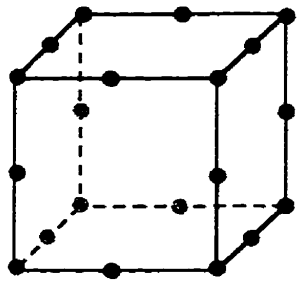

Figure 5-1: 20-Node Hexahedral Element

5.2.1 The Cantilever Model

The finite element mesh for the analytical cantilever model is shown in Figure 5-2. With the use of symmetry about the line passing through the centre of the applied load, this mesh represents one cantilever and an adjacent span. Including the middle span in this model would have resulted in unnecessary complexity of the model. In addition, the left girder in Figure 5-2 was physically restrained from lifting in both the experimental model and the analytical model. The presence of the middle span, therefore, would not have affected the behaviour of the analytical model.

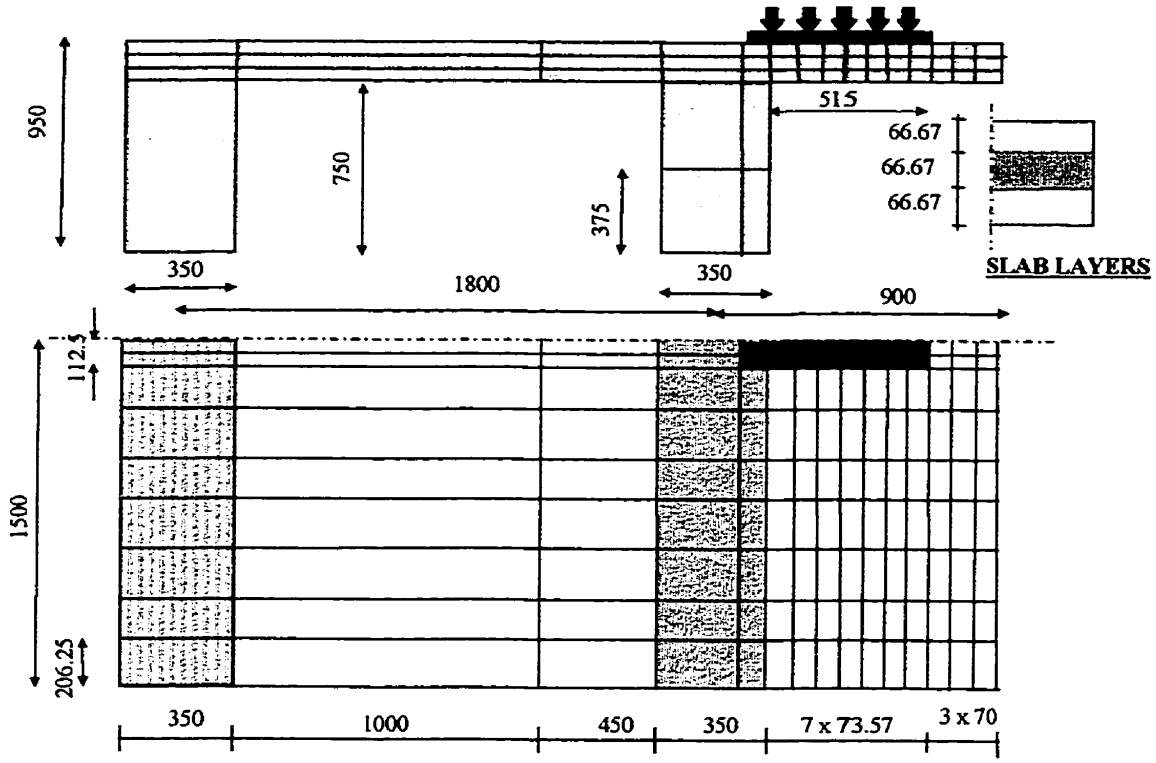

Figure 5-2: Finite Element Mesh used for Cantilever Model (Hassan, 1999)

5.2.2 The Interior Span Model

The mesh that was developed for the interior span model is shown in Figure 5-3. This mesh represents one-quarter of the entire experimental model without the cantilevers. Symmetry about both lines that intersect at point P_1 was used to complete the model.

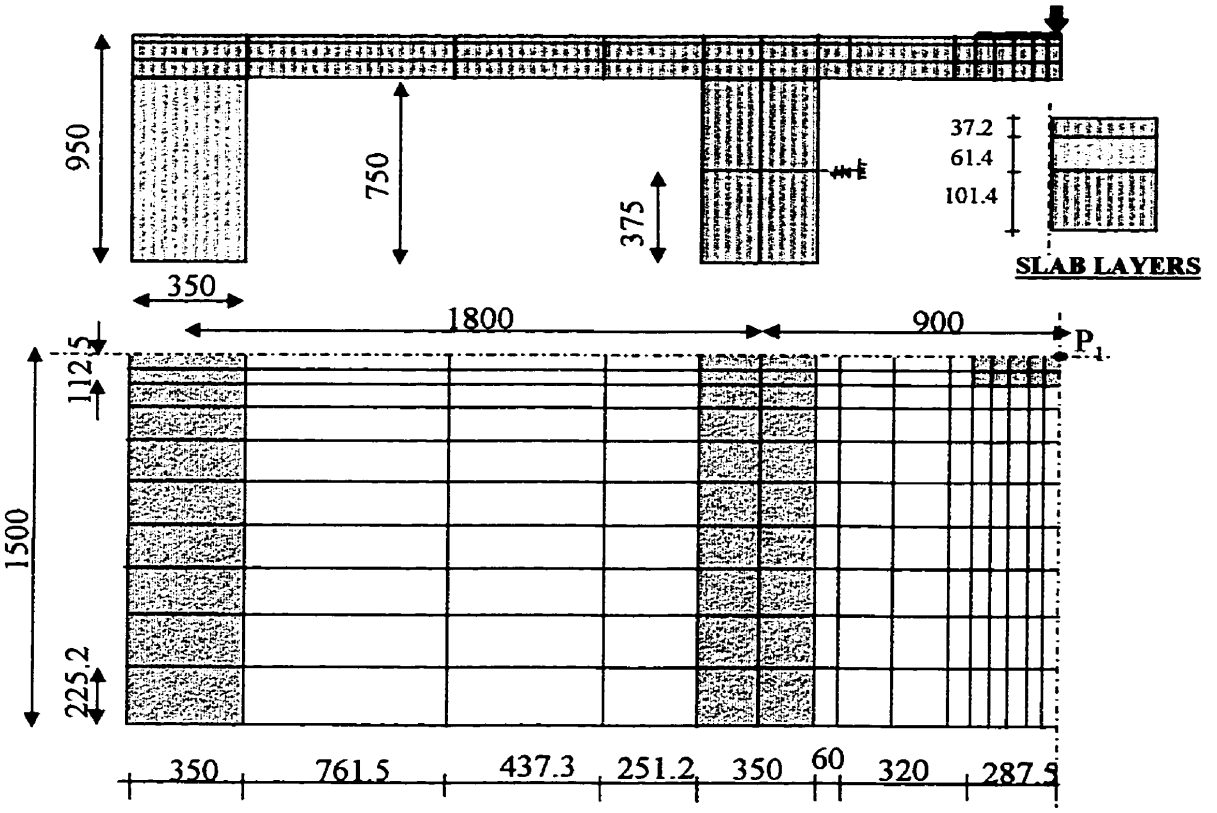

Figure 5-3: Finite Element Mesh used for Interior Span (Hassan, 1999)

5.3 ANALYTICAL RESULTS AND COMPARISON

This section presents a comparison of behaviour between the experimental model and the analytical model. Failure loads, load–deflection behaviour, and load–strain behaviour are compared for the cantilevers and the interior spans.

5.3.1 The Cantilevers

The analytical model was developed to represent both cantilevers in the experimental model. For the right cantilever of the experimental model, the maximum load was 500 kN due to slip of the top reinforcement (C-BAR), as discussed in Chapter 4. The analytical failure, however, occurred due to punching shear at a value of 856.6 kN. Although the manufacturer's information states that ANACAP is capable of modelling bond characteristics, the bond strength of the reinforcement cannot be quantitatively specified in the input file. Instead, ANACAP requires the user to specify qualitative parameters for the bond characteristics of the reinforcement such as "good" or "poor." For the analytical model of the right cantilever, the bond strength was specified as poor, but the cantilever still failed due to punching shear rather than bond failure. ANACAP is therefore inadequate in terms of identifying the bond failure that was observed in the experimental model.

For the left cantilever, the finite element analysis terminated at a load value of 984 kN. The corresponding concrete compressive strain at the loaded area was

$20x10^{-3}$. From the load–compressive strain relationship it was observed that at a load level of 921 kN, a drastic change in the cantilever behaviour occurs, with a considerable increase in the compressive strain while a slight increase in applied load takes place. 921 kN was therefore taken as the failure load due to crushing of the concrete, leading to punching. The corresponding value of the compressive strain at failure was $4x10^{-3}$. The experimental failure load value was 875 kN, which is 5.3 % lower than the predicted failure load obtained by the finite element analysis.

For the left cantilever, the net load–deflection behaviour was calculated at the cantilever end by subtracting the girder's deflection as well as the deflection due to the girder's rotation from the total deflection. The analytical results are shown in comparison with experimental values for the left cantilever in Figure 5-4. The analytical results correlate well with the experimental results until a load level of 500 kN was reached. Higher values of the experimental deflection were observed between 500 kN and failure. Such behaviour may be attributed to the localised crushing of the concrete at the girder face that was observed in the experimental model. This crushing decreased the effective depth of the slab and resulted in higher reinforcement strains and cantilever deflections before failure.

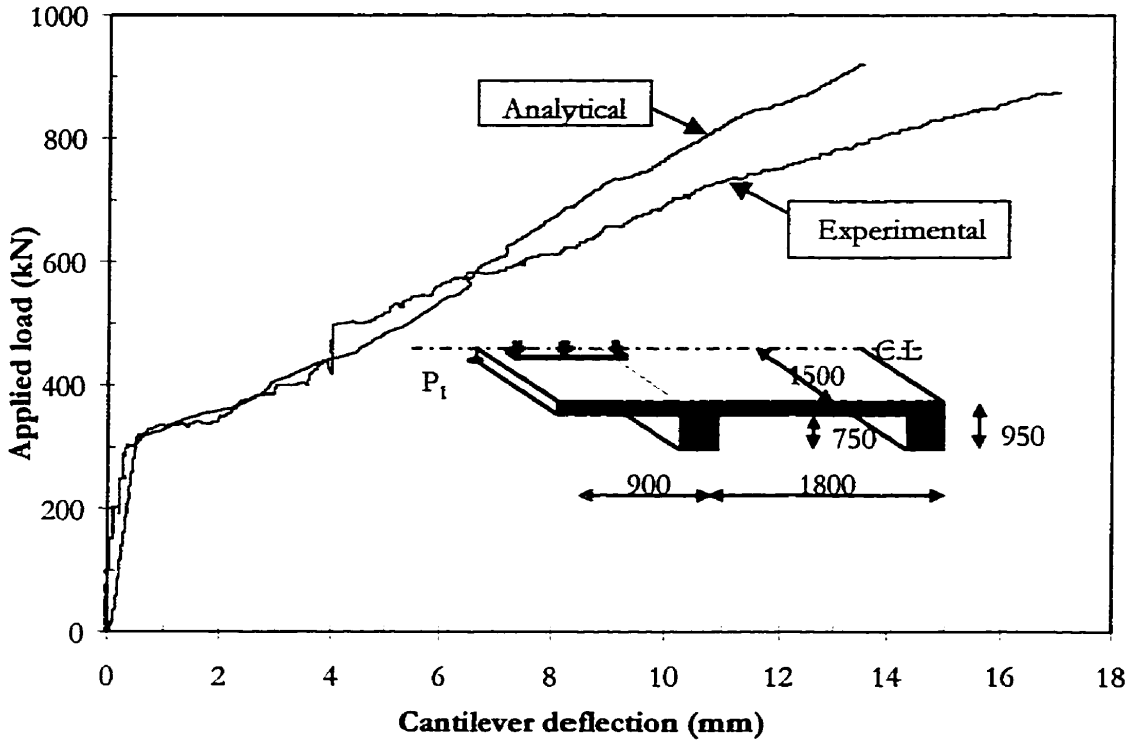

Figure 5-4: Load–Deflection Relationships for Left Cantilever

For the right cantilever, the predicted deflection values correlate well with the experimental results until a load of 500 kN was reached, beyond which the predicted deflection was much less than the measured values. This discrepancy is due to the slipping of the reinforcement that was observed in the experimental model, as discussed in Section 4.2. The comparison of load–deflection behaviour for the right cantilever is shown in Figure 5-5.

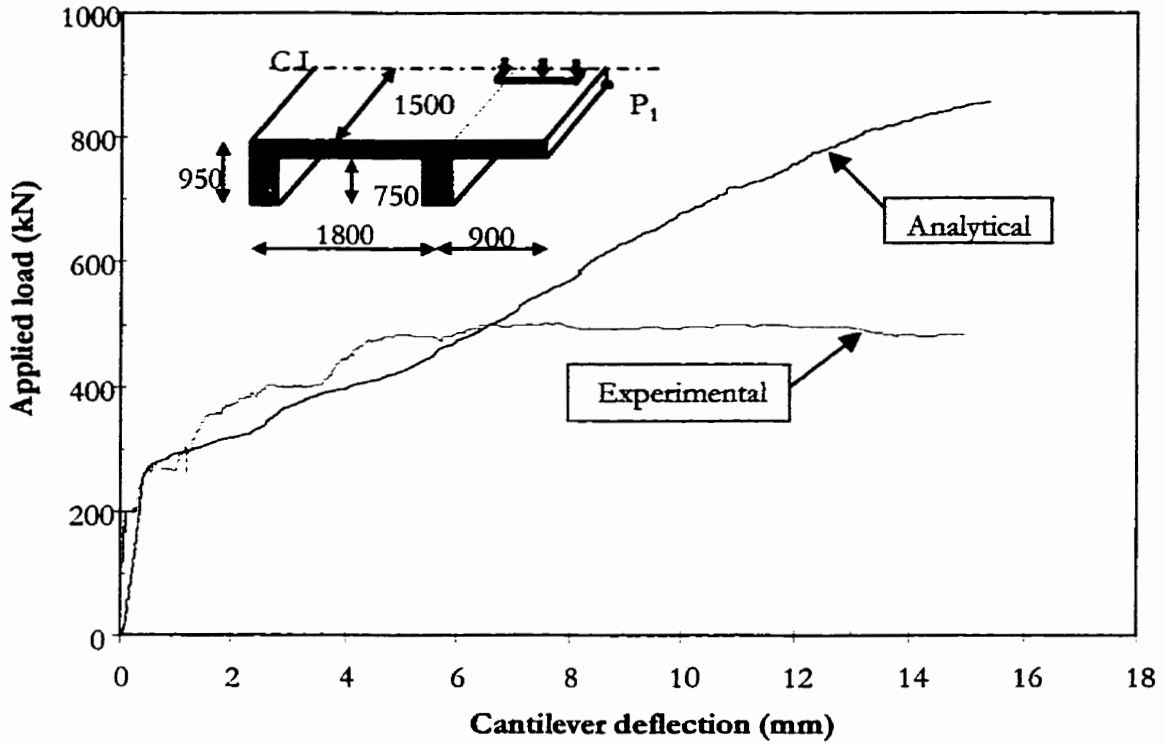

Figure 5-5: Load–Deflection Relationships for Right Cantilever

The maximum tensile strains in the top reinforcement of the analytical model were predicted for the left and right cantilevers. The results were compared to the experimental values as shown in Figure 5-6 and Figure 5-7, respectively. The maximum predicted tensile strain for the left and the right cantilevers reached a value of 0.0086 and 0.011 respectively. As observed with the load–deflection behaviour, the localised crushing in the experimental model may have caused the strains to increase in the left cantilever of the experimental model. For the right cantilever, slip of the reinforcement did not allow the strains in the experimental model to approach the predicted values.

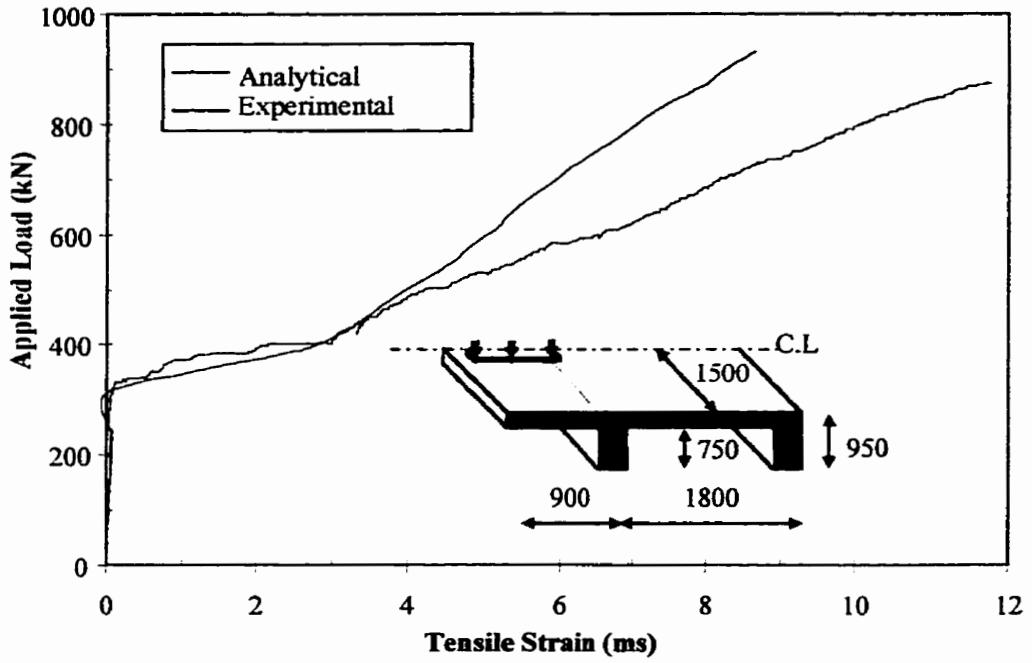

Figure 5-6: Load–Maximum Tensile Strain Relationships for Left Cantilever

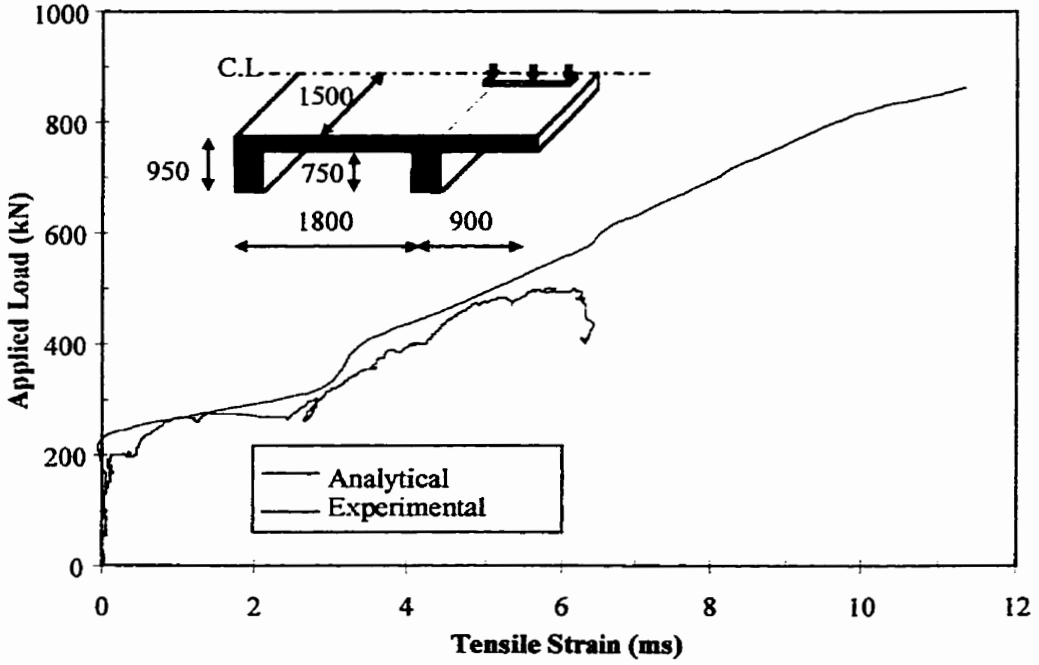

Figure 5-7: Load–Maximum Tensile Strain Relationships for Right Cantilever

5.3.2 The Interior Span

The interior span analytical model was designed to simulate the middle span of the experimental model. The other interior spans of the experimental model were not modelled because of the lack of symmetry in the location of the applied load. An analytical model for these tests would have required twice as many elements and would have greatly increased the execution time of the program. It also would have been difficult to model the pre-existing cracks, which were found to have a large effect on the behaviour of the left and right spans of the experimental model, as discussed in Chapter 4.

The load–deflection behaviour for the two models is shown in Figure 5-8. As discussed in Chapter 4, the experimental model failed due to punching shear at a load of 1050 kN. For the analytical model, punching occurred following a rapid increase in compressive strain in the concrete beginning at 980 kN. The failure load for the analytical model was then taken as 980 kN. While these failure loads are within 10% of each other, it is evident from Figure 5-8 that the behaviour of the two models is quite different.

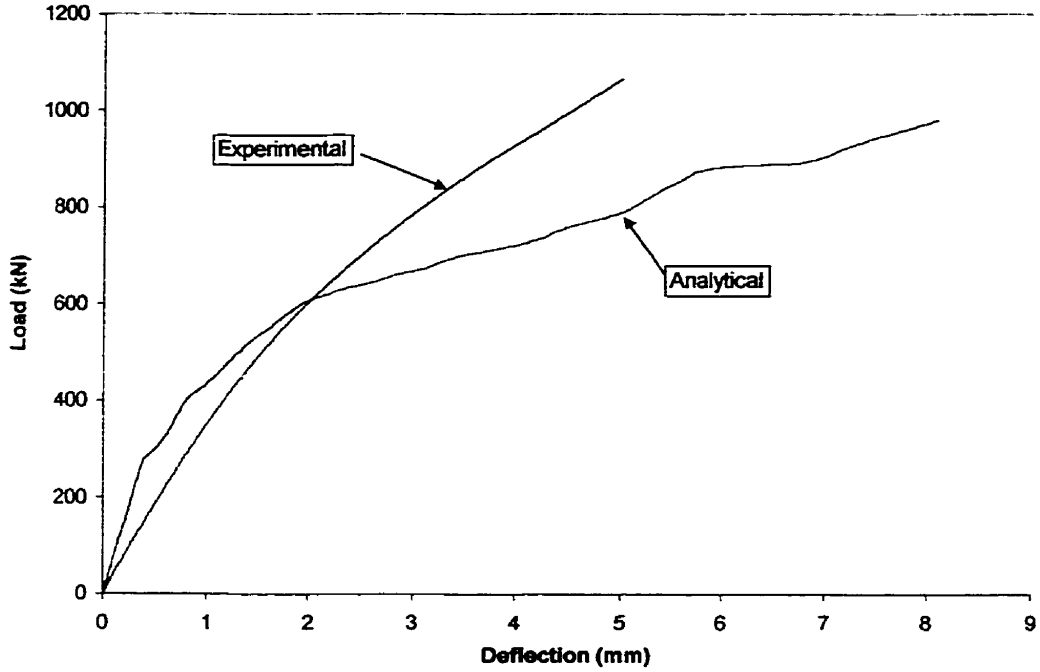

Figure 5-8: Load–Deflection Relationship Comparison

The analytical model predicted a sudden decrease in stiffness at a load level of 600 kN. This caused the predicted deflection to increase rapidly, resulting in a deflection at failure that was 50% higher than the measured value for the experimental model. The reason for the discrepancy between the two models is illustrated in Figure 5-9. This Figure shows the measured and predicted strains in the bottom reinforcement at the girder face. The bottom reinforcement in both models is subject to compression at first, followed by tension. The analytical model, however, shows that the strains changed from compressive to tensile at a load level of approximately 500 kN, resulting in cracking at the bottom surface of the slab at the girder face at a load of 600 kN. The same transition to tension at the bottom

reinforcement occurred at a load level of 1000 kN in the experimental model, and only after load cycles at that level were applied. Cracking at this location in the experimental model was not observed until failure. The difference in behaviour is further illustrated in Figure 5-10, which shows the neutral axis depth as a function of the applied load for both models. The neutral axis depth in the experimental model reached a maximum value at failure, approximately equal to the depth of the bottom reinforcement. For the analytical model, the neutral axis depth reached the bottom reinforcement at approximately 600 kN, then increased to a depth greater than the height of the slab section. Thus, the entire section at the girder face was in tension beyond a load level of 750 kN in the analytical model.

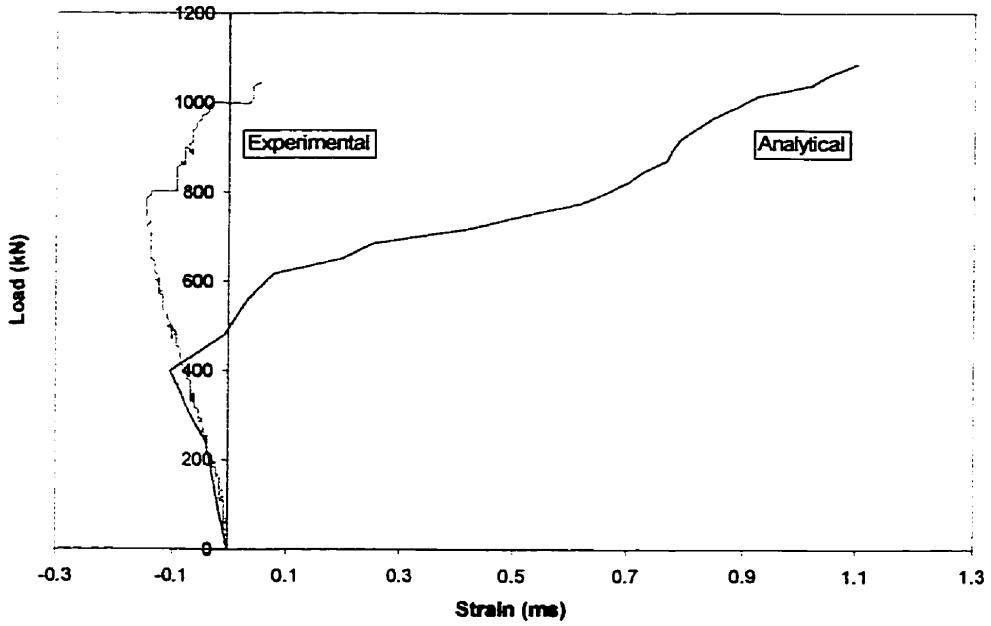

Figure 5-9: Bottom Reinforcement Strains at the Girder Face

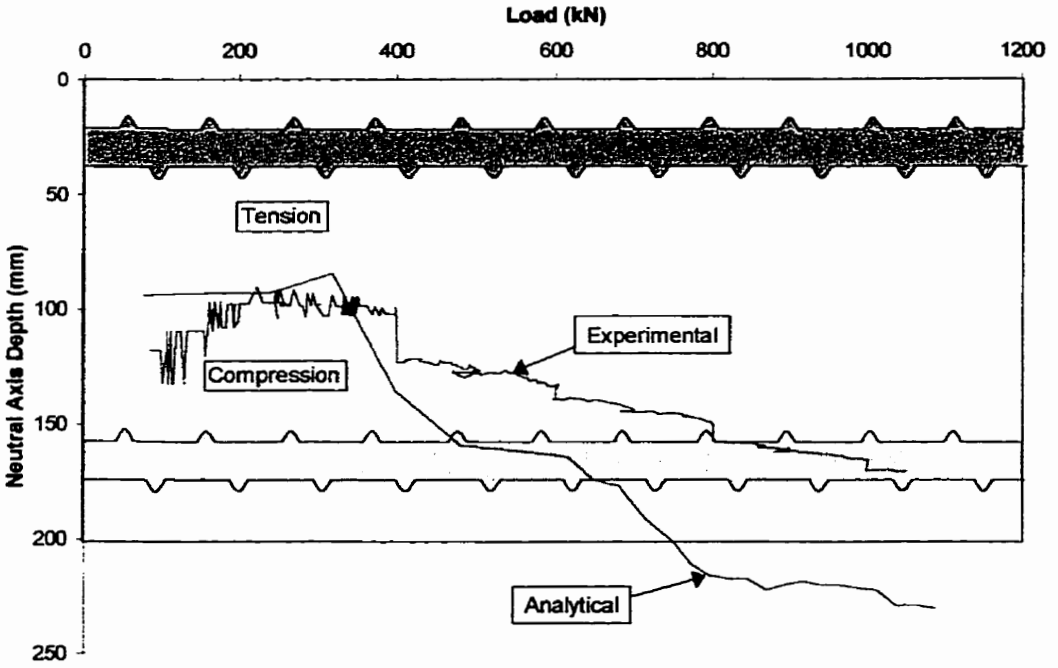

Figure 5-10: Load vs. Neutral Axis Depth Comparison

While it is evident that the behaviour of the analytical model did not correlate with that of the experimental model, investigation into the complex punching behaviour of bridge deck slabs is recommended for future research.

CHAPTER 6: COMPARISON WITH CFRP-REINFORCED BRIDGE DECK MODEL

6.1 TEST MODEL

A full-scale bridge deck model reinforced with carbon fibre reinforced plastic (CFRP) was constructed and tested at the University of Manitoba in 1996. The reinforcement detailing was identical to the reinforcement used in the construction of the Taylor Bridge built in Headingley, Manitoba, and completed in October, 1997. The model was identical in the general configuration and overall dimensions to the hybrid-reinforced model presented in this thesis. This chapter presents a comparison of the behaviour between interior spans of the CFRP- and hybrid-reinforced experimental models.

6.1.1 Reinforcement Details

The CFRP-reinforced model had the same dimensions as the hybrid-reinforced model, with overall plan dimensions of 3 m x 7.2 m. The reinforcement consisted of indented Leadline CFRP bars produced by Mitsubishi Chemicals Corporation, Japan. The bottom reinforcement consisted of double 10 mm bars at 125 mm in the short span, and single 10 mm bars at 125 mm in the direction parallel to the supporting beams. The top reinforcement consisted of single 10 mm bars at 125 mm in both main and secondary directions.

6.1.2 Test Sequence

Each of the three interior spans was tested independently and at different locations as shown in Figure 6-1. Different end restraints were used in each test to investigate their effect on the behaviour and failure mechanism of the bridge deck.

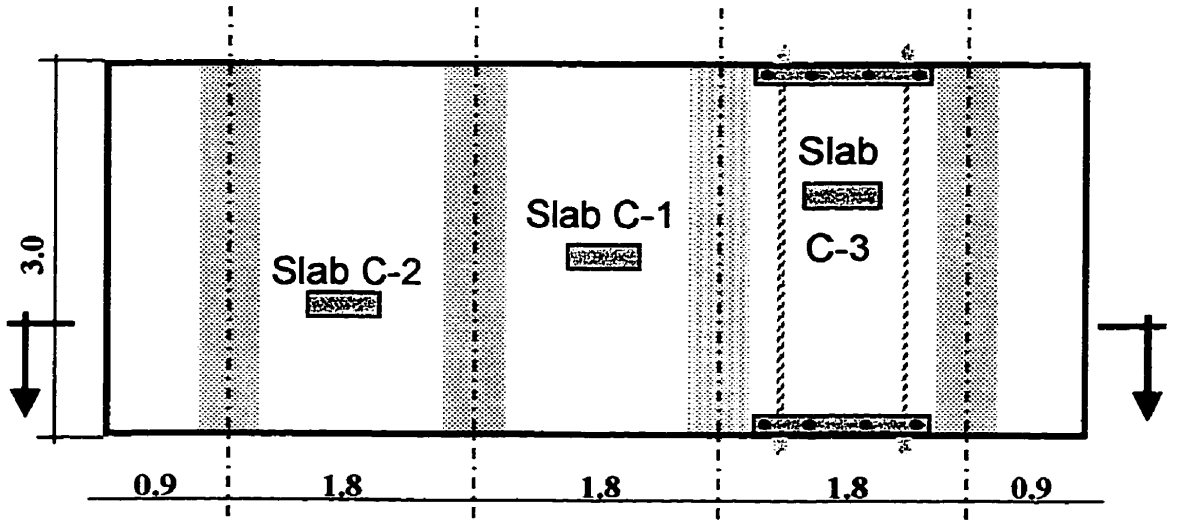

Figure 6-1: Plan View of CFRP-Reinforced Slab and Test Locations

Slab C-1 was tested by applying a concentrated load at the middle span of the model, as shown in Figure 6-1. Steel straps were used as end restraints to model the intermediate diaphragms of the bridge, as shown in Figure 6-2. Before the test was completed, at a load of 600 kN, the steel straps were found to have yielded. The span was unloaded, the straps were taken off, and testing resumed without end restraints up to failure.

The left slab (C-2) was tested with a load applied eccentrically with respect to slab C-1, as shown in Figure 6-3. The end restraints used for this test had a larger cross-

section to avoid yielding during the test. The end restraint conditions in this test are identical to those used for the slab tested with hybrid reinforcement.

Slab C-3 on the right span of the model was tested in a similar manner to C-2, as shown in Figure 6-4. In order to further investigate the effect of continuity of the slab, edge stiffeners were used in addition to the steel straps, as shown in Figure 6-1 and Figure 6-4.

It should be noted that the location of the applied load for the middle span and cantilevers of each model was at the mid-point between the two edges of the slab. The location of the load on the left and right spans on both models, however, was eccentric to reduce the effect of cracks initiated by testing the cantilevers and middle span.

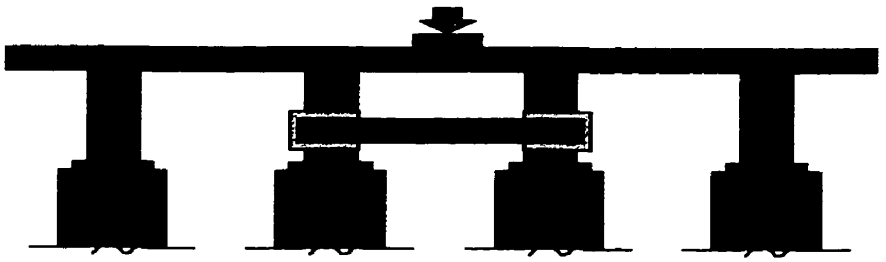

Figure 6-2: End Restraint for First Part of Slab C-1 Test

Figure 6-3: End Restraint for Slab C-2 Test

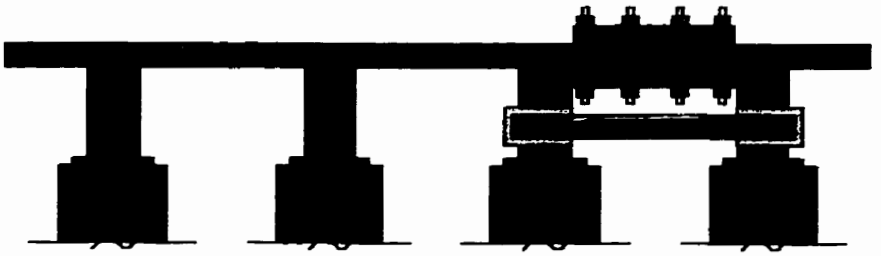

Figure 6-4: End Restraint and Edge Stiffeners for Slab C-3

6.2 GENERAL BEHAVIOUR

In this section, the test results of the interior spans of the CFRP-reinforced slab are presented. For a general comparison, the results from the hybrid-reinforced slab are included. Once the general behaviour is presented and discussed, a more direct comparison will be made between the two slabs for the purpose of determining the consequences that result from varying the reinforcing material.

The mode of failure of all tested slabs reinforced with CFRP- and hybrid-reinforcement was due to punching shear. Table 6–1 gives a summary of the failure loads and corresponding deflections relative to the girders for all tests. To evaluate the stiffness of the slab, the ratio of the ultimate load, P, to the corresponding

deflection, Δ, is also provided in Table 6–1. It can be seen that tests C-2, C-3, and H-2 have comparable load–deflection ratios. Two conclusions can be drawn from this observation: (1) the edge stiffeners used in C-3 did not significantly increase the overall stiffness of the slab; and (2) the hybrid reinforcement provided behaviour similar to that of the CFRP reinforcement.

Table 6–1: Failure Loads and Deflections for Various Tests

Test	Model	Span	Failure Load P (kN)	Deflection at Failure Δ (mm)	Stiffness P/Δ
C-1	CFRP	Middle	1000	7.6	132
C-2	CFRP	Left	1200	5.7	211
C-3	CFRP	Right	1328	6.2	214
H-2	Hybrid	Middle	1055	5.0	211
H-4	Hybrid	Left	1096	9.0	121
H-5	Hybrid	Right	1183	6.6	179

The load–deflection relationships for the tests under consideration are shown in Figure 6-5. Slab C-1 failed at the lowest load and at a high deflection in comparison to other slabs in the same model. This behaviour is a result of the removal of the

restraining straps, allowing rotation of the girders and consequently more flexural behaviour in comparison to the restrained slabs. This flexural behaviour allowed higher deflections and less development of two-way load distribution in comparison with other slabs. Slabs C-2 and H-2 were tested under similar boundary conditions, and therefore exhibited almost identical behaviour, as shown in Figure 6-5. The lower stiffness of slabs H-4 and H-5 is due to the extensive cracking induced by prior testing of the adjacent cantilevers. The slightly higher stiffness of slab C-3 is due to the presence of the edge restraint stiffeners added in the longitudinal direction.

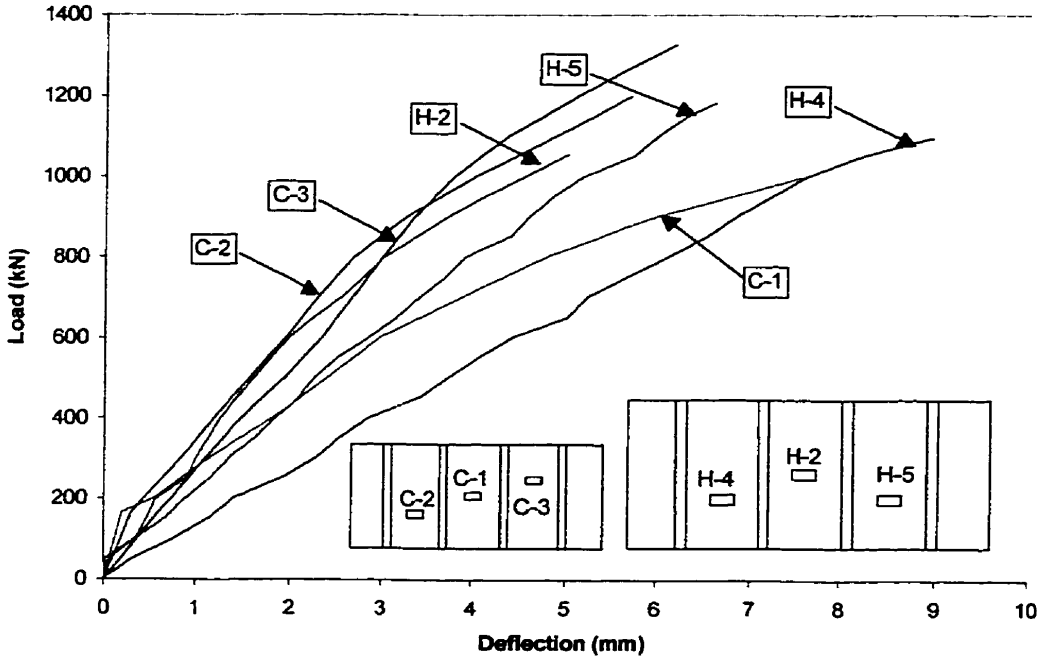

Figure 6-5 : Load–Deflection Relationships for the Two Tested Models

The load–girder rotation behaviour for the two models is shown in Figure 6-6. It can be seen that the girders for slab C-3 exhibit the smallest rotation values. This is a

result of the edge stiffeners, limiting curvature of the slab at the ends. If there is no curvature at the ends, there will be no girder rotation at the ends, thereby reducing the maximum girder rotation achieved. Slabs H-4 and H-5 experienced very high rates of rotation at low loads. As previously noted, the lack of initial stiffness of the system is due to the pre-existing cracks that were present on these two spans. The higher girder rotation for slab H-2 over slab C-2 is a result of the location of the applied load. The maximum girder rotation is at the location of the applied load and, since slab H-2 was loaded at the girder midspan, a larger girder rotation was able to develop than in slab C-2.

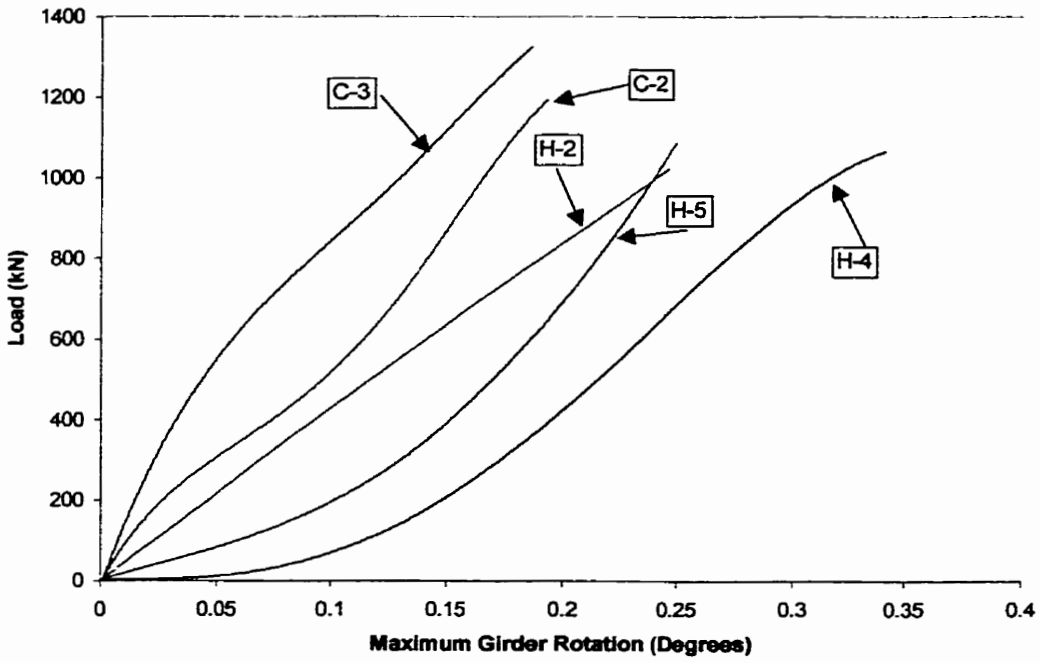

Figure 6-6: Load versus Maximum Girder Rotation for Various Tests

6.3 DIRECT COMPARISON

To best compare the behaviour of a deck slab reinforced by CFRP to one with hybrid GFRP/steel reinforcement, the behaviour of slabs C-1 (before removal of the strap) and C-2 will be compared to the behaviour of slab H-2. Slabs C-1 and C-2 are selected since they have similar boundary conditions in terms of the end restraints; therefore the only parameter being varied is the type of reinforcement. In addition, these spans were not significantly affected by the other tests performed on the model.

6.3.1 Load–Deflection Behaviour and Failure Loads

The load–deflection relationship for slab C-1 (before removal of the strap) and H-2 are shown in Figure 6-7. It can be seen that the behaviour of the two slabs is quite similar. However, as the slab in test C-1 approaches 600 kN, the stiffness decreases at a greater rate than that of span H-2. This might be attributed to the fact that the restraining straps in test C-1 started to yield before the load reached 600 kN. The yielding of the straps means that although the applied load on the slab increased, the straps no longer limited rotation of the girders, resulting in an increase in flexural behaviour, and consequently an increase in deflection, as shown in Figure 6-7.

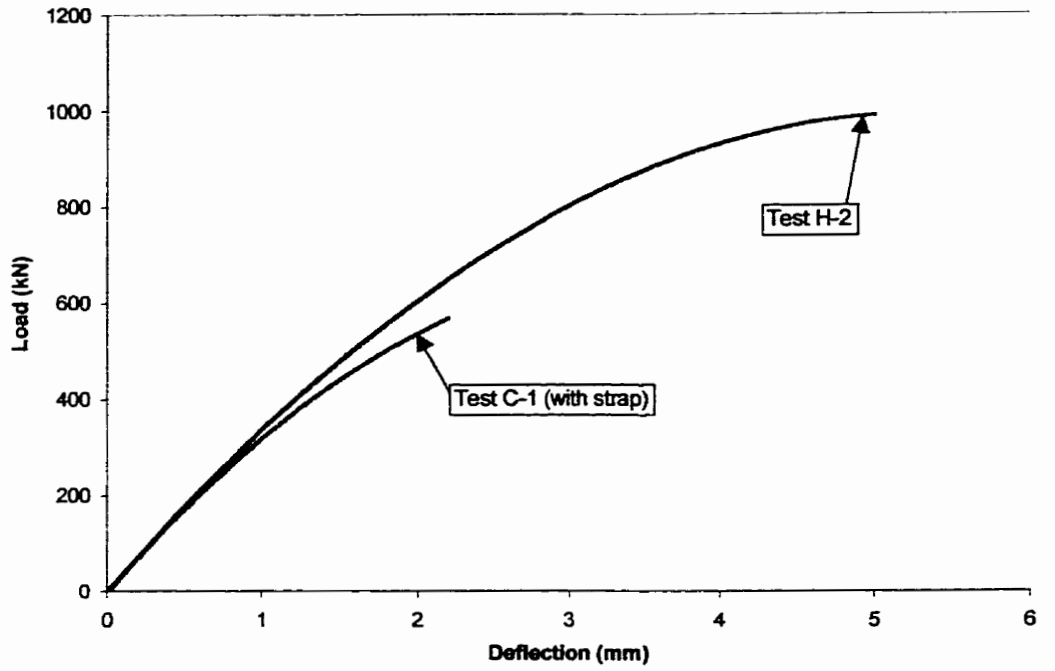

Figure 6-7: Load–Deflection for Tests C-1 and H-2

The load–deflection relationships for tests C-2 and H-2 are shown in Figure 6-8. Both slabs had the same initial stiffness. The stiffness of slab H-2 was reduced by increasing the applied load. Slab C-2 failed at a 15% higher load level than slab H-2. The stiffness reduction and lower level of failure load is matching the characteristics of the GFRP/steel in comparison to CFRP. It is also important to mention that the compressive strength of the concrete in the CFRP-reinforced model was 55 MPa, while that value for the hybrid-reinforced model was 45 MPa. The higher punching strength of slab C-2, therefore, might also be attributed to the higher compressive strength in the concrete. The current CSA code postulates that the shear resistance of a concrete member is a function of the square root of f_c'. If this is the case, the

shear resistance in C-2 would be 10% higher than in H-2. The results also indicate that the use of a significantly stronger material such as CFRP does not necessarily have a significant effect on increasing the ultimate capacity of the slab, which in fact is mainly controlled by the concrete strength and the geometric properties of the deck slab.

Results given in Table 6–1 for slabs C-2 and H-2 indicate that they exhibited almost identical stiffness values, suggesting that the type of reinforcement did not affect the overall stiffness. It can then be concluded that hybrid reinforcement in the slab produces similar serviceability and stiffness characteristics to those achieved with CFRP reinforcement. It is also important to note that the relative strengths of the slabs with the two types of reinforcement are much closer than the difference in reinforcement strength suggests.

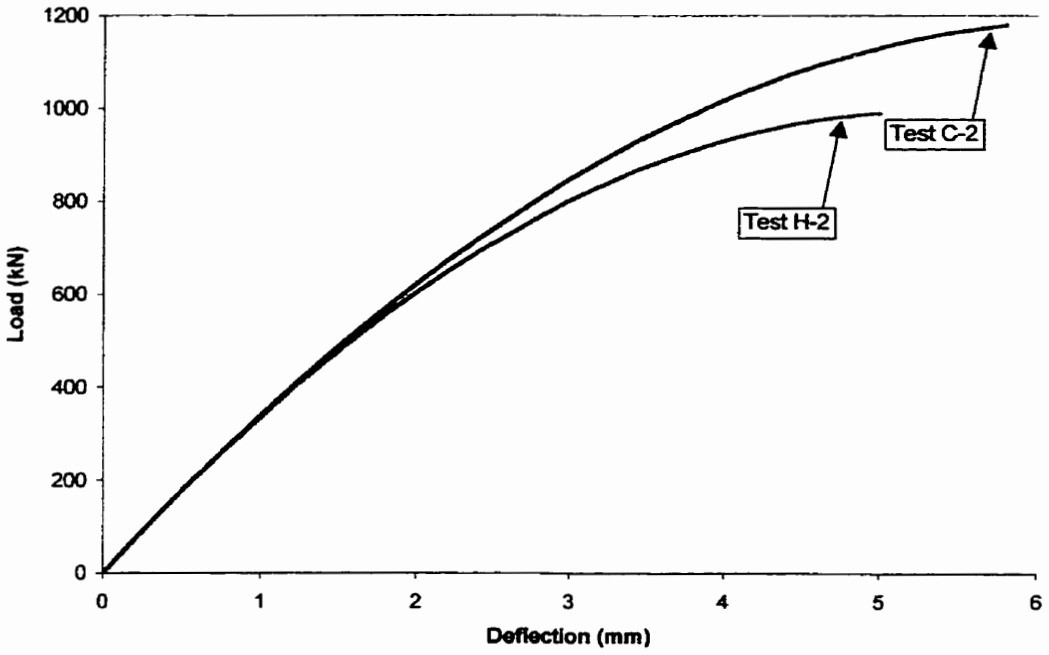

Figure 6-8: Load–Deflection for Tests C-2 and H-2

6.3.2 Crack Patterns

The crack distributions at a load level of 600 kN for the CFRP- and hybrid-reinforced slab are shown in Figure 6-9 and Figure 6-10, respectively. In terms of the number and orientation of the cracks, it can be seen that the crack patterns for tests H-2, H-4, and H-5 are similar to that in test C-2, which has the same restraint conditions. This behaviour confirms that the difference in reinforcement between the CFRP-reinforced slab and the hybrid-reinforced slab does not significantly affect the distribution, size, or orientation of the cracks. The crack distribution and orientation were significantly affected by the parameters that were varied for the CFRP-

reinforced model, namely the restraint stiffness and edge stiffeners. The effect on the crack patterns can be seen in Figure 6-9.

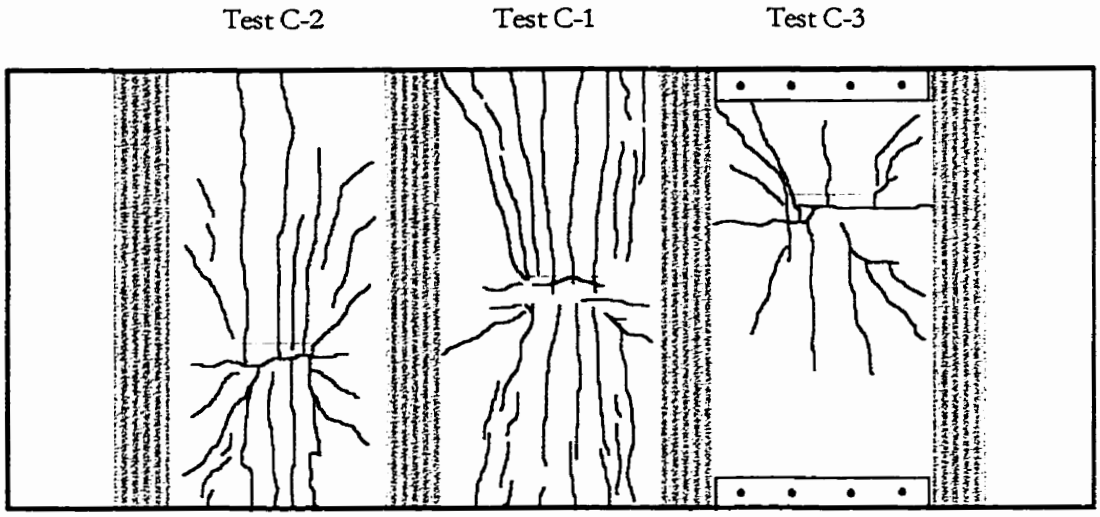

Figure 6-9: Cracks at 600 kN for CFRP-Reinforced Slab

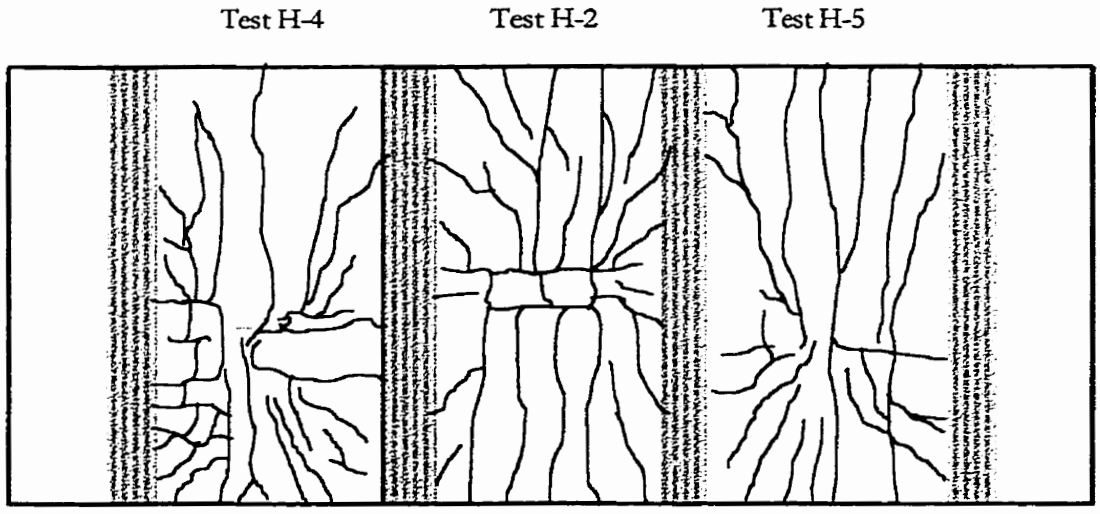

Figure 6-10: Cracks at 600 kN for Hybrid-Reinforced Slab

6.3.3 Girder Rotations

The load–rotation behaviour for C-2 and H-2 are shown in Figure 6-11. The stiffness values of both girders were almost identical up to a load level of 500 kN. As previously stated, the decrease in the rate of girder rotation of C-2 might be attributed to the location of the applied load.

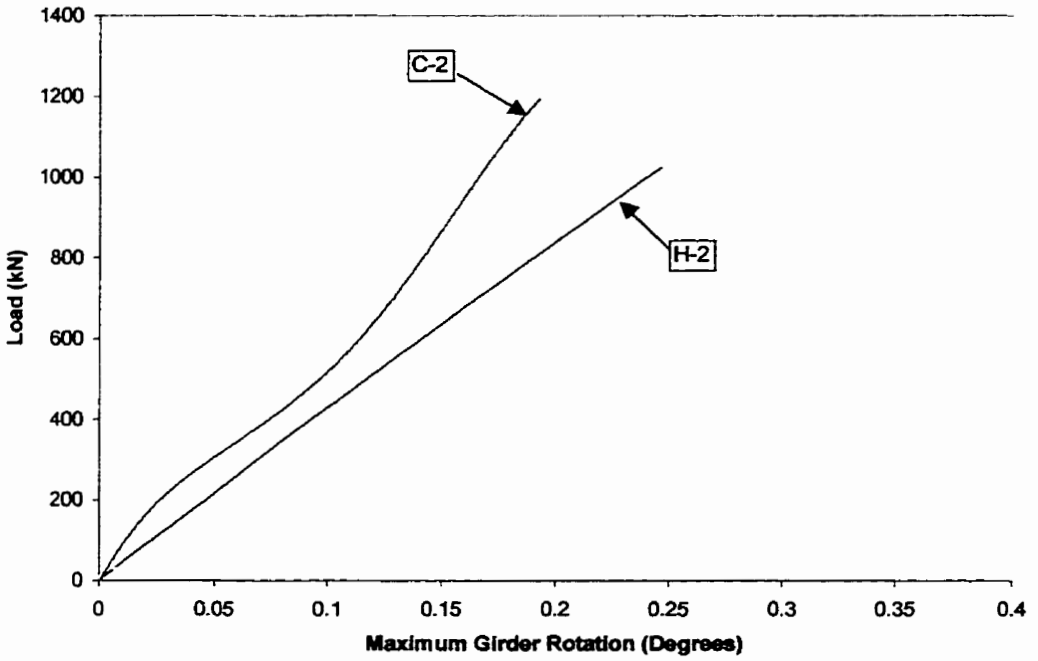

Figure 6-11: Maximum Girder Rotation for Tests C-2 and H-2

6.3.4 Neutral Axis Depth

The variation of neutral axis (NA) depth with applied load for tests C-2 and H-2 is shown in Figure 6-12. At midspan, the behaviour of the hybrid slab was similar to that of the CFRP slab, with the NA close to the mid-depth at low loads, followed by

a slight decrease due to the formation of flexural cracks at the bottom surface of the slabs. At the girder face location, the NA was much closer to the top surface at low load levels for the CFRP-reinforced slab, at a distance of 80 mm, compared to 100 mm for the hybrid-reinforced slab. This difference might be attributable to the very low strain readings observed at low loads. Before cracking, any small strain that is recorded by the strain gauges will result in a large change in neutral axis depth, because the change in strain reading is large relative its magnitude. As the load approaches a level of 400 kN, the neutral axis depth for both slabs was approximately 105 mm. As the applied load was increased, both slabs cracked and the neutral axis depth for the hybrid-reinforced slab increased at a faster rate than that of the CFRP-reinforced slab. This behaviour is attributed to the low elastic modulus of the GFRP in the hybrid slab in comparison to that of the CFRP. As the load was further increased, the NA depth in the CFRP slab increased at a greater rate than that of the hybrid slab. At a load of approximately 800 kN until failure, the neutral axis depth in the two slabs became very close. In both slabs, nearly the entire thickness of the slab at the girder was in tension at higher loads.

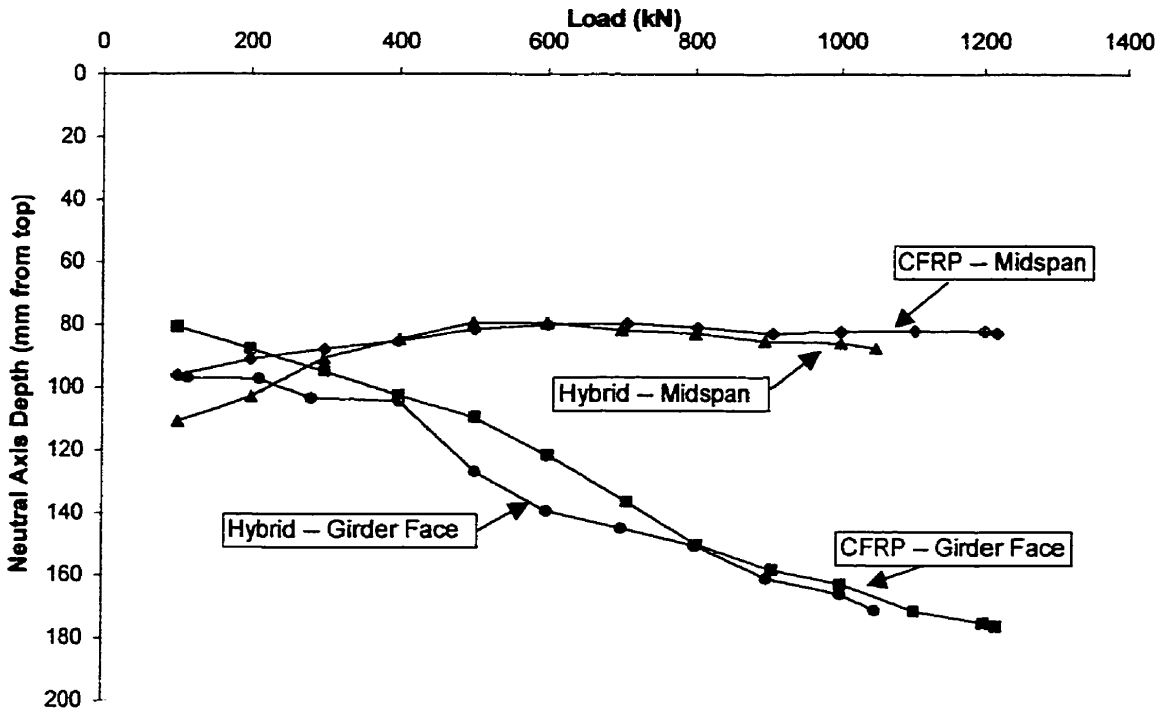

Figure 6-12: Neutral Axis Depth for Hybrid and CFRP Slabs at the Load Location

6.3.5 Membrane Forces

As previously discussed, the in-plane membrane forces that develop in the slab as it resists applied loads play an important role in the serviceability, ultimate capacity, and overall behaviour of the slab. The membrane forces for both the hybrid- and CFRP-reinforced slabs were calculated at the midspan and the girder face. Figure 6-13 shows the applied load vs. membrane force relationship for slabs H-2 and C-2 at these locations. At the girder face, the CFRP-reinforced slab develops much higher compressive membrane forces after cracking than the hybrid-reinforced slab. Since

the neutral axis did not increase dramatically as in the hybrid-reinforced slab after cracking, the area of concrete in compression is greater, resulting in an increase in net compressive forces. At the midspan location, the applied load vs. compressive membrane force relationship is virtually identical throughout the loading range.

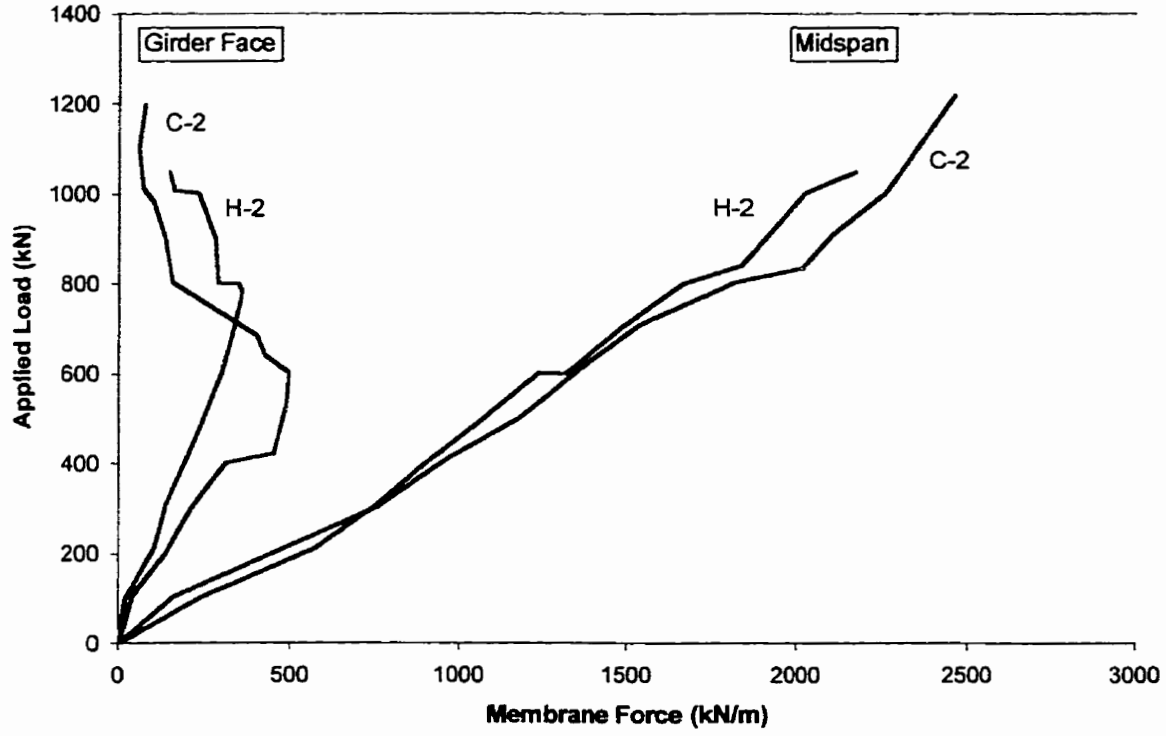

Figure 6-13: Membrane Force Comparison for Hybrid and CFRP Slabs

CHAPTER 7: CONCLUSIONS AND RECOMMENDATIONS

A full-scale model of a hybrid-reinforced highway bridge deck has been constructed and tested at the University of Manitoba. Based on the test results, analysis, and comparisons, the following conclusions can be made:

1. **All spans tested are satisfactory in terms of ultimate load-carrying capacity requirements.**

   The factored wheel load for the AASHTO (1998) design vehicle is 145 kN. In comparison, Table 7-1 shows the failure loads that were recorded for all five tests conducted on the full-scale model.

Table 7-1: Failure Loads for All Tested Spans

Test	Span	Failure Load (kN)
1	Right Cantilever	500
2	Middle Span	1050
3	Left Cantilever	875
4	Left Span	1090
5	Right Span	1180

2. The serviceability of all tested spans in the slab is satisfactory in terms of short-term deflection at service loads.

At service loads, the allowable deflection (Δ) for structural members not supporting or attached to non-structural elements likely to be damaged by large deflections, according to CSA A23.3-94, is $l/180$. For the cantilevers in the experimental model, the clear projection is 725 mm. This results in an allowable deflection of 4.0 mm. For the interior spans in the experimental model, the clear span is 1450 mm. The allowable deflection is therefore 8.0 mm. Table 7-2 shows the allowable deflections in comparison with those measured during each test. The span-to-deflection ratio (l/Δ) is also given.

Table 7-2: Deflections for All Tested Spans

Test	Location	Allowable Deflection (mm)	Deflection at Service Load (mm)	l/Δ **(minimum 180)**
1	Right Cantilever	4	1.0	725
2	Middle Span	8	0.15	9667
3	Left Cantilever	4	Very Small	Very Large
4	Left Span	8	0.7	2071
5	Right Span	8	0.3	4833

3. **The alkalinity that is present in normal concrete should not be considered a threat to the glass fibres in the FRP reinforcing bars used in this investigation.**

   Since there were no cracks at service load in either cantilever, or on the top surface of any of the interior spans, the stresses in the reinforcement were far below levels that would crack the matrix of the reinforcement. The glass fibres are therefore not susceptible to the effects of concrete alkalinity.

4. **The bond strength of the C-BAR reinforcement in the right cantilever was inadequate to utilise the full strength of the bars.**

   At failure, the tensile strain in the C-BAR reinforcement was well below the ultimate value. Improved bond characteristics would result in a higher capacity for the cantilever. For the left cantilever, the strain in the ISOROD reinforcement was close to the ultimate value obtained through tension tests. The reinforcement in the left cantilever might have been close to rupture at the point of failure.

5. **The low elastic modulus of GFRP reinforcing bars has no negative effect on the strength or serviceability of a highway bridge deck slab.**

   Although CFRP is much stronger than steel and stronger and stiffer than GFRP, the strength and serviceability characteristics of the CFRP-reinforced slab are not superior to those of the hybrid-reinforced slab.

6. **It is recommended that hybrid reinforcement be used in the design of bridge deck slabs.**

   The steel straps used in the experimental program simulated the cross-diaphragms in a bridge deck system. The presence of the straps reduced the rotation of the girders and consequently allowed the arch action mechanism to occur. Development of the compressive membrane forces reduced the deflection and therefore compensated for the low elastic modulus of the GFRP.

BIBLIOGRAPHY

1. Abdelrahman, Amr, T. Hassan, and G. Tadros, "Behaviour of Concrete Bridge Deck Model Reinforced by Carbon FRP," *26th Annual Conference of the Canadian Society for Civil Engineering*, Nova Scotia, June 1998.

2. Alexander, Scott D.B. and S. Simmonds, "Punching Shear Tests of Concrete Slab-Column Joints Containing Fiber Reinforcement," *American Concrete Institute Structural Journal*, Vol. 89, No. 4, pp. 425-432, July-August 1992.

3. American Association of State Highway and Transportation Officials, "AASHTO LRFD Bridge Design Specifications," 2nd ed., AASHTO, Washington, D.C., 1998.

4. American Concrete Institute, "Building Code Requirements for Reinforced Concrete," ACI, Michigan, 1990.

5. Anatech Corporation, "ANACAP Concrete Analysis Program: Advanced Finite Element Modeling for Stress, Ductility, and Thermal Analysis of Concrete and Steel Structures," Anatech Corporation, California, 1994.

6. Azad, Abul K., M. Baluch, M. Abbasi, and K. Kareem, "Punching Capacity of Deck Slabs in Girder-Slab Bridges," *American Concrete Institute Structural Journal*, Vol. 91, No. 6, pp. 656-662, November-December 1994.

7. Canadian Standards Association "Design of Concrete Structures," CSA, Ontario, 1995.

8. Chaallal, O., and B. Benmokrane, "Physical and Mechanical Performance of an Innovative Glass-Fiber-Reinforced Plastic Rod for Concrete and Grouted Anchorages," *Canadian Journal of Civil Engineering*, Vol. 20, No. 2, pp. 254-268, November, 1993.

9. Collins, Michael P. and Denis Mitchell, "Prestressed Concrete Structures," Response Publications, Ontario, 1997.

10. Comite Euro-International du Beton/Federation International de la Precontrainte, "CEB-FIP Model Code for Concrete Structures," Switzerland, 1990.

11. Ehsani, M.R., H. Saadatmanesh, and S. Tao, "Design Recommendations for Bond of GFRP Rebars to Concrete," *Journal of Structural Engineering*, American Society of Civil Engineers, Vol. 122, No. 3, March 1996.

12. Fang, I-Kuang, J. Lee, and C. Chen, "Behaviour of Partially Restrained Slabs Under Concentrated Load," *American Concrete Institute Structural Journal*, Vol. 91, No. 2, pp. 133-139, March-April, 1994.

13. GangaRao, H.V.S., P. Vijay, and D. Altizer, "Durability of Glass Composites under Alkaline and Prestress Environment, *Proceedings of the International Conference on Fibre Reinforced Structural Plastics in Civil Engineering, IIT*, Madras, 1995.

14. Gardner, N.J., "Relationship of the Punching Shear Capacity of Reinforced Concrete Slabs with Concrete Strength," *American Concrete Institute Structural Journal*, Vol. 87, No. 1, pp. 66-71, January-February, 1990.

15. Gardener, N.J., X. Shao, "Punching Shear of Continuous Flat Reinforced Concrete Slabs," *American Concrete Institute Structural Journal*, Vol. 93, No. 2, pp. 218-227, March-April 1996.

16. Hewitt, Brian E. and B. Batchelor, "Punching Shear Strength of Restrained Slabs," *American Society of Civil Engineers Journal of the Structural Division*, New York, New York, pp. 1837-1853, September, 1975.

17. ISIS Canada, "Material Properties of C-BAR Reinforcing Rods," Manitoba, June 1997.

18. Jacobson, Amnon, "Membrane-Flexural Failure Modes of Restrained Slabs," *Proceedings of the American Society of Civil Engineers*, New York, New York, pp. 85-113, October, 1967.

19. Japanese Society of Civil Engineers, "Standard Specification for Design and Construction of Concrete Structures," Concrete Library, Japan, 1986.

20. Kirkpatrick, J., G. Rankin, and A. Long, "The Influence of Compressive Membrane Action on the Serviceability of Beam and Slab Bridge Decks," *The Structural Engineer*, Vol. 64B, No. 1, pp. 6-9, March 1986.

21. Kuang, J.S., and C. Morley, "A Plasticity Model for Punching Shear of Laterally Restrained Slabs with Compressive Membrane Action," *International Journal of Mechanical Science*, Vol. 35, No. 5, pp. 371-385, 1993.

22. Kuang J.S. and C. Morley, "Punching Shear Behaviour of Restrained Reinforced Concrete Slabs," *American Concrete Institute Structural Journal*, Vol. 89, No. 1, pp. 13-19, January-February 1992.

23. Loo, Yew-Chaye and M. Falamaki, "Punching Shear Strength Analysis of Reinforced Concrete Flat Plates with Spandrel Beams," *American Concrete Institute Structural Journal*, Vol. 89, No. 4, pp. 375-383, July-August, 1992.

24. Marshall Industries Composites, Inc., "C-BAR Composite Reinforcing Rods: The Future of Concrete Reinforcement," Information literature, Florida, ca. 1997.

25. Marzouk, H. and Hussein, A., "Punching Shear Analysis of Reinforced High-Strength Concrete Slabs," *Canadian Journal of Civil Engineering*, Vol. 18, pp. 954-963, 1991.

26. Ministry of Transportation of Ontario, "Ontario Highway Bridge Design Code," Ontario, 1991.

27. Mufti, Aftab A., L. Jaeger, and L. Wegner, "Experimental Investigation of Fiber-Reinforced Concrete Deck Slabs without Internal Steel Reinforcement," *Canadian Journal of Civil Engineering*, Vol. 20, pp. 398-406, 1993.

28. Newhook, John P., "The Behaviour of Steel-Free Concrete Bridge Deck Slabs Under Static Loading Conditions—Research Report No. 2," Dalhousie University, Nova Scotia, 1997.

29. Paramasivam, P. and K. Tan, "Punching Shear Strength of Ferrocement Slabs," *American Concrete Institute Structural Journal*, Vol. 90, No. 3, pp. 294-301, May-June 1993.

30. Park, R., "The Ultimate Strength and Long-Term Behaviour of Uniformly Loaded, Two-Way Concrete Slabs with Partial Lateral Restraint at all Edges," *Magazine of Concrete Research*, Vol. 16, No. 48, pp. 139-152, September, 1964.

31. Park, R., "Tensile Membrane Behaviour of Uniformly Loaded Rectangular Reinforced Concrete Slabs with Fully Restrained Edges," *Magazine of Concrete Research*, Vol. 16, No.46, pp. 39-44, March 1964.

32. Park, R., "The Lateral Stiffness and Strength Required to Ensure Membrane Action at the Ultimate Load of a Reinforced Concrete Slab-and-Beam Floor," *Magazine of Concrete Research*, Vol. 17, No. 50, pp. 29-38, March 1965.

33. Park, R., and T. Paulay, "Reinforced Concrete Structures," John Wiley & Sons, New York, 1975.

34. Pultrall Inc., "ISOROD: Glass-Fibre Composite Rebar for Concrete—Technical Data," Pultrall Inc., Quebec, February 1992.

35. Siao, Wen Bin, "Punching Shear Resistance of Flat Slabs: A Beam-Strip Analogy," *American Concrete Institute Structural Journal*, Vol. 91, No. 5, pp. 594-604, September-October 1994.

36. Tadros, G., E. Tromposch, and A. Mufti, "University Drive/Crowchild Trail Bridge Superstructure Replacement," *Second International Conference on Composites in Infrastructure*, Conference Proceedings, Arizona, 1998.

37. Taylor, R. and B. Hayes, "Some Tests on the Effect of Edge Restraint on Punching Shear in Reinforced Concrete Slabs," *Magazine of Concrete Research*, Vol. 17, No. 50, pp. 39-44, March 1965.

38. Wegner, Leon D., and Mufti, Aftab A., "Finite Element Investigation of Fibre-Reinforced Concrete Deck Slabs Without Internal Steel Reinforcement," *Canadian Journal of Civil Engineering*, Vol. 21, No. 2, pp. 231-236, April, 1994.